



**Defense Nuclear Agency
Alexandria, VA 22310-3398**



DNA-TR-96-19

Load-Damage Relationships for Chemical Submunitions

**James D. Colton, et al.
SRI International
333 Ravenswood Avenue
Menlo Park, CA 94025-3434**

October 1996

Technical Report

CONTRACT No. DNA 001-93-C-0104

Approved for public release;
distribution is unlimited.

19961022 030

DTIC QUALITY INSPECTED 1

DESTRUCTION NOTICE:

Destroy this report when it is no longer needed.
Do not return to sender.

PLEASE NOTIFY THE DEFENSE SPECIAL WEAPONS
AGENCY, ATTN: CSTI, 6801 TELEGRAPH ROAD,
ALEXANDRIA, VA 22310-3398, IF YOUR ADDRESS IS
INCORRECT, IF YOU WISH IT DELETED FROM THE
DISTRIBUTION LIST, OR IF THE ADDRESSEE IS NO
LONGER EMPLOYED BY YOUR ORGANIZATION.



DISTRIBUTION LIST UPDATE

This mailer is provided to enable DSWA to maintain current distribution lists for reports. (We would appreciate your providing the requested information.)

- ☐ Add the individual listed to your distribution list.
- ☐ Delete the cited organization/individual.
- ☐ Change of address.

NOTE:

Please return the mailing label from the document so that any additions, changes, corrections or deletions can be made easily. For distribution cancellation or more information call DSWA/IMAS (703) 325-1036.

NAME: _____

ORGANIZATION: _____

OLD ADDRESS

CURRENT ADDRESS

TELEPHONE NUMBER: () _____

DSWA PUBLICATION NUMBER/TITLE

CHANGES/DELETIONS/ADDITIONS, etc.)

(Attach Sheet if more Space is Required)

DSWA OR OTHER GOVERNMENT CONTRACT NUMBER: _____

CERTIFICATION OF NEED-TO-KNOW BY GOVERNMENT SPONSOR (if other than DSWA):

SPONSORING ORGANIZATION: _____

CONTRACTING OFFICER OR REPRESENTATIVE: _____

SIGNATURE: _____

CUT HERE AND RETURN



DEFENSE SPECIAL WEAPONS AGENCY
ATTN: IMAS
6801 TELEGRAPH ROAD
ALEXANDRIA, VA 22310-3398

DEFENSE SPECIAL WEAPONS AGENCY
ATTN: IMAS
6801 TELEGRAPH ROAD
ALEXANDRIA, VA 22310-3398

REPORT DOCUMENTATION PAGE			Form Approved OMB No. 0704-0188	
Public reporting burden for this collection of information is estimated to average 1 hour per response including the time for reviewing instructions, searching existing data sources, gathering and maintaining the data needed, and completing and reviewing the collection of information. Send comments regarding this burden estimate or any other aspect of this collection of information, including suggestions for reducing this burden, to Washington Headquarters Services, Directorate for Information Operations and Reports, 1215 Jefferson Davis Highway, Suite 1204, Arlington, VA 22202-4302, and to the Office of Management and Budget, Paperwork Reduction Project (0704-0188), Washington, DC 20503.				
1. AGENCY USE ONLY (Leave blank)	2. REPORT DATE 961001	3. REPORT TYPE AND DATES COVERED Technical 930520 - 950131		
4. TITLE AND SUBTITLE Load-Damage Relationships for chemical Submunitions		5. FUNDING NUMBERS C - DNA 001-93-C-0104 PE - 63216C, 63216C, 63214C PR - SB, AJ, AJ TA - AE, AE, AF WU - DH338260		
6. AUTHOR(S) James D. Colton, Curtis M. Romander, Steven W. Kirkpatrick, Alexander L. Florence, and Jacques H. Giovanola				
7. PERFORMING ORGANIZATION NAME(S) AND ADDRESS(ES) SRI International 333 Ravenswood Avenue Menlo Park, CA 94025-3434		8. PERFORMING ORGANIZATION REPORT NUMBER PYU-4727		
9. SPONSORING/MONITORING AGENCY NAME(S) AND ADDRESS(ES) Defense Special Weapons Agency 6801 Telegraph Road Alexandria, VA 22310-3398 WELR/Hunter		10. SPONSORING/MONITORING AGENCY REPORT NUMBER DNA-TR-96-19		
11. SUPPLEMENTARY NOTES This work was sponsored by the Ballistic Missile Defense Office (BMDO) and managed and executed by the Defense Special Weapons Agency under RDT&E RMC Codes B7668D SB AE 00002 7010A AJ 25904D, B7668D AJ AE 00002 7010A 25904D, and B7666D AJ AF 00012 7010A 25904D.				
12a. DISTRIBUTION/AVAILABILITY STATEMENT Approved for public release; distribution is unlimited.			12b. DISTRIBUTION CODE	
13. ABSTRACT (Maximum 200 words) We determined the load-damage relationship for individual chemical submunitions to link (1) the loads on individual submunitions in a complete target that can be measured or calculated and (2) the damage to individual submunitions that is more difficult to determine. Impact experiments and calculations were conducted on single Chemical Submunitions 1 and 2 (nominally 95% full of water) at full-, half-, and quarter-scale, at velocities up to 330 m/s to simulate impacts away from the direct impact area in a complete target impacted by a hit-to-kill vehicle. The damage mechanisms were similar to those produced in sled tests of complete targets: failure of the burst diaphragm, removal of the fuze plug, fracture where the case is welded to the top and axial fractures in the casing. The load-damage relationship was quantified in terms of pressure-impulse or PI curves. We also determined that submunitions could be ejected at velocities of about 65 m/s with no damage to prevent their functioning. We compared the material and structural response of full- and quarter-scale Chemical Submunitions 2. We found that when the burst diaphragm static strength is matched, the more dominant mechanisms observed in array tests, diaphragm failure and fuze removal, are the same at both scales. Failure of the weld did not occur in the quarter-scale because of intentional differences in construction. Fractures in the cylindrical casing of the submunitions, less frequently observed than diaphragm or fuze failure, were more ductile and hence required greater equivalent loads to produce in quarter-scale than in full-scale.				
14. SUBJECT TERMS Chemical Submunitions Theater Missile Defense			15. NUMBER OF PAGES 152	
			16. PRICE CODE	
17. SECURITY CLASSIFICATION OF REPORT UNCLASSIFIED	18. SECURITY CLASSIFICATION OF THIS PAGE UNCLASSIFIED	19. SECURITY CLASSIFICATION OF ABSTRACT UNCLASSIFIED	20. LIMITATION OF ABSTRACT SAR	

UNCLASSIFIED

SECURITY CLASSIFICATION OF THIS PAGE

CLASSIFIED BY:

N/A since Unclassified.

DECLASSIFY ON:

N/A since Unclassified.

EXECUTIVE SUMMARY

Missiles with payloads comprising arrays of chemical submunitions are a key target in the Theater Missile Defense Program. To determine the response of such payloads to hit-to-kill vehicles, other organizations have conducted sled tests at impact velocities up to 2 km/s, to observe submunition response, and have performed computer code calculations of the response. However, neither approach allows a detailed investigation into the load and response of individual submunitions. Submunitions that are away from the impact area, where the secondary impact velocities from fragments or neighboring submunitions are hundreds of meters per second, are of particular interest because the damage to those submunitions strongly affects the damage to the overall array. A determination of the load-damage relationships for chemical submunitions can link measurements of response made in sled tests and calculated in the most sophisticated codes to final damage to individual submunitions. Load-damage relationships are also important in performing lethality assessments where damage, which must be assessed for a range of parameters, cannot be determined in sled tests or with computer code calculations.

The primary objective of the research reported here was to determine the load-damage relationships for chemical submunitions. Secondary objectives were to determine the maximum velocity with which a surviving submunition can be ejected from the submunition array (for post-engagement analysis), to provide data for computer code validation of submunition response, and to evaluate scaling of chemical submunitions to impact response.

Our approach consisted of the following steps:

- Identify the damage mechanisms produced in the sled tests
- Perform experiments and analyses to investigate the damage mechanisms in detail
- Based on results of the above, develop load-damage relationships in terms of pressure-impulse relationships
- Compare damage mechanisms in full- and quarter-scale hit-to kill tests on submunition arrays and perform well-controlled impact experiments and material property measurements at different scales.

We conducted impact experiments on single, full-scale Chemical Submunitions 1 and 2, and on half- and quarter-scale Chemical Submunitions 2 at velocities up to 330 m/s. Most submunitions had their volume filled to 95% capacity with water to simulate the chemical agent. To study basic response mechanisms of submunitions, most tests were performed with a gas gun to accelerate steel plates or actual submunition models into single submunition targets. In the impact experiments, we measured the impact

velocity and frequently used high-speed movies and high-speed video to observe the impacts and to measure the velocity imparted to the target. We performed computer code calculations on individual submunitions to plan and interpret the experiments and to broaden our understanding of the response phenomena.

We conducted a series of experiments in which single, full-scale submunitions were impacted with a plate to determine the location, orientation, and magnitude of the loads required to produce damage similar to that observed in the sled tests. Figure S-1 summarizes the results for Chemical Submunition 1 (similar experiments were performed for Chemical Submunition 2). Impact of the fuze end of the models demonstrated that the fuze acts as a good energy absorber that protects the body of the submunition. Therefore, nose-on loads are the largest loads needed to produce damage. The smallest loads to produce damage are those that occur on the shoulder, causing the weld that connects the top and the main body of the submunition to fail. For side impact, the damage mechanism was frequently rupture of the burst diaphragm and/or removal of the fuze.

We performed plate impact experiments and computer code calculations to investigate the effect of ullage amount and location. We found that, for the range of dynamic loadings investigated, the failure of the diaphragm is largely a dynamic phenomenon in the fluid. Therefore, the amount of ullage did not significantly affect diaphragm failure. We also found that the location of the ullage was not important in causing damage to the diaphragm; the same damage occurred even when the ullage was located at the diaphragm.

We performed a series of experiments and calculations to quantify the load-damage relationship in terms of the applied peak pressure and impulse (PI) curves. Figure S-2 summarizes the results for external loading that spans the entire side of Submunition 2. The figure illustrates how different types of experiments can be used to span the load durations of interest. The figure also shows the similarity between the experimental results and the calculations, and how both can be used to construct PI curves. Techniques based on the response characteristics of the diaphragm were developed to assign pressures and impulses to the multi-peak, finite-rise, waveforms produced in the fluid. The figure shows calculated critical internal pressures and impulses that correspond to the critical external loads. Similar data and calculations provided additional points on PI plots to characterize external spot loading (i.e., plate impact) on the side and nose-on loading for Chemical Submunition 2, and side, spot, and nose-on loading for Chemical Submunition 1. The PI curves for either external or internal loading can be used to link measurements and calculations of loads produced in hit-to-kill scenarios with damage to submunitions.

Based on the mechanisms observed in the experiments and the code calculations, we developed simple analyses to predict PI curves for diaphragm rupture and fuze failure. The PI curves derived from the simple analyses can be used to predict response for other parameters of interest. For example, if the thickness of the submunition is decreased, the simple analyses can be used to estimate PI curves for the

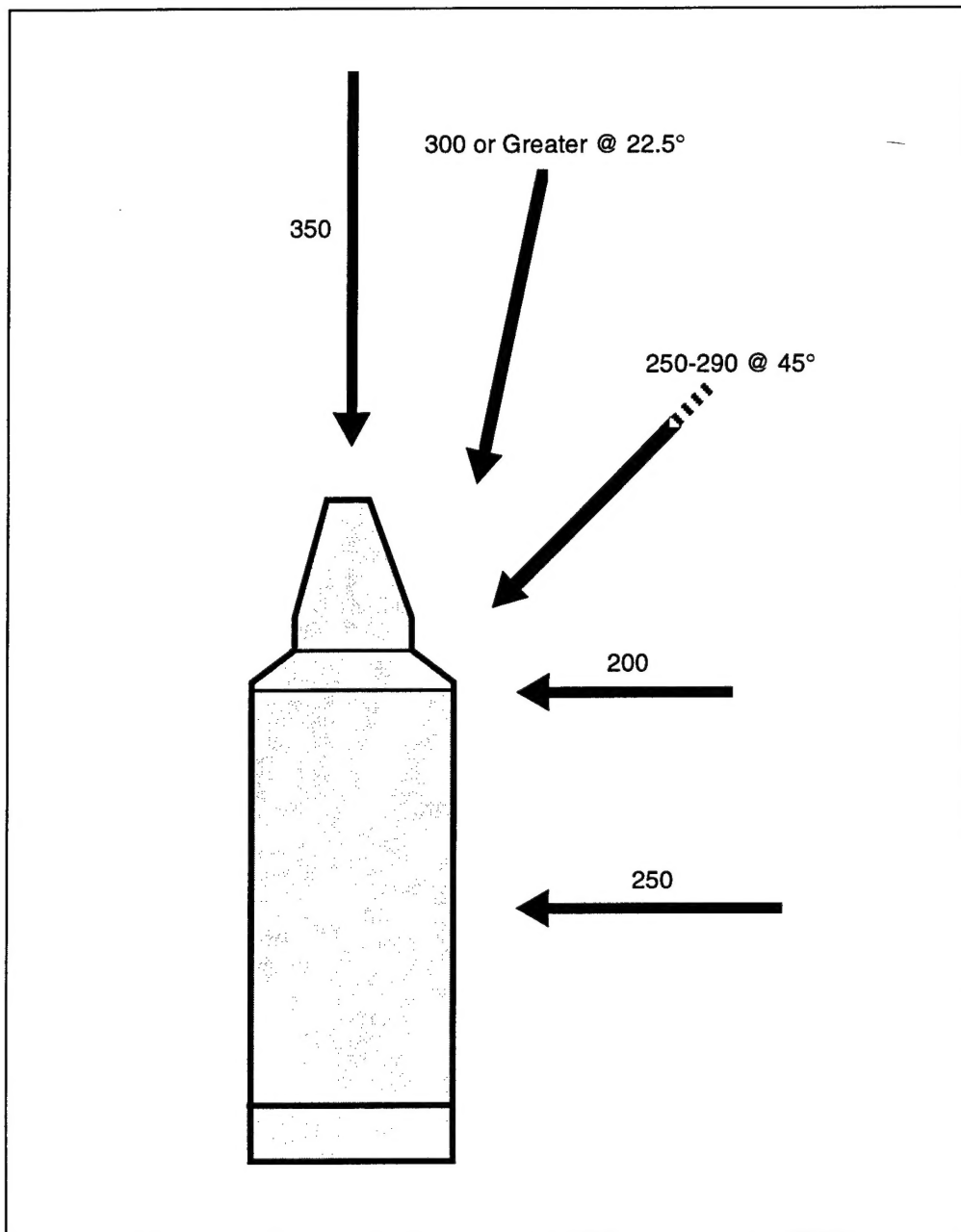
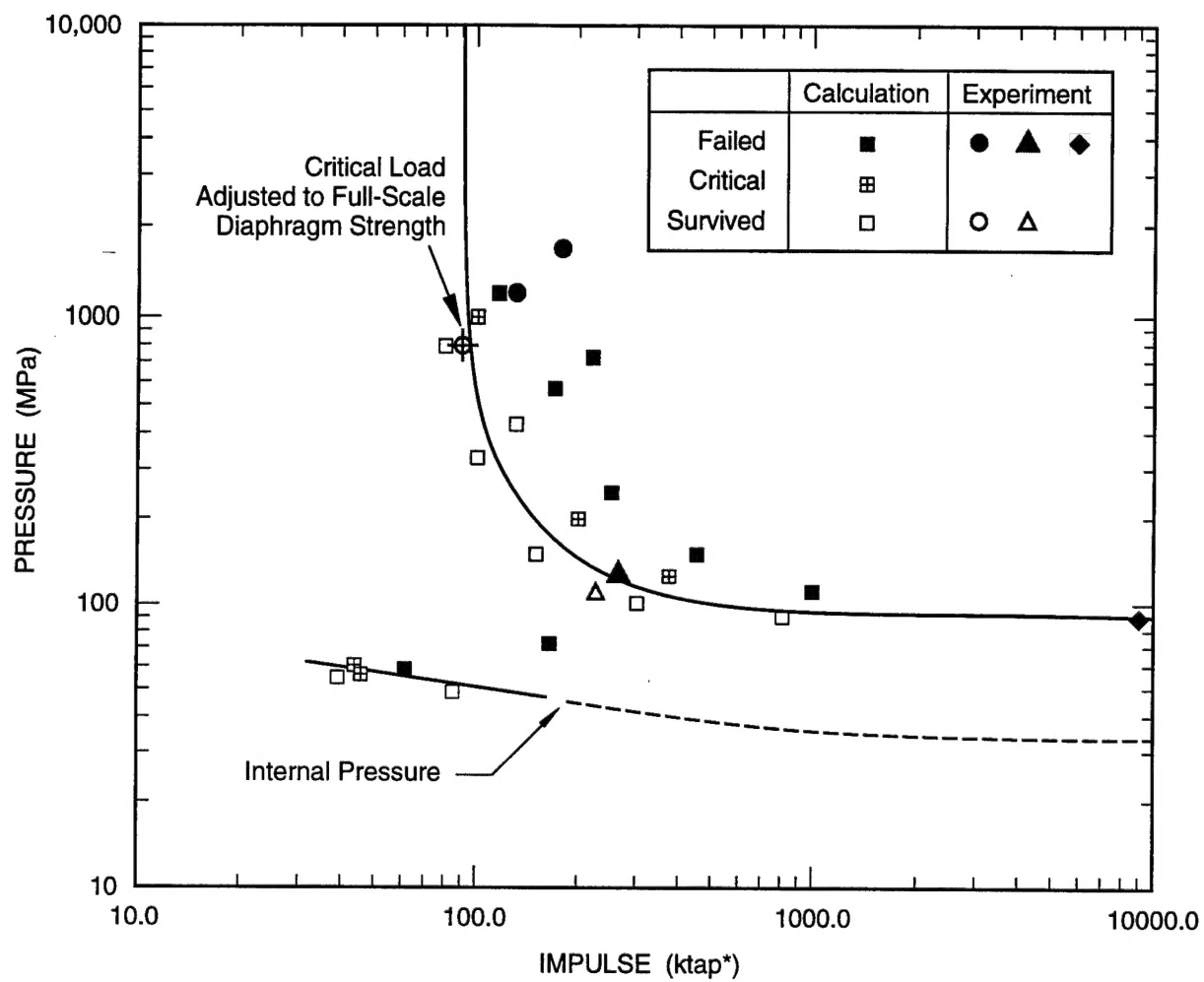


Figure S-1. Impact velocities to produce failure in Chemical Submunition 1 for different types of impacts (1.9-cm-thick, 8.9-cm-diameter impactors).



*1 tap = 1 dyne • s/cm²

Figure S-2. PI curve for external side load Chemical Submunition 2.

modified submunitions. These analyses are particularly useful for lethality assessment, because a large number of loading conditions can be quickly evaluated.

Submunition to submunition impacts were also conducted to determine the maximum residual velocity that could be imparted to a submunition that survived the impact. From tests with the impacting submunition and the impacted submunition aligned, and tests with the two submunitions at right angles to each other, we found that the maximum velocity that could be imparted to a surviving submunition was about 65 m/s.

We also investigated scaling of submunition response. Available data from full-scale hit-to-kill sled tests and quarter-scale gun tests indicated that fragmentation of the submunitions in the vicinity of the impact appears to scale. Differences in the damage to the submunition casing resulted from differences in construction (welds versus no welds—not a true scaling difference) and from differences in fracture behavior between the full- and the quarter-scale material. The (scaled) loads to produce fracture of the casing were greater at quarter-scale than at full-scale. Thus, if fracture of the submunition casing is a significant damage mode of interest, care must be taken in interpreting the results of small model experiments. When fragmentation or fracture of the casing did not occur (which was the case for a majority of the submunitions in the array) and when the burst diaphragm static strength is properly scaled, the damage mechanisms and critical loads (notably diaphragm and fuze failure) were similar in the full- and quarter-scale submunitions.

Although the half-scale models had a greater hydrostatic burst pressure to fail the diaphragm than the other models, the failure mechanisms were the same as for full-scale and we expect that properly designed and constructed models would have critical loads to cause failure very close to that of the full-scale.

We recommend that

- Additional experiments be carried out, particularly on Submunition 1, to complete the critical load curves for external and internal loads and for multiple impacts.
- Simplified models be developed for loading over a portion of the side of the submunition, for axial impact, and for internal loads for loading other than side area loading.
- The critical load curves developed be integrated into lethality assessment codes such as KAPPII.
- Additional experiments be conducted to refine the critical survival velocity imparted to an impacted submunition by glancing blows and multiple impacts. Post-engagement analyses of the results should also be conducted.

PREFACE

The work discussed in this technical report was performed from May 1993 through November 1994 under Contract No. DNA 001-93-C-0104. Commander K. Hunter was the DNA COTR. This report deals primarily with structural damage to chemical submunitions. A companion technical report is being issued concurrently entitled "Improved Fragmentation Algorithms for Debris Environments."

CONVERSION TABLE

Conversion factors for U. S. Customary to metric (SI) units of measurement

MULTIPLY TO GET ← BY → TO GET
 ← BY → DIVIDE

angstrom	1.000 000	X E -10	meters (m)
atmosphere (normal)	1.013 25	X E +2	kilo pascal (kPa)
bar	1.000 000	X E +2	kilo pascal (kPa)
barn	1.000 000	X E -28	meter ² (m ²)
British thermal unit (thermochemical)	1.054 350	X E +3	joule (J)
calorie (thermochemical)	4.184 000		joule (J)
cal (thermochemical)/cm ²	4.184 000	X E -2	mega joule/m ² (MJ/m ²)
curie	3.700 000	X E +1	*giga becquerel (GBq)
degree (angle)	1.745 329	X E -2	radian (rad)
degree Fahrenheit	$T_K = (T^{\circ}F + 459.67)/1.8$		degree kelvin (K)
electron volt	1.602 19	X E -19	joule (J)
erg	1.000 000	X E -7	joule (J)
erg/second	1.000 000	X E -7	watt (W)
foot	3.048 000	X E -1	meter (m)
foot-pound-force	1.355 818		joule (J)
gallon (U.S. liquid)	3.785 412	X E -3	meter ³ (m ³)
inch	2.540 000	X E -2	meter (m)
jerk	1.000 000	X E +9	joule (J)
joule/kilogram (J/kg) (radiation dose absorbed)	1.000 000		Gray (Gy)
kilotons	4.183		terajoules
kip (1000 lbf)	4.448 222	X E +3	newton (N)
kip/inch ² (ksi)	6.894 757	X E +3	kilo pascal (kPa)
ktap			newton-second/m ²
	1.000 000	X E +2	(N-s/m ²)
micron	1.000 000	X E -6	meter (m)
mil	2.540 000	X E -5	meter (m)
mile (international)	1.609 344	X E +3	meter (m)
ounce	2.834 952	X E -2	kilogram (kg)
pound-force (lbs avoirdupois)	4.448 222		newton (N)
pound-force inch	1.129 848	X E -1	newton/meter (N · m)
pound-force/inch	1.751 268	X E +2	newton-meter (N/m)
pound-force/foot ²	4.788 026	X E -2	kilo pascal (kPa)
pound-force/inch ² (psi)	6.894 757		kilo pascal (kPa)
pound-mass (lbm avoirdupois)	4.535 924	X E -1	kilogram (kg)
pound-mass-foot ² (moment of inertia)			kilogram-meter ²
	4.214 011	X E -2	(kg·m ²)
pound-mass-foot ³			kilogram/meter ³
	1.601 846	X E +1	(kg/m ³)
rad (radiation dose absorbed)	1.000 000	X E -2	**Gray (Gy)
roentgen			coulomb/kilogram
	2.579 760	X E -4	(C/kg)
shake	1.000 000	X E -8	second (s)
slug	1.459 390	X E +1	kilogram (kg)
torr (mm Hg, 0° C)	1.333 22	X E -1	kilo pascal (kPa)

*The becquerel (Bq) is the SI unit of radioactivity; 1 Bq = 1 event/s.

**The Gray (Gy) is the SI unit of absorbed radiation.

TABLE OF CONTENTS

Section	Page
EXECUTIVE SUMMARY	iii
PREFACE	viii
CONVERSION TABLE	ix
FIGURES	xii
TABLES	xv
1 INTRODUCTION.....	1
1.1 BACKGROUND	1
1.2 OBJECTIVES	2
1.3 APPROACH	2
2 CHEMICAL SUBMUNITION IMPACT RESPONSE	4
2.1 DAMAGE MODES OBSERVED IN SLED TESTS.....	4
2.2 PROCEDURES FOR SINGLE SUBMUNITION EXPERIMENTS.....	8
2.2.1 Submunitions.....	8
2.2.2 Loading Techniques	10
2.2.3 Measurement Techniques	12
2.3 PROCEDURES FOR SINGLE SUBMUNITION CALCULATIONS.....	15
2.3.1 DYNA3D	15
2.3.2 L2D.....	17
2.4 SUBMUNITION RESPONSE TO LOCALIZED LOADING.....	17
2.4.1 Axial Impact.....	20
2.4.2 Calculations of Axial Loading Response.....	26
2.4.3 Other Plate Impact Experiments.....	27
2.4.4 Other Plate Impact Calculations.....	27
2.4.5 Effects of Ullage.....	36
2.5 SUBMUNITION RESPONSE TO SIDE AREA LOADING	39
2.5.1 Experiments	39
2.5.2 Calculations.....	39
2.6 RESIDUAL VELOCITIES	42
3 PRESSURE-IMPULSE CURVES FOR CHEMICAL SUBMUNITIONS.....	47
3.1 BACKGROUND	47

TABLE OF CONTENTS (Continued)

Section	Page
3.2 PRESSURE-IMPULSE CHARACTERIZATION FOR CHEMICAL SUBMUNITION 2	49
3.2.1 External Loads	49
3.2.2 Internal Loads	53
3.3 PRESSURE-IMPULSE CHARACTERIZATION FOR CHEMICAL SUBMUNITION 1	57
3.4 PRESSURE-IMPULSE CHARACTERIZATION FOR A LONG FLUID-FILLED CYLINDRICAL SHELL	63
3.5 PRESSURE-IMPULSE CHARACTERIZATION FOR FUZE PLUG RESPONSE	66
4 SCALING EVALUATION	75
5 CONCLUSIONS	79
6 REFERENCES	81
 Appendix	
A PRESSURE-IMPULSE CURVES FOR COMPLEX PULSES	A-1
B DERIVATION OF PRESSURE-IMPULSE RELATIONSHIP FOR A LONG FLUID-FILLED CYLINDRICAL SHELL	B-1
C TABLES OF TEST RESULTS	C-1
D EXPLOSIVELY ACCELERATED PLATE TESTS	D-1
E AIR GUN PERFORMANCE DATA	E-1

FIGURES

Figure		Page
S-1	Impact velocities to produce failure in Chemical Submunition 1 for different types of impacts (1.9-cm-thick, 8.9-cm-diameter impactors).....	v
S-2	PI curve for external side load Chemical Submunition 2.....	vi
1-1	Chemical submunition threat simulator.....	3
2-1	Fragment size distribution	7
2-2	Air gun facility for chemical submunition impact tests	11
2-3	Impulsive loading of submunitions using sheet explosive.....	13
2-4	Quasi-static loading of submunitions; $P = 92$ MPa	14
2-5	Mesh of the Submunition 2 and internal fluid used in the DYNA3D finite element calculations.....	16
2-6	Comparison of DYNA3D calculated and measured deformation in Test 13 (19-mm-thick steel plate impact at 204 m/s).....	18
2-7	Stress contours in Chemical Submunition 1 calculated with the L2D code for axial impact (1.9-cm-thick, 8.9-cm-diameter steel plate at 200 m/s)	19
2-8	Chemical Submunition 1 after fuze-end impact of a 1.85-kg mass at a velocity of 175 m/s (Test G-10).....	21
2-9	Chemical Submunition 1 after fuze-end impact of a 1.85-kg mass at a velocity of 198 m/s (Test G-9).....	22
2-10	Chemical Submunition 1 after fuze-end impact of a 1.85-kg mass at a velocity of 234 m/s (Test G-8).....	24
2-11	Chemical Submunition 1 after fuze-end impact of a 1.85-kg mass at a velocity of 326 m/s (Test G-7).....	25
2-12	Damage to Chemical Submunition 1 from side-on impact at midheight.....	28
2-13	Damage to Chemical Submunition 1 from side-on impact near top.....	29
2-14	Damage to Chemical Submunition 1 from oblique shoulder impact.....	30
2-15	Damage to welded Chemical Submunition 2 from side-on impact at midheight.....	31

FIGURES (Continued)

Figure		Page
2-16	Damage to welded Chemical Submunition 2 from side-on impact near top	32
2-17	Damage to Chemical Submunition 2 from oblique shoulder impact.....	33
2-18	Impact velocities to produce failure in Chemical Submunition 1 for different types of impacts (1.9-cm-thick, 8.9-cm-diameter impactors).....	34
2-19	Impact velocities to produce failure in Chemical Submunition 2 for different types of impacts (1.2-cm-thick, 8.9-cm-diameter impactors).....	35
2-20	Pressure-time histories at the rupture diaphragm produced by disk impact at the midheight of Chemical Submunition 2 (200 m/s).....	38
2-21	Damage to submunition from impulsive loading.....	40
2-22	Damage to submunitions from body-to-body impact.....	41
2-23	DYNA3D calculation of pressure loading on the side of Chemical Submunition 2	43
2-24	Body-to-body impact orientations	45
2-25	Damage to submunitions from cross-axis body-to-body impact.....	46
3-1	PI diagram for a responding structure such as a submunition (pressure = $P e^{-t/T}$, impulse = PT).....	48
3-2	Chemical Submunition 2 PI data for various side loading experiments.....	50
3-3	Calculated effect of impulse on internal pressure for side area loading of Chemical Submunition 2.....	51
3-4	PI curve for external side load for Chemical Submunition 2.....	52
3-5	Pressure histories calculated inside Chemical Submunition 2 for side area loading.....	54
3-6	Loading pulses for PI characterization.....	55
3-7	PI curve for external side load and internal fluid load for Chemical Submunition 2	56
3-8	PI curve for side impact plate loading experiments on Chemical Submunition 2	58

FIGURES (Continued)

Figure		Page
3-9	PI curve for axial loading on Chemical Submunition 2.....	59
3-10	PI data for side area oading of Chemical Submunition 1	60
3-11	PI data for side impact plate loading experiments on Chemical Submunition 1	61
3-12	PI curves for axial loading on Chemical Submunition 1.....	62
3-13	Plastic hinge mechanism that leads to diaphragm failure.....	64
3-14	Comparison of the PI curves calculated for the analytical model of burst diaphragm failure and the baseline PI curve for Chemical Submunition 2.....	67
3-15	Schematic of fuze removal mechanism	68
3-16	PI curves for fuze removal compared to baseline curve for Chemical Submunition 2	73
3-17	PI curves for standard and short fuze in Chemical Submunition 1	74
4-1	Comparison of damage in different sizes of Chemical Submunitions 2 subjected to side-on impact	76
A-1	Elemental displacements and forces.....	A-3
A-2	Pulse example.....	A-14
A-3	Fundamental pulse variation.....	A-19
A-4	Dimensionless PI curves.....	A-20
A-5	PI curve for burst diaphragm in Chemical Submunition 2	A-21
B-1	Plastic hinge mechanism that leads to diaphragm failure	B-2
B-2	Comparison of the PI curves calculated for the analytical model of burst diaphragm failure and the baseline PI curve for Chemical Submunition 2.....	B-12
B-3	Pressure-impulse relationships for a fully and partially loaded canister	B-16
D-1	Experimental setup for explosively accelerating steel plates	D-2
E-1	Gas gun velocity calibration curve	E-2

TABLES

	Page
2-1 Overall damage modes observed in sled tests	5
2-2 Pressure end loading calculations on Chemical Submunition 2	26
2-3 Plate impact calculations on Chemical Submunition 2.....	36
2-4 Pressude side area loading calculations on Chemical Submunition 2.....	42
4-1 Deformation and volume change measurements for Chemical Submunition 2 impact tests	77
C-1 Impact tests on Chemical Submunition 1	C-2
C-2 Impact tests on Chemical Submunition 2	C-5
C-3 Impact tests on scaled Chemical Submunition 2	C-7
C-4 Tests to define PI curve for Chemical Submunition 2	C-8
D-1 Test parameters for explosively accelerated steel plates.....	D-2
E-1 Gas gun velocity calibration curve	E-2

SECTION 1

INTRODUCTION

1.1 BACKGROUND.

Missiles with payloads comprising arrays of chemical submunitions are a key target in the Theater Missile Defense Program. To determine the response of such payloads to hit-to-kill vehicles, sled tests have been conducted at Holloman Air Force Base as part of a program conducted by the U.S. Army Strategic Defense Command (Mullins et al., 1992). Sled tests have been conducted at impact velocities up to 2 km/s to observe submunition response. State-of-the-art computer codes have also been used to calculate the response of the complete submunition array (Smith and Durham, 1993). However, neither approach allows a detailed investigation into the load and response of individual submunitions, particularly those that are away from the impact area where the impact velocities are reduced to hundreds of meters per second. Such submunitions are large in number and their fate often determines the damage to the overall array. Details of the loads applied to these submunitions are not available from sled tests, because such measurements are difficult and expensive to make. Similarly, in calculations performed to date, external loads on submunitions are difficult to predict because of the complex loading and response mechanisms for high velocity impacts and the fine zoning required with current limitations on computing power.

Understanding the relationship between loads and damage for these submunitions is useful in several ways. Load-damage relationships are useful for comparing loads required to produce damage under different impact conditions and for different submunitions (i.e., to provide a first order assessment of target hardness). Load-damage relationships are particularly useful as a framework to tie together results from different tests and analyses. Load-damage relationships that are simple in form can be used as essential input into lethality assessments where damage, which must be assessed for a range of parameters, is not feasible to be determined in sled tests or with detailed computer code calculations. Finally, a determination of load-damage relationships can link measurements made in sled tests and calculated in code calculations to final damage to individual submunitions. In many sled tests, measurements have been made of the internal pressure at the center of one or more submunitions. In calculations performed of the response of complete arrays, it is believed that the internal pressure can be calculated more accurately than many other response parameters. Thus, a determination of the load-damage relationships for chemical submunitions that includes internal pressure can link final damage to individual submunitions with measurements and calculations in complete submunition arrays. Then, load-damage relationships can be used in performing lethality assessments for many scenarios of interest.

1.2 OBJECTIVES.

The primary objective of the research reported here was to determine the load-damage relationships for individual Chemical Submunitions 1 and 2 (Figure 1-1) under a variety of load orientations and durations. The load-damage relationships should also relate externally applied loads to internal pressure to the extent possible. Secondary objectives were to determine the effects of ullage on submunition impact response, to determine the maximum velocity with which a surviving submunition can be ejected from the submunition array (for post-engagement analysis), to provide data for validating computer code calculations, and to evaluate scaling of chemical submunitions to impact response.

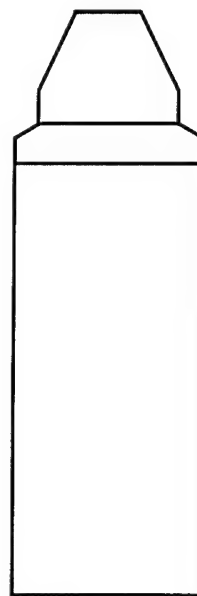
1.3 APPROACH.

To meet these objectives, we took a combined experimental and analytical approach that consisted of the following steps. First, we examined the submunitions damaged in some of the sled tests to determine the dominant damage mechanisms. Second, we performed experiments and analyses to investigate these mechanisms in more detail, to quantify the relationship between load and damage for particular cases of interest, and to determine the effect of ullage locations. We performed submunition to submunition impact tests to determine the maximum velocity at which a surviving submunition can be ejected from the submunition array. Next, we combined the load-damage relationships already determined for particular cases and performed additional experiments and analysis so that we could express the load-damage relations in terms of pressure-impulse (PI) characterizations for a variety of loading conditions of interest. Based on the observed damage mechanisms, we performed simplified analyses that allow prediction of the critical loads for target parameters other than those tested (e.g., for different submunition wall thicknesses).

To investigate scaling issues, we first compared the damage observed in the sled tests on submunition arrays conducted at Holloman Air Force Base with corresponding damage observed in quarter-scale array tests conducted at the Arnold Engineering Development Center. Then, we compared the responses of tensile and fracture tests on material specimens from the full-, half, and quarter-scale submunition and of carefully controlled impact, tests on single full-scale and corresponding half- and quarter-scale submunitions.



(a) Type 1



(b) Type 2

Figure 1-1. Chemical submunition threat simulators.

SECTION 2

CHEMICAL SUBMUNITION IMPACT RESPONSE

To investigate the impact response of chemical submunitions, we first examined the damage modes produced in the sled tests. We then performed both experiments and analyses to investigate and quantify the damage produced in these modes.

2.1 DAMAGE MODES OBSERVED IN SLED TESTS.

We visited Teledyne Brown Engineering in Huntsville, where we examined the damage to the submunitions from the sled tests conducted at Holloman Air Force Base. In these tests, a mock-up simulating a hit-to-kill projectile was accelerated by a rocket sled and impacted a target containing submunition threat simulators (hereafter referred to as submunitions). The objective of our examination was to identify the damage modes in the submunitions, particularly those modes that would result in release of the agent simulant.

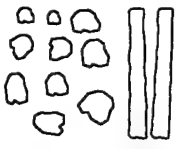
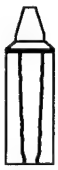
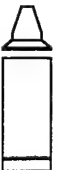
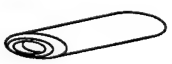
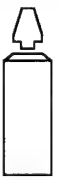
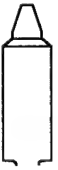
Overall damage modes for chemical submunitions were first identified. In some cases, we were able to observe macroscopic fracture surfaces that can indicate fracture initiation sites, crack propagation direction, types of loads driving the cracks, and the distribution of fragment sizes. At the end of this section, we discuss the implications of our observations.

Although both Type 1 and Type 2 chemical submunitions were examined, we concentrated our efforts on the damage modes and fragments in Type 1 chemical submunitions (see Figure 1-1), which were impacted at about 1.9 km/s. We examined Type 1 submunitions from Test 41I-E2, in which the target was impacted at the center of mass at a 10-degree angle of attack, and from Test 41I-F4, in which the axis of the target was parallel to the axis of the projectile, but was misaligned so that the projectile impacted the aft portion of the target.

In the description that follows, we generally progress from the area of direct impact (i.e., from the most severe damage) to the area farthest from the impact (i.e., to the least severe damage). Table 2-1 shows some of the common overall damage modes. Photographs of the damaged submunitions appear in Appendix B of Mullins et al. (1992). Each damage mode is discussed below.

In all three tests, the submunitions in the vicinity of the impact were heavily fragmented to the extent that the fragments could not be identified with the individual submunitions from which they came. Most of the fragments from both submunitions were "potato chip-shaped" portions of the case wall, but some fragments were portions of the base plate or portions of the fuze attachment section at the

Table 2-1. OVERALL DAMAGE MODES OBSERVED IN SLED TESTS.

Damage Mode	Figure from Reference*	Example from Submunition Threat Simulator No.	Comments
S  Severe fragmentation	B-2 B-11 B-15	(Cannot identify submunition threat simulators)	
A  Axial fracture	B-3 B-10 B-16	120 121 258 323 326	Multiple axial fractures
	B-11 B-16	266 330	Single axial fracture
	B-11a	265	Spiral fracture
C  Circumferential weld fractures	B-4 B-12 B-11 B-16	125 135 298 266 306 330	Usually accompanied by axial fractures or transverse crushing
L  Lateral crushing	B-4	135	
F  Fuse detachment	B-4 B-10 B-14	130 131 136 251 261 311	
D  Failure of burst diaphragm	B-10	254 260 253 261	Often accompanied by other failure modes

* S. E. Mullins, G. B. Booth, and C. S. Fowler, "ERINT Hit-to-Kill Sled Tests Against Chemical Submunition Targets (U)," Technical Report SEAS-SDC-3390, Teledyne Brown Engineering Report on Contract No. DASG60-92-C-0036 (October 1992). (SECRET)

submunition nose. Some fragments were strips, formed from axial fractures that ran down most or all of the length of the submunitions that had length-to-width ratios greater than 5. However, strips were rarer than potato chips.

Figure 2-1 plots the distributions as cumulative number of fragments, $N_g(R)$, versus fragment size, R , where $N_g(R)$ is the number of fragments with sizes greater than R . We believe that the lack of fragments with sizes less than 1 cm is real, because there was no evidence of the production of fine fragments. Furthermore, fine fragments would not be expected in such ductile material at the loading rates involved.

In all tests, at a distance away from the direct impact area, we also found large fragments of submunitions formed by a few axial fractures, most of which began at the weld zone at the top (fuze) end of the submunition and ran down all or part of the length of the submunition. In some submunitions, axial fractures did not propagate the entire length of the submunition or were joined with spiral fractures. We believe that the axial cracks are initiated by ovalization or denting of the end of the cylinder.

Another common damage mode is a circumferential failure at the shoulder of the submunition, where the top is welded to the cylinder. The top can be separated from the cylinder by axial impact, impact at an oblique angle to the axis, or lateral impact. In axial impact, a fragment hits the fuze axially and deforms it plastically. The resulting axial loads induce bending in the top cover and expansion (mushrooming) of the end of the cylinder until the welded joint cracks along the circumference and the cover separates. These circumferential fractures apparently occurred in all the submunitions that were either severely fragmented or that suffered at least one axial fracture over the entire length of the cylinder. As the direction of impact shifts from an axial orientation to an oblique angle to the axis, the mechanism shifts from mushrooming to ovalizing the cylinder. This inward deformation induces circumferential cracks in the weldment (and separation of the cover), as well as radial cracks in the cover itself (and the fragmentation of the cover). Separation of the top welded cover was often accompanied by circumferential failure at the weld between the cylindrical portion of the main body and the bottom of the submunition. In a direct lateral impact (fragment impacting at about midheight with the impact velocity along a radial direction), the top can be removed by bending along the axial direction over the top piece.

The most likely mechanism for the separation of the bottom closure plate is the ovalization of the submunition case by a lateral impact or by impact at an oblique angle to the axis similar to that described above for removal of the top cover, except with the impact point near the bottom of the case. As a result of ovalization, the brazed or welded joint at the bottom of the submunition fractures and the closure plate is forced out and/or fractured.

A lateral fragment impact on a submunition (i.e., a fragment impacting at about midheight, with the impact velocity along a radial direction) will cause ovalization of the cylinder (frequently accompanied by

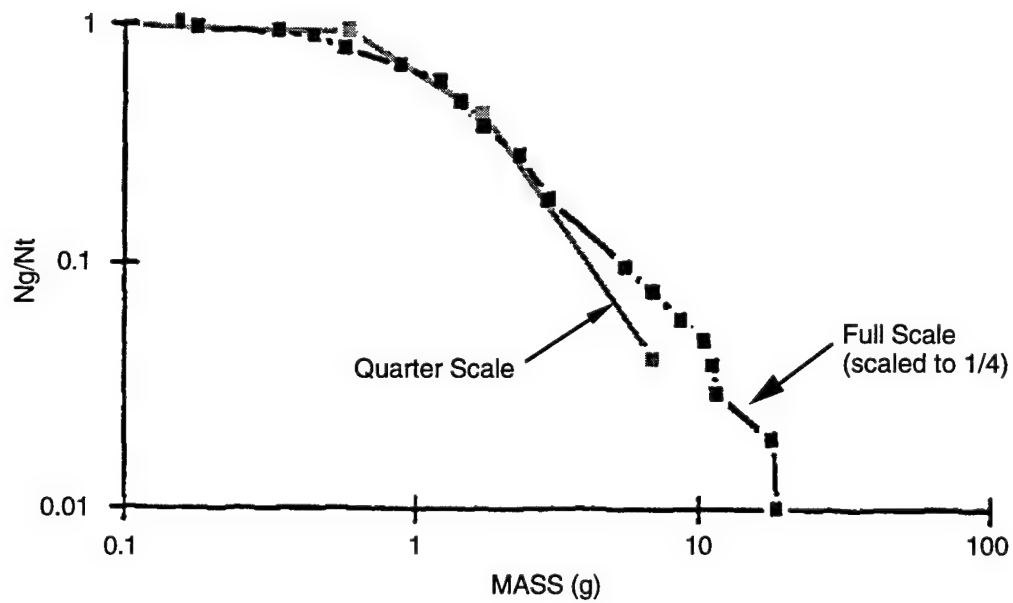


Figure 2-1. Fragment size distribution.

circumferential cracks in the weld and separation of the cover). We also observed part-cylindrical dents running the full length of a submunition, clearly showing that it had been impacted by another undamaged or only partially damaged submunition.

We observed evidence for several mechanisms that can lead to the removal of the fuze. First, the fuze can be directly impacted by a fragment, and the resulting compression and bending loads force it out of the threaded region at the top of the submunition. The fuze then bears some dents, as evidence of the impact, and its threaded bottom part is bent, shreaded, or both. A second mechanism involves no direct impact on the fuze but an oblique impact on the top of the submunition. The resulting deformation of the welded cover ovalizes the threaded fuze-cover attachment region and squeezes out the fuze. In this case, the fuze does not bear any evidence of impact, but its threaded base is bent and ovalized and some of the threads may be stripped. A third scenario involves a side impact of the submunition: the resulting translational and/or rotational motion of the submunition and inertial forces cause enough bending at the threaded base to force out the fuze. In this case, the fuze sustains very little damage except to the threads.

The last common damage mode was failure of the burst diaphragm. The burst diaphragm can be sheared and ejected by the buildup of internal pressure (due to impact and deformation of the case), while the closure plate remains attached to the submunition. This failure mode is often accompanied by other failure modes.

Most of the observed shock tubes were completely flattened, probably by the internal pressure buildup. Side impact on the submunition and inertia can also cause the shock tubes to bend along the axial direction and to separate from the fuze. The bottom extremities of some tubes clearly show dent marks, which resulted from impact with the internal case wall.

Overall, Chemical Submunitions 1 and 2 undergo the same material and structural damage modes, and we believe that the mechanisms driving these modes are also the same. One difference between the two submunitions is that, because of its stubbier design, the fuze of Submunition 2 does not fail as frequently as that of Submunition 1. The larger case length-to-diameter ratio in Submunition 2 may also make some failure modes more likely than others and may require different critical conditions. For example, the smaller diameter of the case may make the top and bottom region stiffer; hence, higher impulses or forces may be required to separate the top and the bottom from the cylinder.

2.2 PROCEDURES FOR SINGLE SUBMUNITION EXPERIMENTS.

2.2.1 Submunitions.

We performed tests on Chemical Submunitions 1 and 2. At full-scale, Chemical Submunition 1 is 9 cm (3.54 inches) in diameter and 32.5 cm (12.8 inches) long including the fuze. Chemical Submunition

2 is 6.4 cm (2.50 inches) in diameter and 32.8 cm (12.9 inches) long. All full-scale submunitions were obtained from Battelle Memorial Institute, Huntsville, Alabama, and were fabricated in the same way as the submunitions used in the sled tests. We obtained half-scale Chemical Submunition 2 models from Battelle or directly from their subcontracted machine shop located in Huntsville. The half-scale models were used primarily so that we could conduct submunition to submunition impact tests using the six-inch air-driven gun described below. For consistency, we used half-scale models in other tests also. We obtained the quarter-scale Chemical Submunition 2 models from General Research Corporation (GRC) in Santa Barbara, California. Quarter-scale tests were performed only to assess scaling effects.

The bottom of each submunition has an end that tapers down to an opening sealed with a burst diaphragm. For Chemical Submunition 1, the diaphragm is 4.8 cm (1.9 inch) in diameter and for Chemical Submunition 2 it is 2.2 cm (0.875 inch) in diameter (full-scale). Each submunition is fitted with a shock tube that is attached to the fuze. In actual operation, the shock tube is filled with an energetic material that is initiated by the fuze and pressurizes the chemical agent, which then bursts the diaphragm. In our impact tests, as in most of the sled tests, the submunitions were filled to 95% of their capacity with water (5% ullage) to simulate the agent. The total mass for Chemical Submunition 1, including water, was 6.4 kg. The hydrostatic pressure that produces diaphragm bursting was reported by Battelle to be 27 to 41 MPa (4000 to 6000 psi) in Chemical Submunition 1. We measured burst pressure in Chemical Submunition 2 to be 41 MPa (6000 psi). We measured burst pressure in the half-scale Chemical Submunition 2 to be 90 MPa (13,200 psi). The burst pressure in the quarter-scale Chemical Submunition 2 was measured by GRC to be about 31 MPa (4600 psi).

Full-scale submunitions are constructed with welds that attach the top end and the tapered bottom to the cylindrical portion of the submunition. The top end of Chemical Submunition 1 is conical in shape with the simulated fuze plug threaded into a hole in the conical end. Thus, Chemical Submunition 1 has sloped shoulders on the fuze end. In contrast, Chemical Submunition 2 has a flat end to accommodate the fuze plug; the shoulder is slightly rounded. The welds attaching the bottom section of each submunition model generally were strong enough not to fail in our tests. The top welds on both full-scale model submunitions did, however, fail in several tests. The top welds in full-scale Chemical Submunition 1 were not full-penetration welds. Rather, they began on the outside surface of the submunition and penetrated not more than half the thickness of the wall. The welds in full-scale Chemical Submunition 2 models were full-penetration welds. To investigate the effect of these top welds on Chemical Submunition 2, two corresponding full-scale, unwelded, Chemical Submunition 2 models were specially fabricated at SRI. We machined them from thick-walled tubing. On most of the half-scale models, the tops were welded to the body with full-penetration welds. The bodies of a few half-scale models were machined from solid bar stock so that the upper end of these models had no welds. Similarly, the quarter-scale

models had no welds but were machined from solid rods. The bottom tapered end of the quarter-scale models was threaded into the cylindrical portion.

2.2.2 Loading Techniques.

The majority of the tests performed were impact tests. We impacted individual submunitions with a plate or with another submunition. Preliminary tests were performed with plates accelerated by explosive; the details of this loading technique are presented in Appendix D.

For the sizes, shapes, and velocities of impactors needed to damage the submunitions with plate and submunition-to-submunition impact, we found that the most suitable technique was to accelerate the impactor with a 15.2-cm-diameter (6-inch) air-driven gas gun (Figure 2-2). In early air gun tests, we used polyethylene bottles filled with foam as sabots to hold the steel plate impactors. However, for impact velocities above 100 m/s, the gun was operated at pressures above 0.34 MPa (50 psi). At these pressures, we found that the sabots deformed, creating misalignment of the plate with the target. To prevent this problem, we fabricated sabots from aluminum. The aluminum sabots withstand the maximum pressure for which the gun was designed 3.4 MPa. Sabots hold the steel impactors until they exit the muzzle of the gas gun. The sabots were stripped from the impactors by means of a thick steel ring, which stopped the sabot, leaving the plate impactor to strike the target.

For body-to-body impacts, the half-scale impactor was lightly bonded to the front of the sabot. The sabot was stripped away from the impactor by two thick steel blocks placed so the impactor would pass between them. For tests where the target was impacted axially, the target was placed on its side in alignment with the axis of the air gun. In this orientation, the ullage volume would be distributed along the top side of the model. For tests where the target was impacted on the side either by a plate or by another submunition, the target was positioned on end so that the fuze end was pointing up. Here, the ullage volume was at the fuze end. In preliminary gas gun tests, we determined the practical maximum velocity for a 1.85-kg plate to be about 330 m/s. More complete gun calibration data are given in Appendix E.

For impact tests, test parameters included the mass of the impacting plate and the velocity of impact. Orientation of the model was also an important parameter. As mentioned above, models were loaded either on the fuze end or along the side. A few tests were conducted where the model was impacted at an angle with the plate impacting the shoulder of the model. For these tests, the plate was cut-off along two parallel sections, so that the plate initially contacted only the shoulder of the submunition. Limited impact tests were also conducted where the ullage volume and location was a parameter.

Experiments were also conducted on half-scale models of Chemical Submunition 2 canisters. We chose this scale so that complete submunitions could be launched in the air-driven gas gun. For the

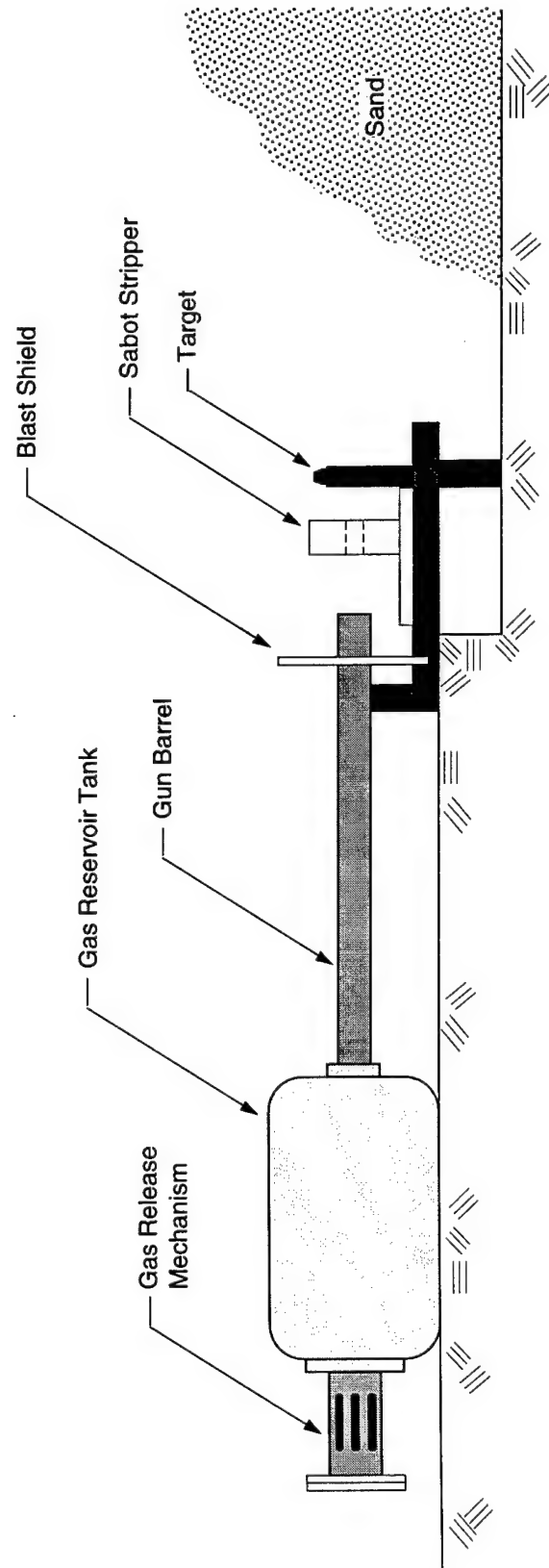


Figure 2-2. Air gun facility for chemical submunition impact tests.

experiments, three different loading durations were produced by three different loading techniques: sheet explosive tests produced short duration loads, submunition-to-submunition impacts produced intermediate duration loads, and static compression tests produced long duration loads.

For short duration impulsive loading, a uniform sheet explosive load was applied over $\pm 40^\circ$ on one side of the submunition, as shown in Figure 2-3. The fuze was not loaded. A layer of half-inch-thick foam neoprene was placed between the explosive and the submunition to suppress any damage from the direct shock wave. Thus, any damage observed was caused by a later time structural response. Sheet explosive thickness was selected to provide loads that bracket canister damage from slight deformation of the loaded surface to diaphragm rupture and fuze removal. Impulses imparted to the target submunition from direct explosive loading are well known and reproducible (Lindberg and Colton, 1970).

For quasi-impulsive loading, the side of each target canister was impacted by another submunition at velocities from 100 to 230 m/s. This impact loading is similar to the plate impactor tests, except that the impactor is another submunition.

For quasi-static loading, a load was applied to two sides of a submunition by compressing it between two steel platens, as shown in Figure 2-4. The steel platens extend over the entire length of the model so that the ends of the model, which are stiffer than the central portion, carry much of the crush load.

2.2.3 Measurement Techniques.

2.2.3.1 Velocity Measurement. Impact velocity was measured with an optical system installed in the barrel of the gun. Two optical stations were used, one 10.2 cm (4 inches) from the end of the barrel and one 12.7 cm (5 inches) from the end. At each station, a light source illuminated the sabot as it passed the measurement point. A fiber optic light sensor was embedded in the light source. When the light reflected off the sabot, the fiber optic sensor would convert this light into a signal that was recorded on a digital scope. To enhance this measurement technique, the sabot was marked with reflective tape. Two intervals of reflective tape each 2.54 cm long, were separated by nonreflective (black) tape. As the sabot passed the fiber optic sensor, the alternating light and dark surfaces were registered, giving a reliable measurement of the exit velocity of the sabot and impactor.

2.2.3.2 High-Speed Photography and Video. In some tests, submunition response and imparted velocity were measured with a Hycam running at 500 frame/s. In some tests, high-speed video was used to record the response. Framing rates for the video were 1000 to 2000 frame/s.



Figure 2-3. Impulsive loading of submunitions using sheet explosive.

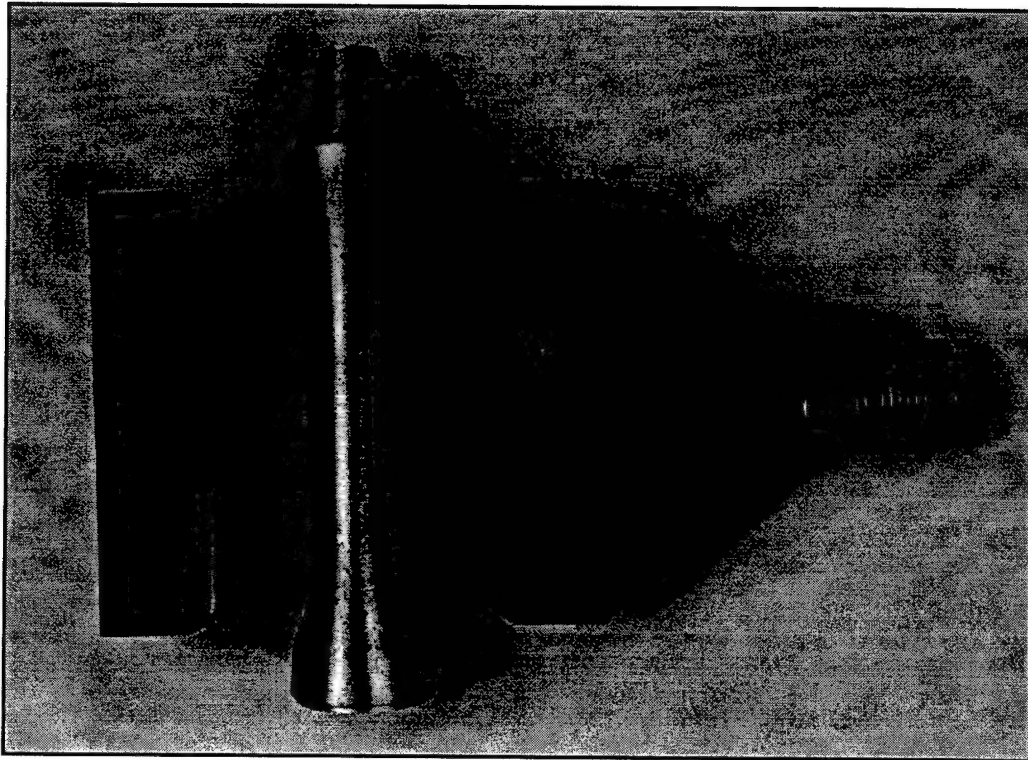


Figure 2-4. Quasi-static loading of submunitions; $P = 0.92$ kbar.

2.3 PROCEDURES FOR SINGLE SUBMUNITION CALCULATIONS.

2.3.1 DYNA3D.

We performed finite element calculations of the submunition for various loading conditions to help in experiment planning and interpretation, to investigate responses for loading conditions not tested, and to relate the external loads to the internal loads. Most of these submunition response calculations were performed using the DYNA3D finite element code developed at Lawrence Livermore National Laboratory (Whirley, 1993), DYNA3D is an explicit, nonlinear, three-dimensional finite element code for analyzing the large deformation dynamic response of solids and structures. The equations of motion are integrated in time by using the central difference method. Spatial discretization is achieved with eight-node solid hexahedron (brick) elements.

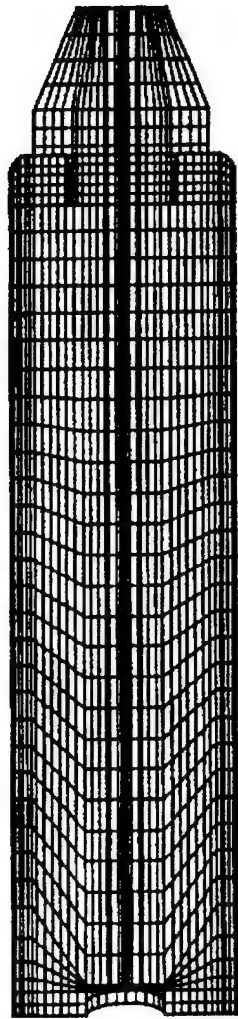
All of the DYNA3D calculations were performed for Chemical Submunition 2, using the full-scale submunition dimensions (6.35 cm outer diameter). All of the calculations had at least one plane of symmetry through the axis of the submunition, which was used to reduce the calculation size by a factor of 2. The mesh used in the calculations contained 4864 elements for the submunition and fuze and 4004 elements for the internal fluid and is shown in Figure 2-5. The behavior of the circumferential weld near the shoulder of the submunitions was not sufficiently characterized to be incorporated into the model and therefore was neglected. This will result in conservative estimates of submunition lethality by eliminating a potential weak point in the structure.

The fuze cap was modeled, but the detonator and shock tube were neglected since the only fuze failure mode considered in the calculations was separation of the fuze from the submunition body. The threshold connection between the fuze cap and submunition body was modeled with a region of fuze material that had a stiffness and strength approximately one-half that of the submunition steel combined with a tied sliding interface with failure. Separation of the fuze and submunition is allowed after the interface failure criterion is exceeded. The failure criterion used in the calculations was

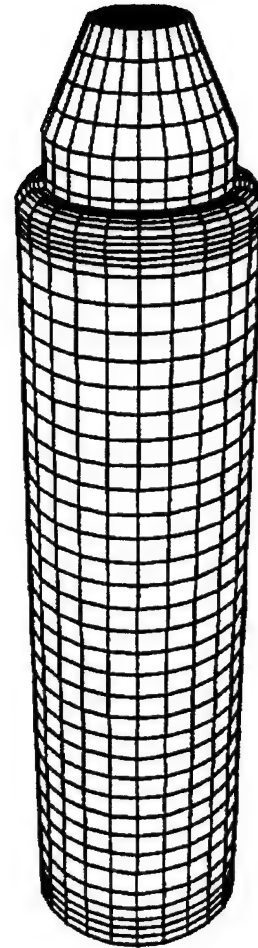
$$(\tau/T)^2 + (\sigma/N)^2 \geq 1 \quad (2.1)$$

where τ = shear stress, σ = normal stress, and $T = N = 350$ MPa. The values of T and N were chosen based on comparisons of the initial simulations with results of the plate impact experiments.

The submunition was modeled using an isotropic, elastic-plastic, hydrodynamic, constitutive model (model number 10 in DYNA3D) with a yield strength of 670 MPa and the plastic hardening stress-strain behavior specified in tabular form. The water was modeled with the fluid constitutive model (model number 9 in DYNA3D) with a viscosity of 1.0 cP and a linear pressure volume relationship with a bulk



(a) Mesh cross section through the symmetry plane showing internal mesh resolution



(b) Mesh reflected about the symmetry plane showing external canister geometry

Figure 2-5. Mesh of the canister and internal fluid used in the DYNA3D finite element calculations.

modulus of 2.07 GPa. Modeling fluid response at a free surface (such as that produced by the ullage) can produce difficulties in Lagrangian finite element codes (like DYNA3D) if splashing or significant flow occurs producing large distortion of elements.

To eliminate this problem in the calculations, we smeared the ullage/water interface, creating a region of water with porosity. Specifically, for a submunition with 5% ullage, the model included a region of 20% of the submunition volume that contained water with 25% porosity and a region of 80% of the volume that contained water with no porosity. Figure 2-6 shows a comparison between a DYNA3D calculation and a corresponding experiment.

2.3.2 L2D.

We used the L2D code to model end impact of Chemical Submunition 1 (Cooper, 1980). All such calculations were axisymmetric. L2D code is a two-dimensional, Lagrangian, continuously rezoned code. The advantage of L2D over other comparable codes is in its rezoning scheme. It uses a Free Lagrange method with quadrilaterals instead of triangles. Triangular elements are used to simplify connectivity problems that occur in mesh generation and in the rezoning algorithms. However, the code minimizes the number of triangles by converting pairs of triangles into quadrilaterals. This produces more economical solutions and reduces potential numerical problems introduced by triangular elements. The rezoning operations consist of reconnecting the mesh, deleting nodes, creating nodes, and relocating a node to a better position. Mass, momentum, and total energy are conserved in the rezoning.

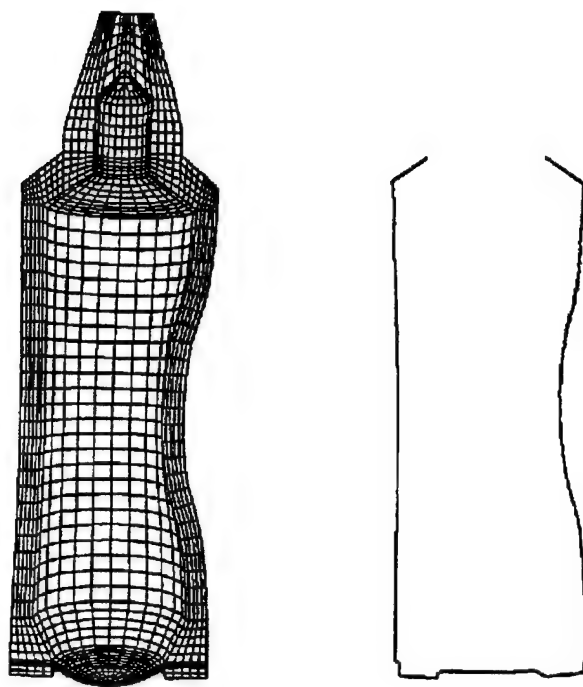
We performed two types of L2D calculations on Chemical Submunition 1. First, a series of calculations was performed for plate impact on the fuze. Figure 2-7 shows typical results of one such calculation in which the impact velocity was 200 m/s. The characteristic load duration was 80 μ s. The maximum stress occurs at the top of the cylindrical portion of the submunition due to combined bending and hoop tension induced by flattening of the conical end.

In the second type of calculation, the fuze was replaced by a plate flush with the fuze opening. Pressure loading was applied to the entire top surface of this submunition. This loading represents loads that would be produced by a debris cloud that impacted the entire end of the submunition. In all cases, the maximum stress occurred at the top of the cylindrical portion of the submunition.

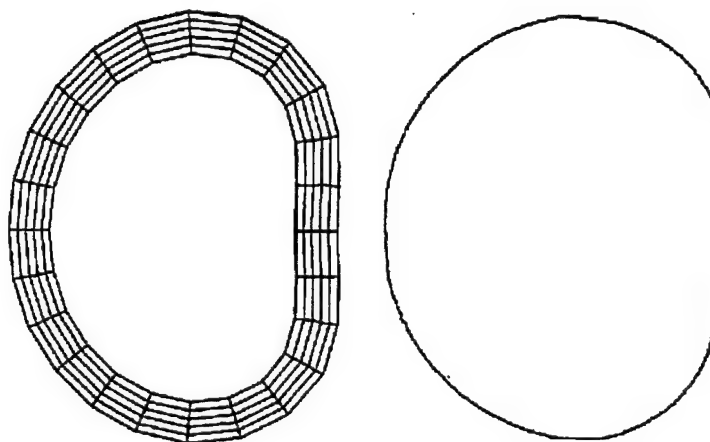
The results of both the DYNA3D and the L2D code calculations are presented in Section 3.

2.4 SUBMUNITION RESPONSE TO LOCALIZED LOADING.

We performed experiments and calculations to determine the response of localized loading, such as plate impact, on Chemical Submunitions 1 and 2. In actual scenarios, the plate loading represents loading produced by an array of fragments on the target submunition that is partially shielded by other



(a) Side view



(b) Cross-section

Figure 2-6. Comparison of DYNA3D calculated and measured deformation in Test 13 (19-mm-thick steel plate impact at 204 m/s).

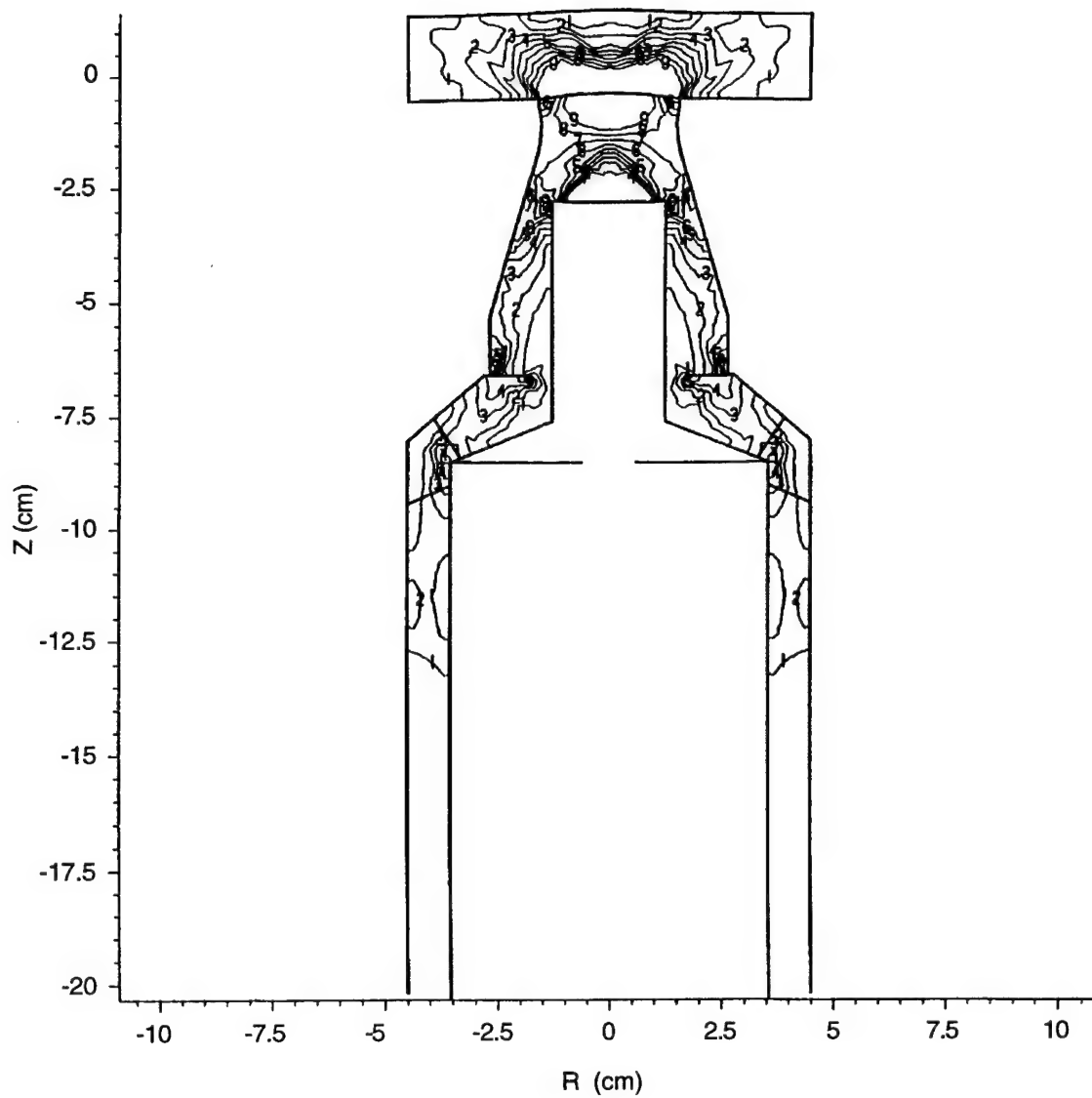


Figure 2-7. Stress contours in Chemical Submunition 1 calculated with the L2D code for axial impact (1.9-cm-thick, 8.9-cm-diameter steel plate at 200 m/s).

submunitions, the impact of the end of one submunition into the side of the impacted submunition, or large fragments from parts of the target other than the submunitions or from the projectile itself. We present the results of the experiments and calculations in the remainder of this section. Interpretation of the results is given in Section 3.

2.4.1 Axial impact.

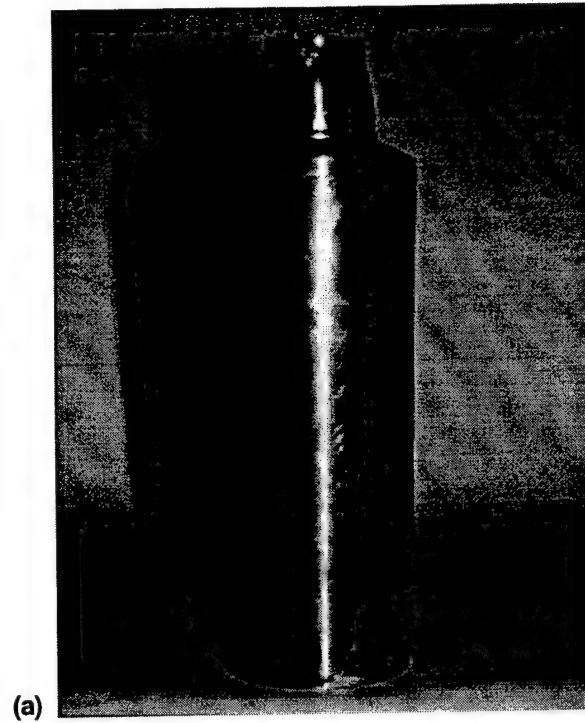
To see the progression of damage observed in one type of localized loading, we first describe a series of axial impact experiments on Chemical Submunition 1 at progressively higher velocities. In all the tests, the steel impactor plate was 8.9 cm in diameter and had a mass of 1.85 kg.

In Test G-10, the plate velocity was 175.2 m/s (total momentum of 3.2×10^7 dyne•s). For loading over the 2.3-cm-diameter fuze end, the specific impulse was 7800 ktaps.* We used high-speed photography to measure a post-impact velocity of the submunition of 43.5 m/s, which corresponds to a total impulse of 2.8×10^7 dyne•s imparted to the submunition. In this test, shown in Figure 2-8, no pieces broke away from the body of the submunition and all of the water remained within the submunition. As for all tests in this series, conservation of momentum shows that the plate must have rebounded from the submunition on impact.

The impact caused severe deformation of the fuze, which expanded significantly and shortened from 6.4 cm initial length to 4.5 cm average final length (1.9 cm shortening), as shown in the figure. In this test, the impact also caused the cone to flatten and the top end of the cylindrical body to bulge or mushroom. The overall shortening of the conical end and cylindrical body was 0.2 cm; thus, the total shortening of the submunition was 2.1 cm. The final diameter of the mushroomed end was 9.1 cm (2.2% expansion). An incipient crack in the weld between the conical end and the cylindrical body extended more or less continuously around half of the circumference but did not extend through the entire thickness. The impact also produced axial cracks that emanated from the circumferential crack; these axial cracks were spaced about 1.5 cm apart but generally extended only about 0.7 cm. The damage of interest here appears to be near the threshold of crack initiation.

In Test G-9, the measured plate velocity was 198.4 m/s (total momentum of 3.7×10^7 dyne•s). For loading over the 2.3-cm-diameter fuze end, the specific impulse was 8800 ktaps. We used high-speed photography to measure the post-impact velocity of 53.4 m/s, which corresponds to a total momentum of 3.4×10^7 dyne•s imparted to the submunition, again indicating plate rebound. In this test, as shown in Figure 2-9, no pieces broke away from the body of the submunition and all of the water remained within the submunition.

*1 ktap = 100 MPa-μs, 1 tap = 1 dyne•s/cm².

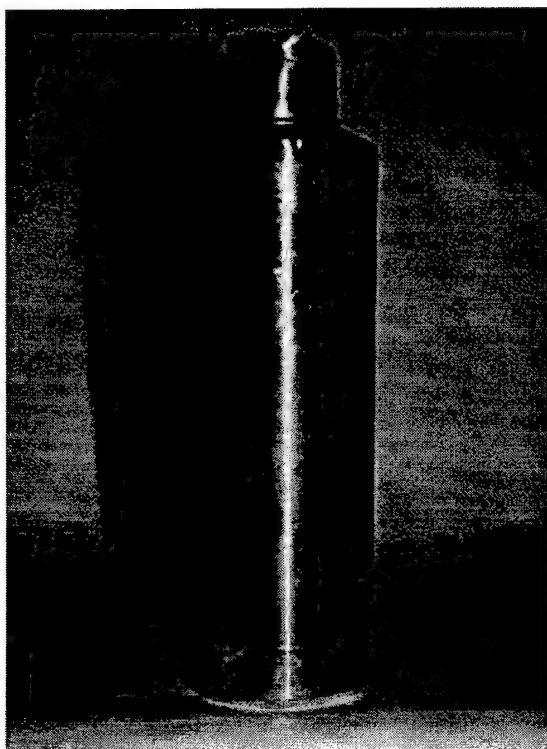


(a)

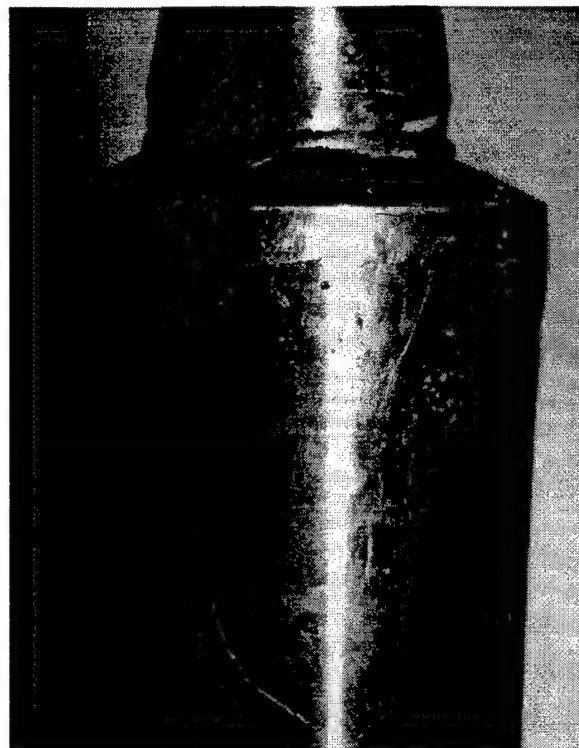


(b)

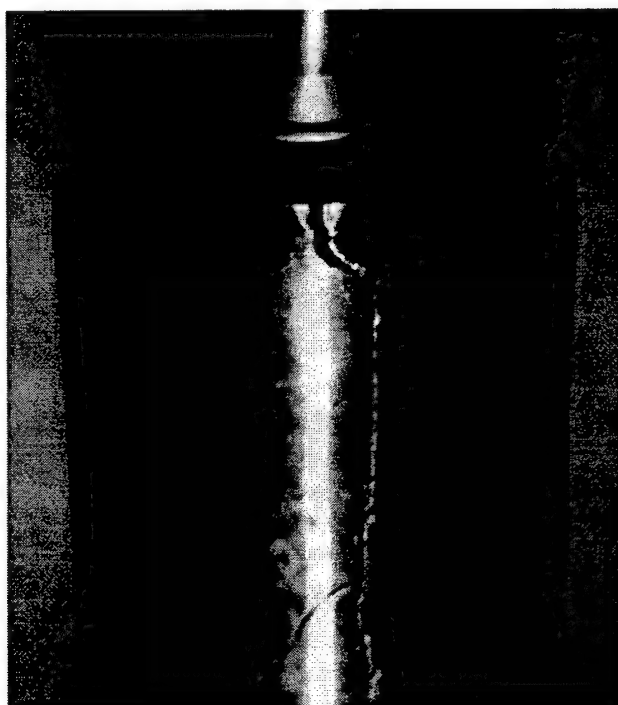
Figure 2-8. Chemical Submunition 1 after fuze-end impact of a 1.85-kg mass at a velocity of 175 m/s (Test G-10).



(a)



(b)



(c)

Figure 2-9. Chemical Submunition 1 after fuze-end impact of a 1.85-kg mass at a velocity of 198 m/s (Test G-9).

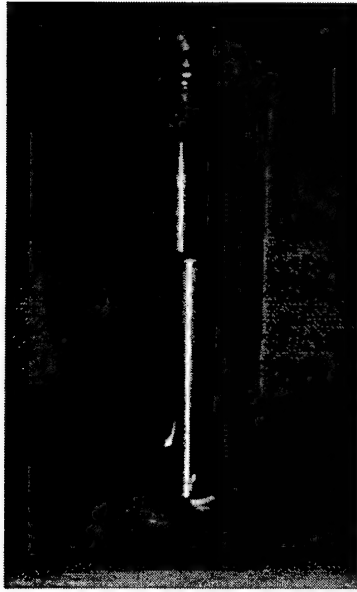
The impact caused significant deformation of the fuze. It expanded significantly and shortened from 6.4 cm initial length to 3.6 cm average final length (2.8 cm shortening), as shown in Figure 2-9. The impact also caused the conical top end of the submunition to flatten and the top end of the cylindrical body to bulge or mushroom. The overall shortening of the conical end and cylindrical body was 0.3 cm; thus, the total shortening of the submunition was 3.1 cm. The final diameter of the mushroomed end was 9.2 cm (3.4% expansion). A crack in the weld between the conical end and the cylindrical body extended more or less continuously around the entire circumference but did not extend through the entire thickness. The impact also produced axial cracks that emanated from the circumferential crack; these axial cracks were spaced about 1.5 cm apart and generally extended about 1.4 cm. Two of the axial cracks (about 120° apart) extended 5 cm axially, then branched into twin cracks that continued to extend as much as 12 cm. The response of interest here, shown in Figure 2-9(c), appears to be slightly above the threshold of crack initiation.

In Test G-8, the measured plate velocity was 233.6 m/s (total momentum of 4.3×10^7 dyne•s). For loading over the 2.3-cm-diameter fuze end, the specific impulse was 10,400 ktaps. We used high-speed photography to measure the post-impact velocity of 63.3 m/s, which corresponds to a total momentum of 4.1×10^7 dyne•s imparted to the submunition. This momentum is based on the entire submunition and fluid mass and is an upper bound, because the submunition fragmented and lost its water (and hence an unknown portion of its mass) within 8 ms of impact but before the velocity was measured. Therefore, the measured velocity corresponds to some smaller unknown mass and associated momentum.

The impact caused the fuze to deform and fail as shown in Figure 2-10. In this test, the impact also caused the body of the submunition to fracture into several pieces. The main piece that broke away from the body of the submunition was recovered, but the remaining pieces from the conical end could not be found. The fragmentation was initiated by three major axial cracks approximately evenly spaced around the submunition. These cracks joined the circumferential crack between the conical end and the cylindrical body. The three major axial cracks apparently extended axially for 5 cm and then branched into multiple cracks. The cracking along the weld region traveled around the entire submunition, with failure through the entire thickness along only one-third of the circumference.

In Test G-7, the plate velocity was 325.6 m/s (total momentum of 6.0×10^7 dyne•s). For loading over the 2.3-cm-diameter fuze end, the specific impulse was 14,500 ktaps. We used high-speed photography to measure a post-impact velocity of 87.1 m/s. This value is also an upper bound, because the photographic coverage showed that within 5 ms of impact the submunition fragmented and lost its water before the velocity was measured.

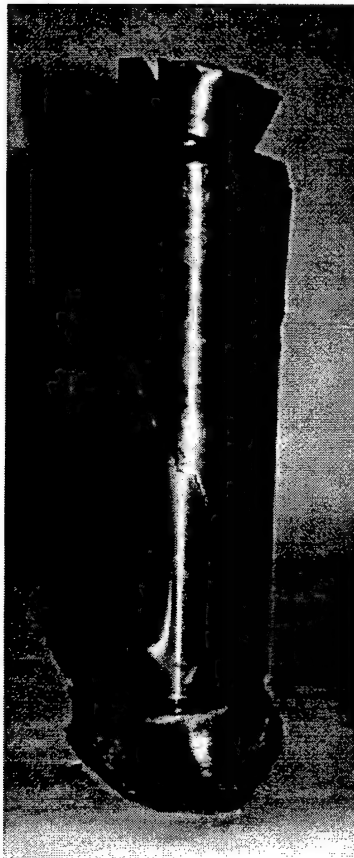
The damage shown in Figure 2-11 is the greatest response of interest. The impact caused severe deformation of the fuze. It shortened until the tip of the fuze sheared off around the internal bore, resulting



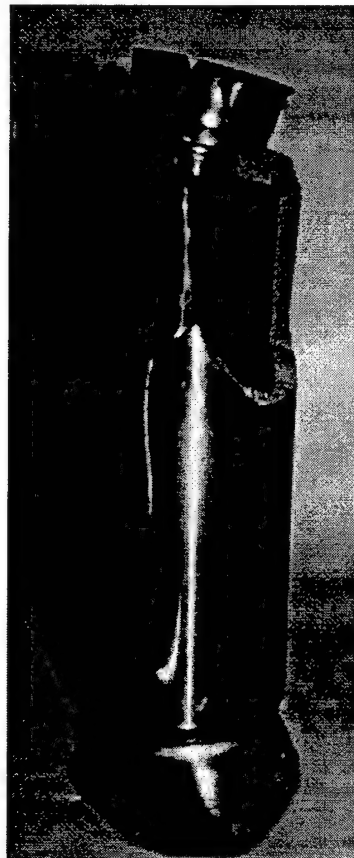
(a)



(b)

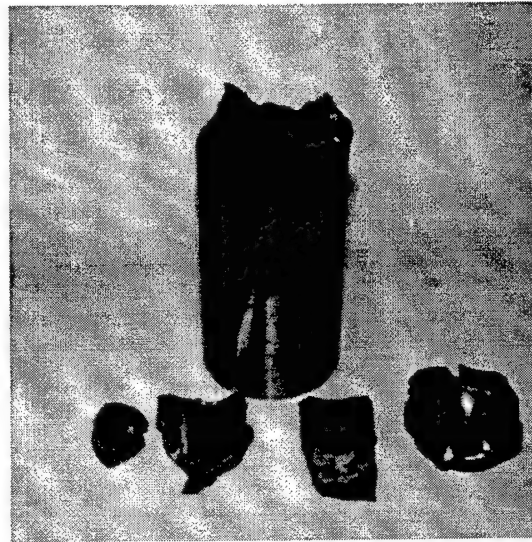


(c)



(d)

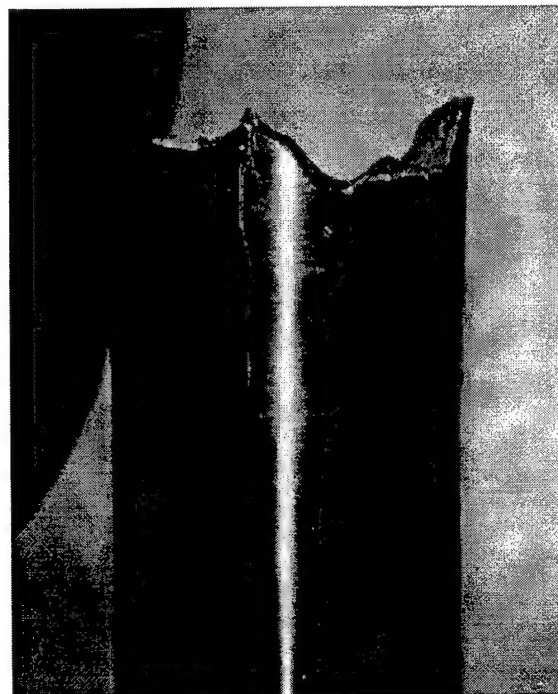
Figure 2-10. Chemical Submunition 1 after fuze-end impact of a 1.85-kg mass at a velocity of 234 m/s (Test G-8).



(a)



(b)



(c)

Figure 2-11. Chemical Submunition 1 after fuze-end impact of a 1.85-kg mass at a velocity of 325 m/s (Test G-7).

in complete failure of the fuze, as shown in the figure. In this test, the impact also caused the body of the submunition to fracture into multiple pieces. Three of the pieces that broke away from the body of the submunition were recovered, but the remaining pieces could not be found. The fragmentation was initiated by three major axial cracks approximately evenly spaced around the submunition. These cracks joined the circumferential crack along the weld between the conical end and the cylindrical body. The three major axial cracks apparently extended axially for 12 cm and then turned to about a 45° angle and extended an additional 3 cm.

2.4.2 Calculations of Axial Loading Response.

We performed DYNA3D calculations to investigate in more detail the response of Chemical Submunition 2 and to enhance our understanding of the load-damage relationship. Because the load-damage relationship does not depend on how the loads are generated, we selected loading that was most convenient to analyze. For most calculations, the load was specified as a pressure time history that was a square pulse (constant pressure) of varying durations.

We performed one set of calculations to investigate the effects of an end pressure load acting on the fuze of Chemical Submunition 2. The spatial distribution of the load was a flood load over the exposed end area, with the pressure magnitude scaled by the cosine of the surface normal vector to the axis of the submunition. Table 2-2 provides a summary of these end loading calculations.

Table 2-2. Pressure end loading calculations on Chemical Submunition 2.

Calculation Number	Peak impulse (ktaps)	Load Duration (μs)	Peak Pressure (MPa)	Canister Shoulder Strain (%)	Diaphragm Strain (%)	Notes
Can10a	600	10	600	45	12	
Can10b	400	10	400	20	7.5	
Can10c	300	10	300	10	4.5	
Can10d	2700	900	300	1.3	1.2	
Can10e	4050	900	450	6.0	3.0	
Can10f	5400	900	600	35	3.5	
Can10g	800	100	800	13	8.0	
Can10h	1000	100	100	23	7.0	

The failure mechanism predicted by these calculations is a circumferential failure through the submunition wall, below the shoulder, near the weld location, in the submunitions used in the experiments. The average plastic strain magnitude through the submunition wall at this location is given in column 5 of Table 2-2. The critical strain for failure was taken as 20%.

2.4.3 Other Plate Impact Experiments.

We conducted several other plate impact experiments on Chemical Submunitions 1 and 2. The tests consisted of striking submunitions with circular steel plates in prescribed orientations and velocities. The plates all had a diameter of 8.9 cm. Plate thickness ranged from 9 to 38 mm for Chemical Submunition 1 and from 6 to 24 mm for Chemical Submunition 2. Impact orientations included end-on onto the fuze end of the submunition, side-on onto the center of the submunition, side-on onto the shoulder of the submunition, and at oblique angles onto the shoulder of the submunition.

Table C-1 (in Appendix C) summarizes the test series performed on full-scale Chemical Submunition 1. Most of the damage modes observed in the sled tests were observed in the single submunition tests. Lateral crushing of the submunition body was not observed, since this mode is probably achieved in submunition-to-submunition impact. Figures 2-12 through 2-14 show typical damage to Chemical Submunition 1 for three of the impact orientations tested.

Table C-2 summarizes the test parameters for the series of tests performed on full-scale Chemical Submunition 2. Figures 2-15 through 2-17 show typical damage to Chemical Submunition 2 for three of the four impact orientations considered. Lethal damage was not demonstrated for end-on impact of this submunition.

Figures 2-18 and 2-19 summarize the impact velocities required to cause fluid leakage in Chemical Submunitions 1 and 2. Both submunitions are strongest against end-on loading because of the fuze and weakest in shoulder loading because of the weld.

2.4.4 Other Plate Impact Calculations.

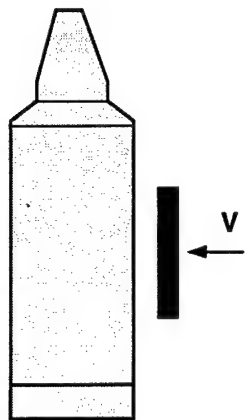
We performed a series of plate impact calculations to investigate the side impact response for Chemical Submunition 2 for a greater variety of impactor sizes, shapes, impact positions, and velocities than could be investigated experimentally. Table 2-3 gives a summary of these calculations.

These calculations were performed using the baseline plate dimensions, which had the same impact length, thickness, and mass as the 12-mm-thick impact plates used in the experiments. The remainder of the plate impact calculations were then performed with no ullage volume, which slightly overestimates damage but eliminates any variation that might occur with ullage volume fraction or position as an

Impact Test 15

Impactor Velocity (V) = 273 m/s

Impactor Mass = 942 g



Impact Orientation

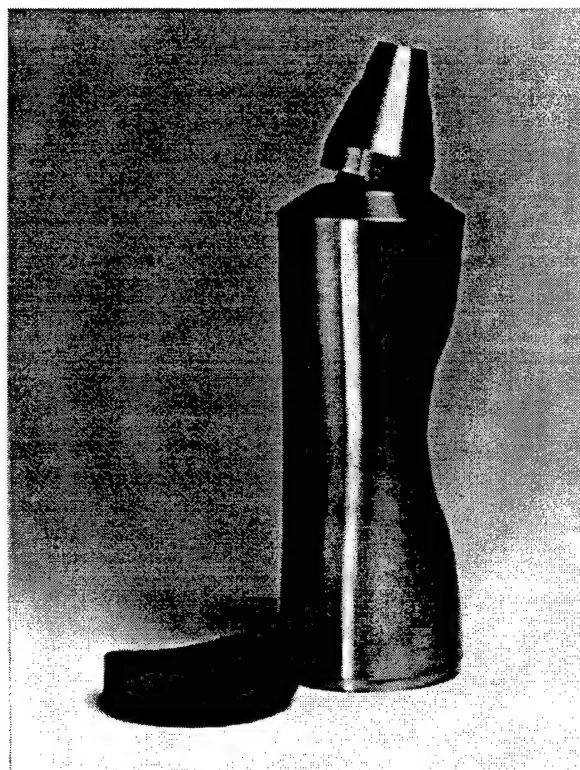
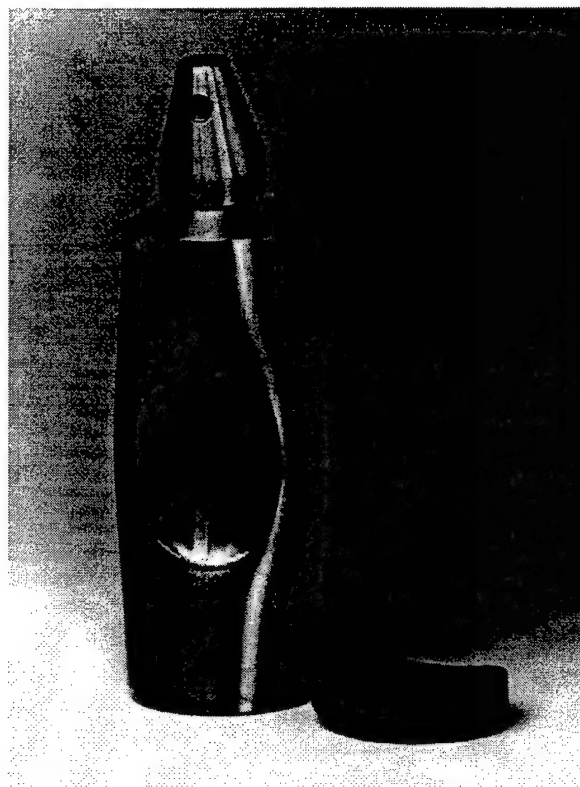
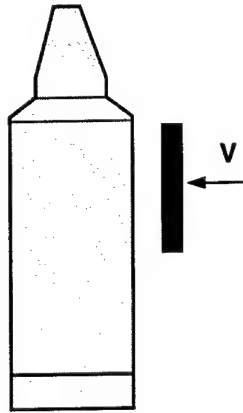


Figure 2-12. Damage to Chemical Submunition 1 from side-on impact at midheight.

Impact Test 17

Impactor Velocity (V) = 197 m/s

Impactor Mass = 942 g



Impact Orientation

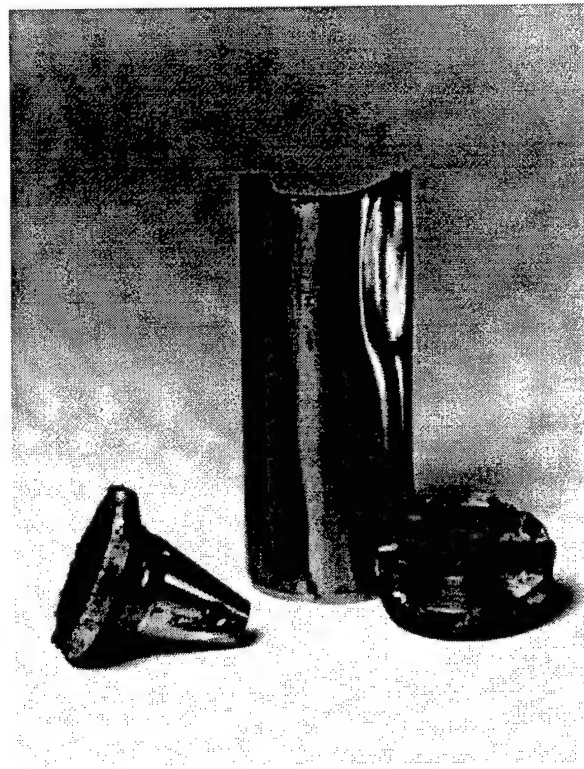
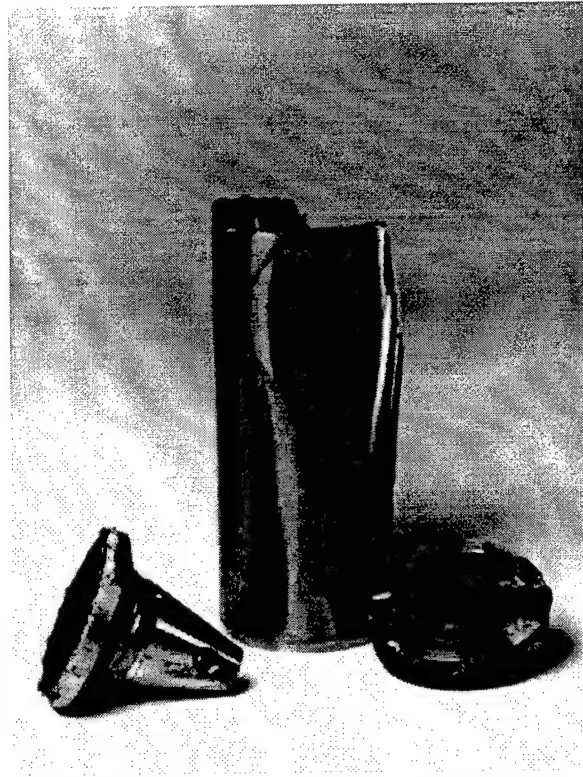
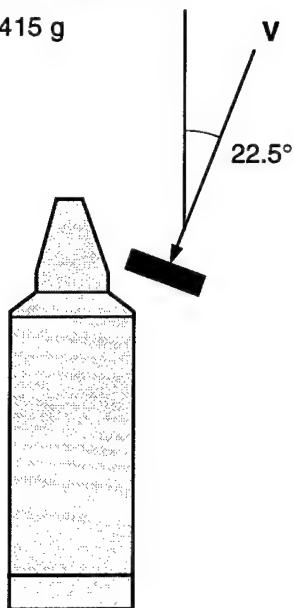


Figure 2-13. Damage to Chemical Submunition 1 from side-on impact near top.

Impact Test 21

Impactor Velocity (V) = 343 m/s

Impactor Mass = 415 g



Impact Orientation

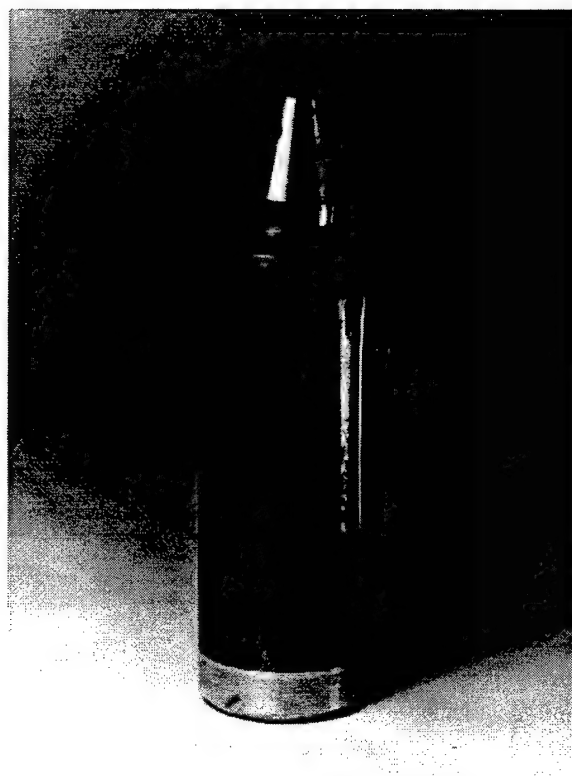
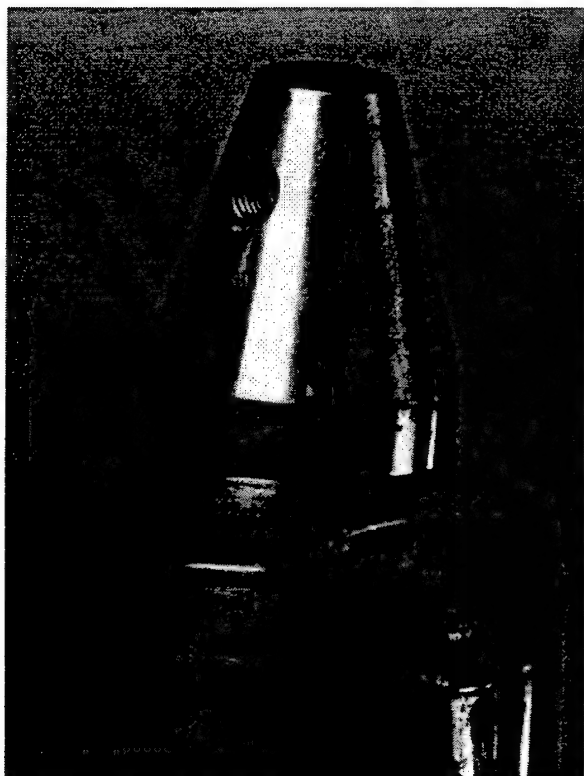
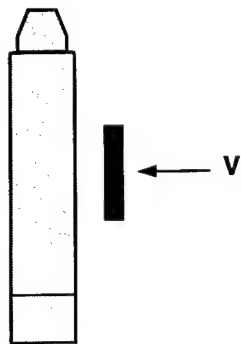


Figure 2-14. Damage to Chemical Submunition 1 from oblique shoulder impact.

Impact Test 27

Impactor Velocity (V) = 200 m/s

Impactor Mass = 594 g



Impact Orientation

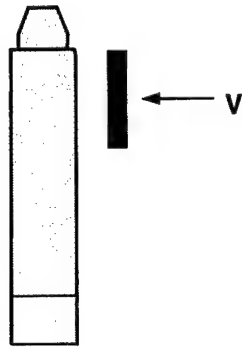


Figure 2-15. Damage to welded Chemical Submunition 2 from side-on impact at midheight.

Impact Test 25

Impactor Velocity (V) = 200 m/s

Impactor Mass = 598 g



Impact Orientation

Fracture

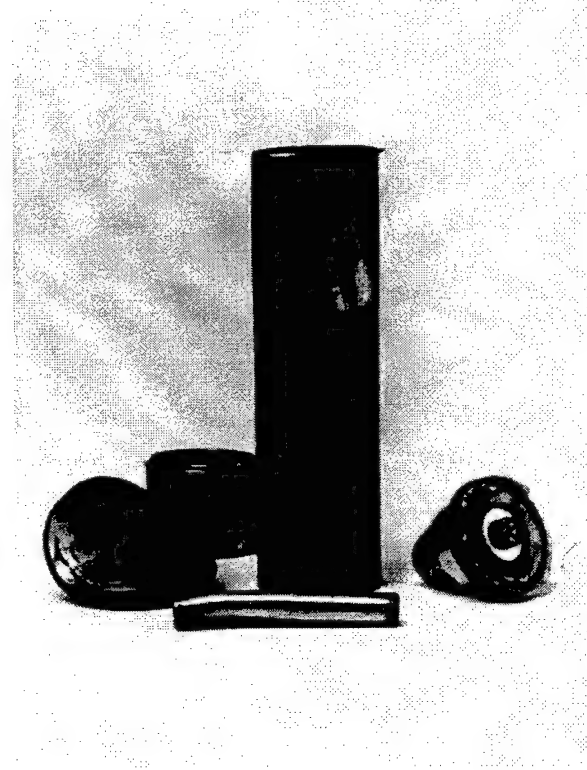
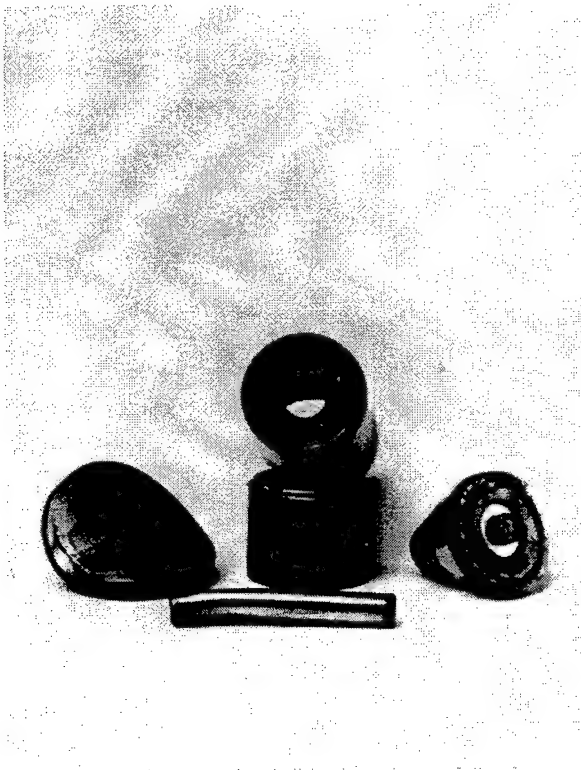
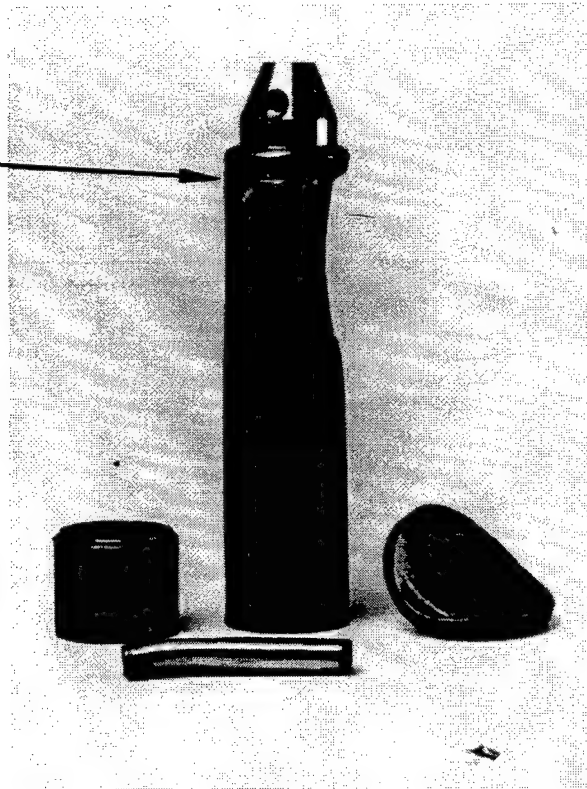
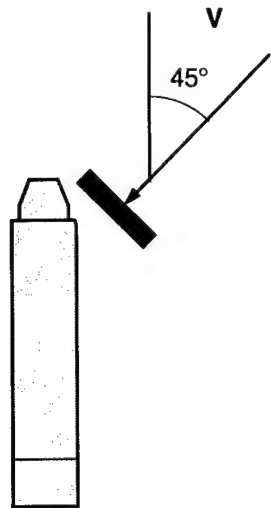


Figure 2-16. Damage to welded Chemical Submunition 2 from side-on impact near top.

Impact Test 26
Impactor Velocity (V) = 205 m/s
Impactor Mass = 599 g



Impact Orientation

Fracture →

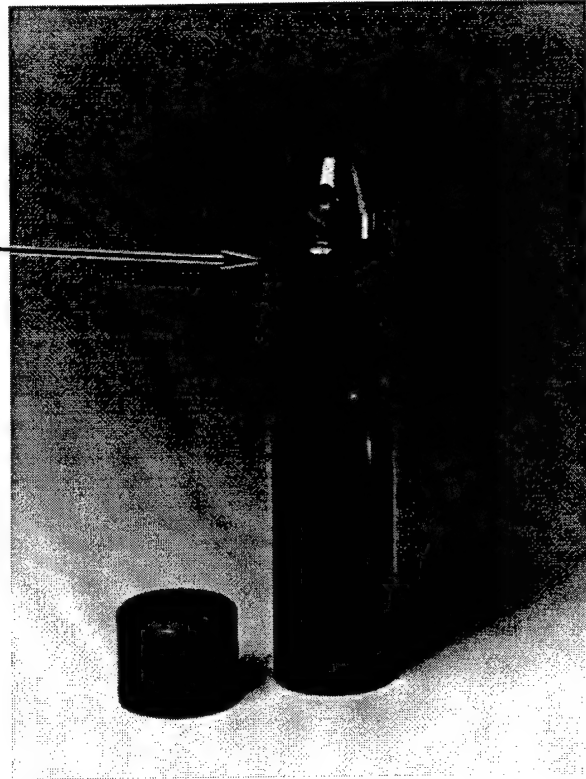


Figure 2-17. Damage to Chemical Submunition 2 from oblique shoulder impact.

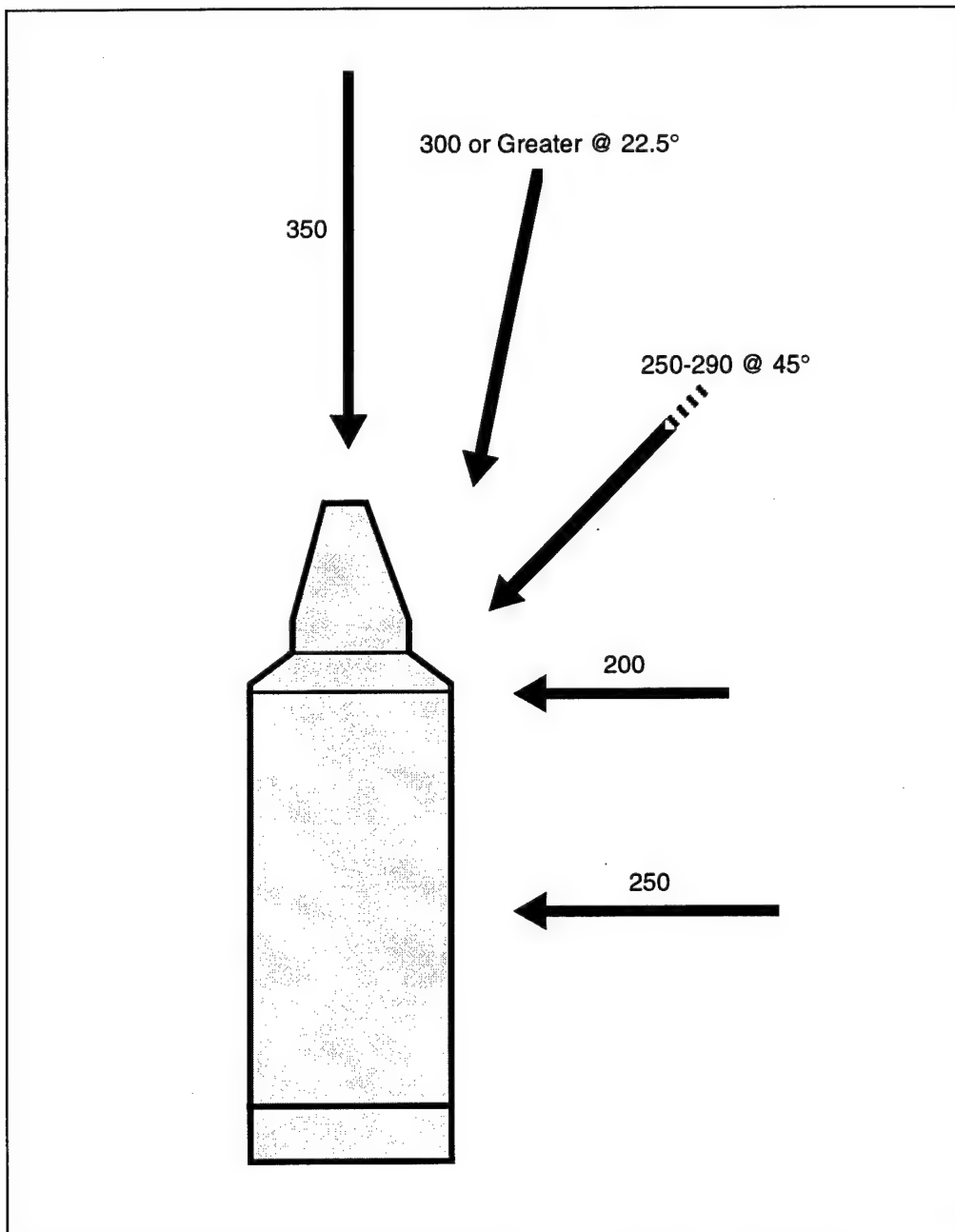


Figure 2-18. Impact velocities to produce failure in Chemical Submunition 1 for different types of impacts (1.9-cm-thick, 8.9-cm-diameter impactors).

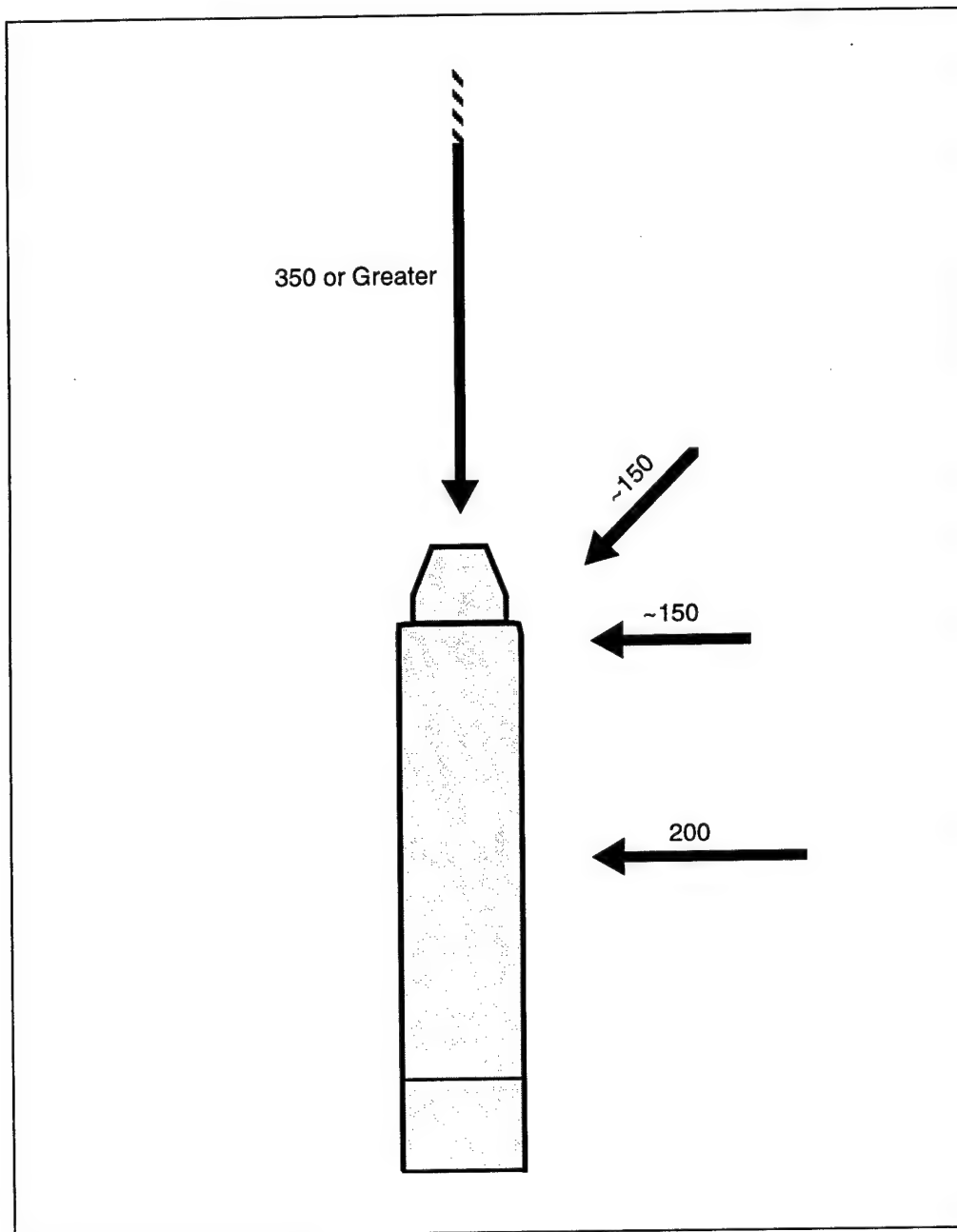


Figure 2-19. Impact velocities to produce failure in Chemical Submunition 2 for different types of impacts (1.2-cm-thick, 8.9-cm-diameter impactors).

additional parameter. (All the other calculations described in this report had the baseline 5% ullage volume.)

Table 2-3. Plate impact calculations on Chemical Submunition 2.

Calculation Number	Plate Velocity (m/s)	Plate Size (LxWxT cm)	Kinetic Energy (kJ)	Diaphragm Pressure (MPa)	Diaphragm Strain (%)	Impact Position	Ullage Volume (%)
F1 (7a)	200	8.89 x 6.98 x 1.2	11.7	90	19	Middle	5
F2 (7b)	200	8.89 x 6.98 x 1.2	11.7	100	22	Middle	0
F3 (7c)	200	8.89 x 6.98 x 1.2	11.7	110	25	Top	0
F4 (7d)	200	8.89 x 6.98 x 1.2	11.7	85	18	Bottom	0
F5 (7e)	200	20.7 x 6.98 x 1.2	27.2	100	23	Full Length	0
F6 (7q)	566	20.7 x 3.49 x 0.3	27.2	75	18	Full Length	0
F7 (7f)	200	4.44 x 6.98 x 1.2	5.9	55	12	Middle	0
F8 (7g)	283	4.44 x 6.98 x 1.2	11.7	95	26	Middle	0
F9 (7h)	200	8.89 x 3.49 x 1.2	5.9	65	13	Middle	0
F10 (7i)	283	8.89 x 3.49 x 1.2	11.7	105	28	Middle	0
F11 (7j)	283	8.89 x 3.49 x 0.6	5.9	55	11	Middle	0
F12 (7k)	400	8.89 x 3.49 x 0.6	11.7	85	18	Middle	0
F13 (7l)	800	8.89 x 3.49 x 0.3	23.6	110	35	Middle	0
F14 (7m)	566	8.89 x 3.49 x 0.3	11.7	75	15	Middle	0
F15 (7n)	200	4.44 x 6.98 x 2.4	11.7	110	35	Middle	0
F16 (7o)	141	4.44 x 6.98 x 2.4	5.9	70	13	Middle	0
F17 (7p)	141	4.44 x 3.49 x 4.8	5.9	70	13	Middle	0

The calculations F2, F3, and F4 show the effect of impact position with the baseline fragment impact. The impact location produces approximately a 15% variation in calculated burst diaphragm peak strain and a 10% to 15% variation in peak pressure at the diaphragm. In the calculated response for the top side impact, the fuze failed; this did not occur for the middle or bottom side impacts.

2.4.5 Effects of Ullage.

In our side impact experiments, we initially found a correlation between the total volume reduction and the failure of the burst diaphragm. Specifically, when the total volume reduction was greater than the ullage (5%), the diaphragm always burst. When the total volume reduction was less than the ullage (5%),

the diaphragm rarely burst. We hypothesized that the diaphragm burst was caused simply by squeezing the ullage out of the submunition until the hydrostatic pressure could build up sufficiently to burst the diaphragm. To check this hypothesis, we conducted an experiment on a full-scale Chemical Submunition 2 that had 15% ullage. This experiment (G-45) was performed at a plate impact velocity of 200 m/s, with the plate striking the side of the submunition midway along its length. We used the same size plate and impact velocity as that used in an earlier experiment (G-27) in which the rupture diaphragm was burst and the submunition had a volume change of 7.2%. In experiment G-45, the rupture diaphragm was also burst and the volume change was 5.3%. This result suggests that the mere squeezing of the submunition to a volume change greater than the ullage volume is not the driving mechanism that leads to diaphragm rupture. We hypothesize that it is the dynamic pressure that leads to diaphragm rupture. DYNA3D calculations were performed to check this hypothesis.

The DYNA3D calculations shown in Figure 2-20 indicate that the transient pressure pulse acting on the diaphragm is a result of the dynamic stress waves in the internal fluid (water). As the submunition is impacted, a compressive pressure pulse is transmitted through the canister wall into the fluid. This pressure pulse spreads through the interior of the submunition, reflecting off the interior surfaces, producing a complex transient pressure history. For an impact occurring at midheight on the submunition, it takes approximately 50 μ s for the pressure pulse to travel to the burst diaphragm at the bottom of the submunition and to the ullage region at the top of the submunition. Any relief of the pressure pulse occurring at the ullage requires about 120 μ s to reach the burst diaphragm. For many of the submunition loading conditions considered, the internal loading on the diaphragm was sufficient to cause failure of the burst diaphragm before the arrival of the relief wave from the ullage at the top of the submunition. The burst diaphragm would therefore have failed before the ullage volume was removed and before uniform compression of the fluid would have occurred.

To determine the effect of ullage location, we performed two experiments on a half-scale Chemical Submunition 2. (Use of half-scale models is discussed in Section 4.) In Test G-48, the half-scale submunition was oriented nose up so that the ullage was on the opposite end of the submunition from the rupture diaphragm. The 0.6-cm-thick, 4.45-cm-diameter plate struck the side of the model midway along its length at a velocity of 200 m/s. In this test, the fuze was removed and the rupture diaphragm was burst. In Test G-62, a half-scale Chemical Submunition 2 was oriented nose down so that the ullage was next to the rupture diaphragm. The test was identical to Test G-48 in every other respect. In Test G-62, we found that the diaphragm burst just as it had in Test G-48. We conclude that the location of the ullage is not significant in producing damage to the rupture diaphragm.

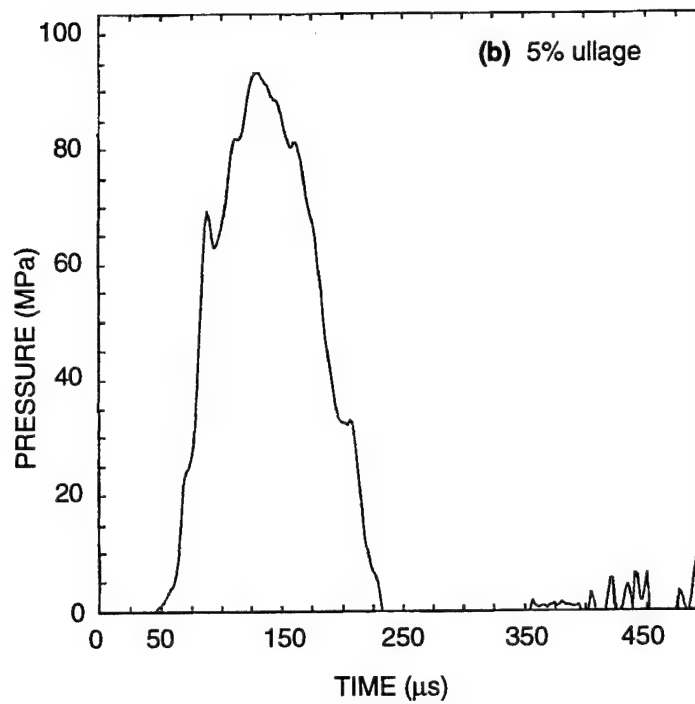
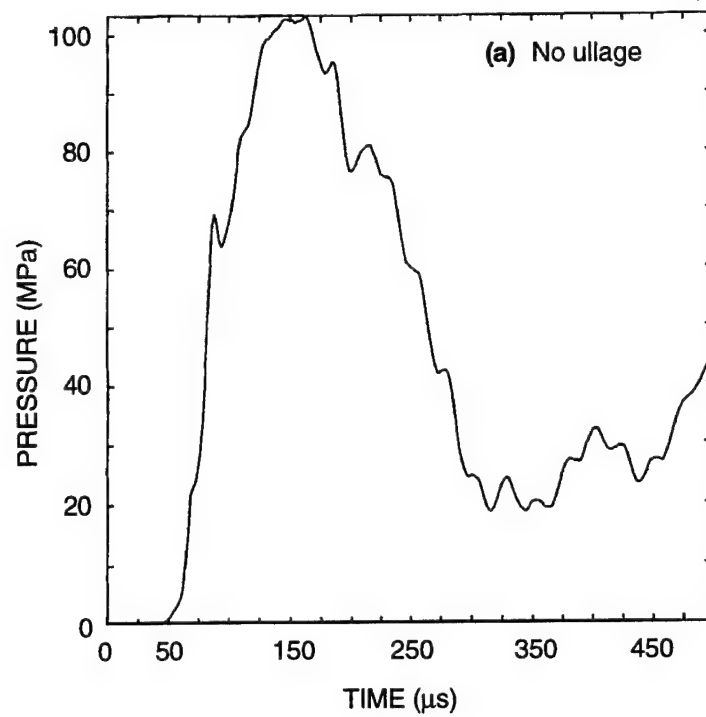


Figure 2-20. Pressure-time histories at the rupture diaphragm produced by disk impact at the midheight of Chemical Submunition 2 (200 m/s).

2.5 SUBMUNITION RESPONSE TO SIDE AREA LOADING.

From the sled tests, it is apparent that many submunitions are damaged by loading over the entire side of the submunition. We performed experiments and calculations to investigate the response of submunitions to side area loading. We designed the experiments and performed the calculations so that the results could be cast in the form of the classic pressure-impulse (PI) curves (Abrahamson and Lindberg, 1971), as discussed in Section 3.

2.5.1 Experiments.

For impulsive short-duration loading, the rupture diaphragm burst, and the fuze plug was removed at an impulse of 64 ktaps on the half-scale model (corresponds to 128 ktaps on a full-scale model), as shown in Figure 2-21. At an impulse of 47 ktaps (94 ktaps full-scale), the diaphragm and fuze were intact.

In submunition-to-submunition impact tests (intermediate duration loading), neither the fuzes nor the diaphragm of the impacted target is ruptured at an impact velocity of 111 m/s. The imparted velocity is 50 m/s. At an impact velocity of 158 m/s, the fuze is removed from the impacted target but the diaphragm is intact. The imparted velocity is 77 m/s. Figure 2-22 shows views of the two submunitions in the test at an impact velocity of 230 m/s. In both, the fuze is removed and the diaphragm is ruptured. Volume change in the two submunitions averages 7%. This is consistent with side impact tests using circular plate impactors, in which diaphragm rupture does not occur at impact velocities less than 200 m/s.

In the first static (long-duration) test, the submunition was crushed uniformly between two flat platens until the diaphragm was ruptured at a load of 178 to 100 kN (40,000 to 45,000 lb). At this load, the submunition was unloaded and the contact area measured. A static load of 200 kN (45,000 lb) corresponds to a pressure over the loaded area of about 130 MPa (19,000 psi). This test was repeated with custom platens that only load the submunition along its length between the hard end points. The platen had rounded ends. Here, the load to cause failure is lower because the stiff end closures do not carry any of the crush load. At the peak load of about 80 kN (18,000 lb), leakage was produced around the fuze plug (see Figure 2-5). This load corresponds to a pressure over the loaded area of 92 MPa (13,500 psi).

2.5.2 Calculations.

We performed a series of calculations to investigate the side loading response of Chemical Submunition 2 in more detail. In these calculations, the load distribution was chosen to approximate the



Diaphragm End

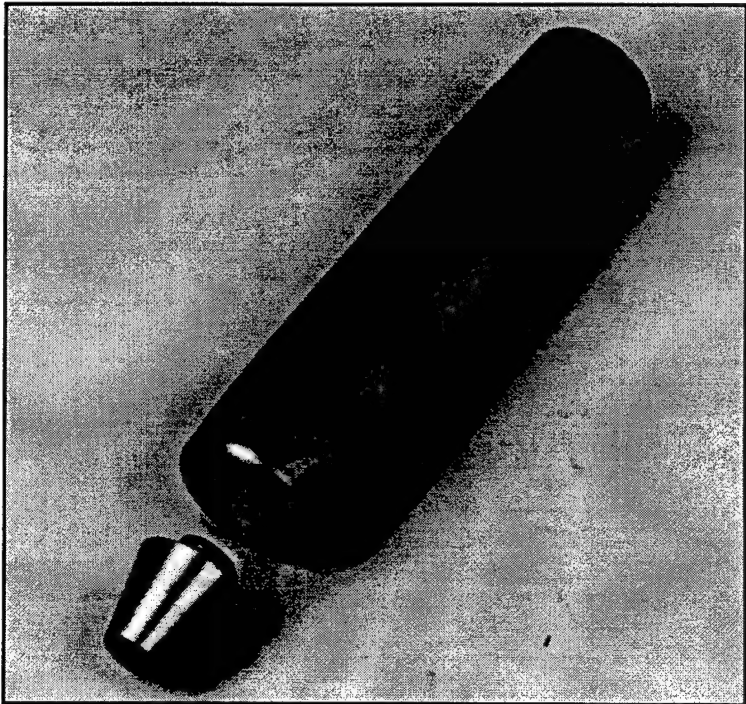
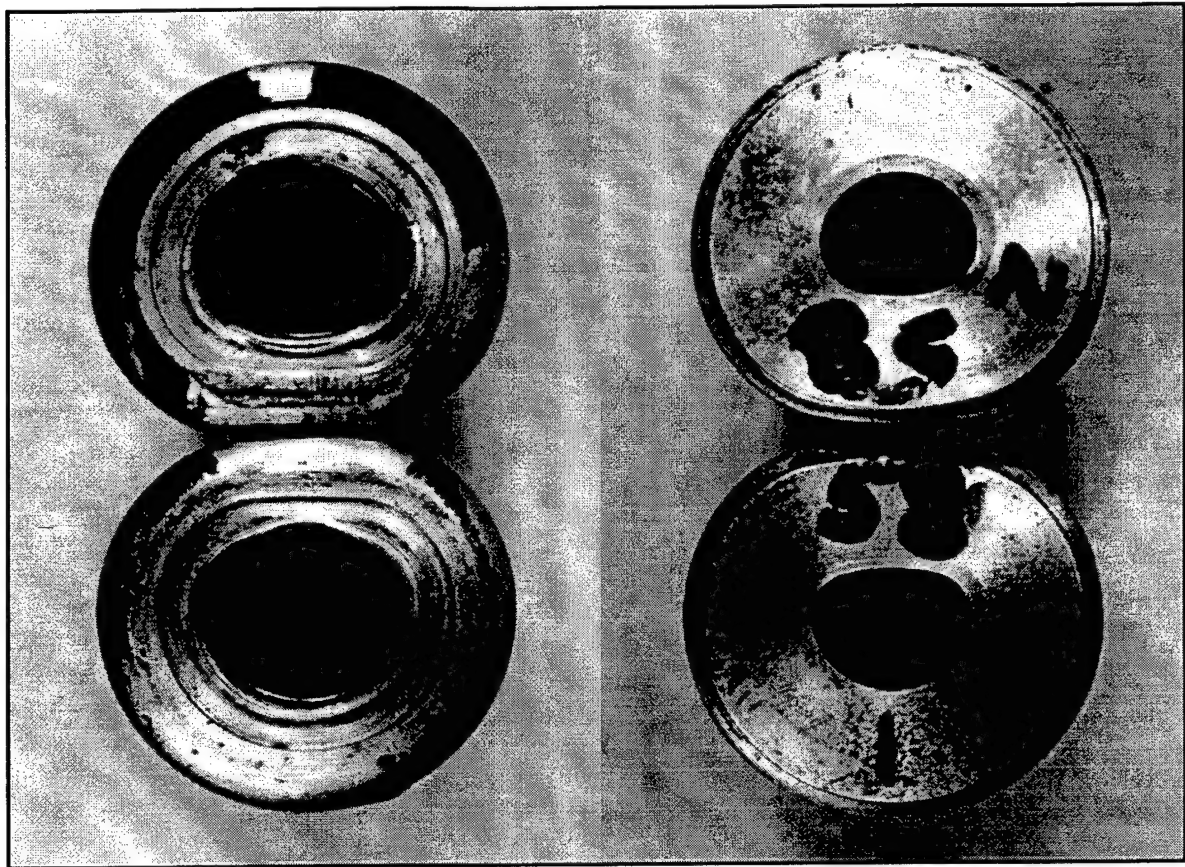


Figure 2-21. Damage to submunition from impulsive loading
(equivalent full-scale load: impulse = 128 ktaps;
pressure = 1.2 GPa).



Fuze End

Diaphragm End

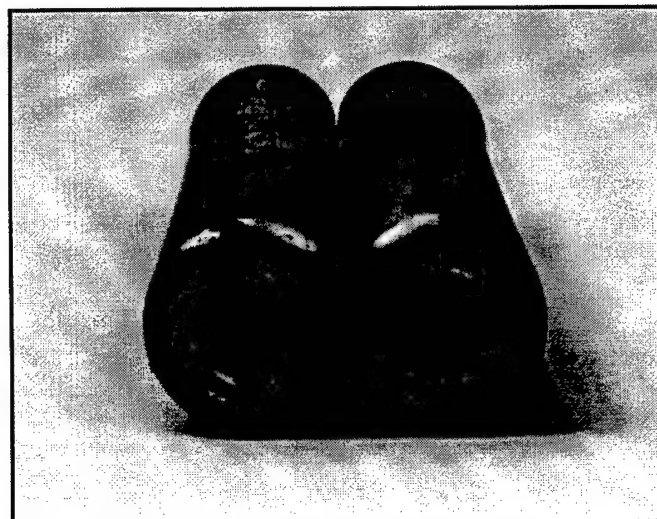


Figure 2-22. Damage to submunitions from body-to-body impact
(equivalent full-scale load: impulse = 269 ktaps;
pressure = 125 MPa).

loading produced in the experiments. Therefore, the pressure (and impulse intensity) distribution was uniform over the central portion and tapered at the edges, i.e.,

$$p = \begin{cases} P_o & \theta < \theta_f \\ P_o \exp(-\theta/\theta_d)^2 & \theta > \theta_f \end{cases} \quad (2.1)$$

where θ_f is the center flat top angle set to $\pm 17.1^\circ$ and θ_d is the decay angle set to $\pm 27.5^\circ$. A typical calculation of this type is shown in Figure 2-23. This calculation showed diaphragm burst and partial removal of the fuze. Table 2-4 provides a summary of the submunition calculations with side pressure loads applied. Critical diaphragm strain was taken to be in the range of 13% to 17%.

Table 2-4. Pressure side area loading calculations on Chemical Submunition 2.

Calculation Number	Peak impulse (ktaps)	Load Duration (μs)	Peak Pressure (MPa)	Diaphragm Pressure (MPa)	Diaphragm Strain (%)	Notes
Can9k	80	10	800	45	11	
Can9i	100	10	100	65	17	
Can9h	120	10	120	75	22	
Can3b	100	30	333	20	4.5	• Slight side denting
Can3c	130	30	433	40	10	
Can3d	170	30	567	70	20	• Dent and fuze rotation
Can3e	220	30	733	100	36	• Fuze failure
Can9f	150	100	150	40	5	
Can9d	200	100	200	80	15	
Can9e	250	100	250	130	30	
Can9a	300	300	100	36	7	
Can9c	375	300	125	80	15	
Can9b	450	300	150	130	3	
Can9g	810	900	090	40	7	
Can9j	990	900	110	55	15	Fuze Failure

2.6 RESIDUAL VELOCITIES.

We conducted another series of experiments on half-scale models of Chemical Submunition 2 to determine the maximum residual velocity that a submunition could sustain following an impact and still be

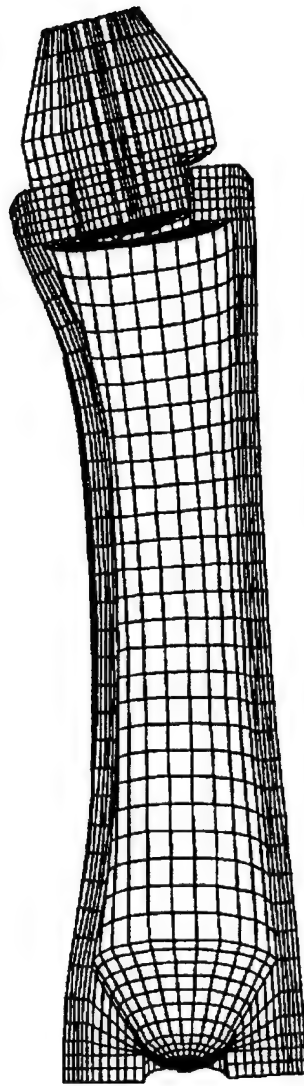


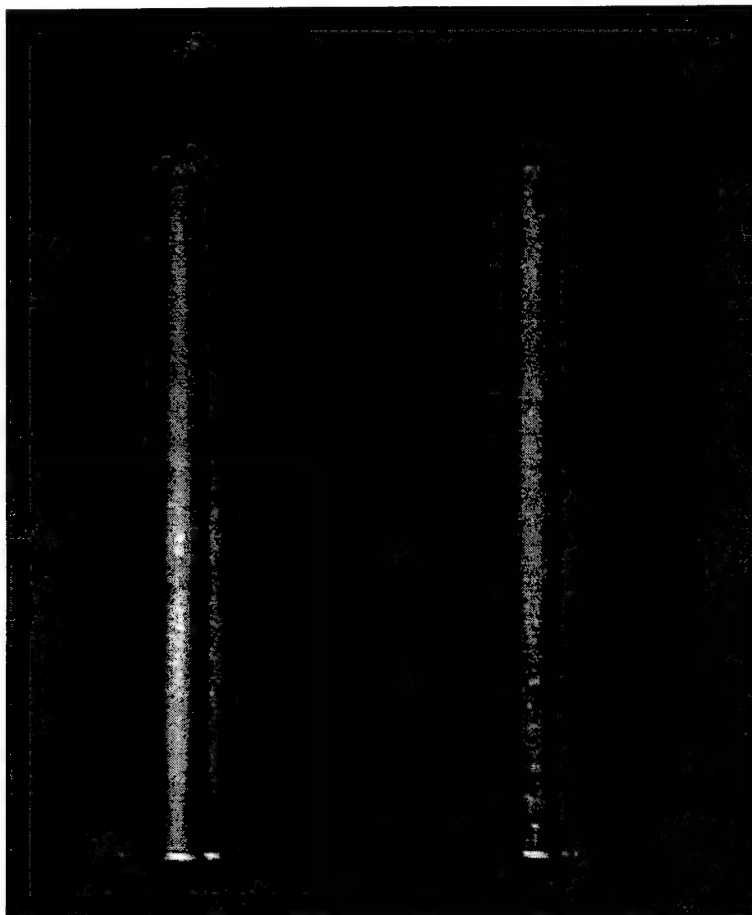
Figure 2-23. DYN3D calculation of pressure loading on the side of Chemical Submunition 2.

in a condition to function (fuze and diaphragm intact and no leakage). This information can be used for post-engagement analysis.

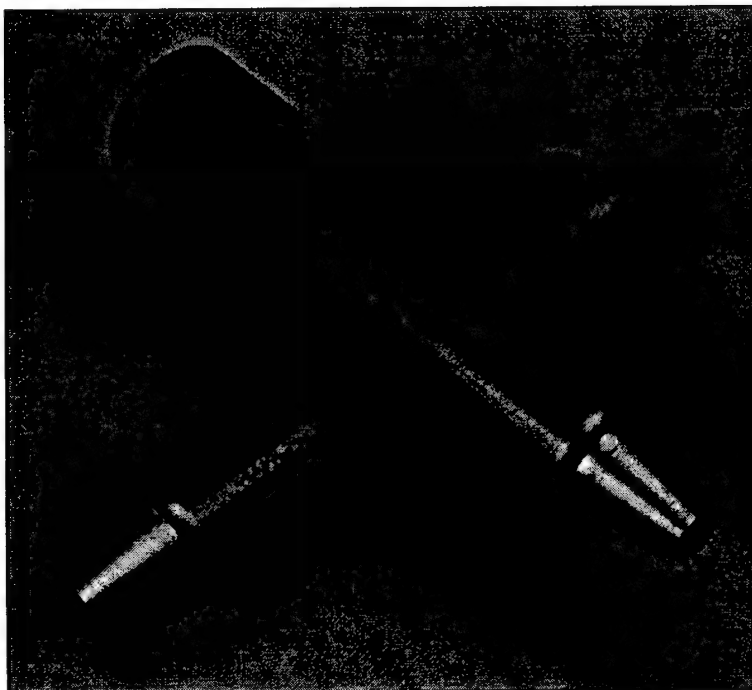
Figure 2-24 shows the impact orientations. In Test G-54, an undamaged half-scale submunition filled to 95% of capacity was impacted at 111 m/s by an empty submunition that had been lightly damaged in a previous test. High-speed motion pictures of the test were taken and analyzed. From the movies, we found that the residual velocity of the target submunition was 49.1 m/s. The residual velocity of the impactor was 34.9 m/s. For this test, the impacted submunition was intact and no fluid was lost from it. After considering the initial mass and final mass of each submunition, we found that total momentum of both submunitions was conserved to within 1%. In a second test (G-55), the target submunition was impacted at a velocity of 158 m/s. The impact removed the fuze plug from the target and about half of the fluid inside was removed, as shown in Figure 2-22. Residual velocity of the target submunition was 76.6 m/s. The impactor had a residual velocity of 55.7 m/s. Again, after considering the initial mass and final mass of each submunition, we found that the total momentum of both submunitions was conserved to within 1%. Thus, for submunitions that are aligned as in these tests, the maximum residual velocity for a surviving submunition is in the range of 50 to 75 m/s.

We also performed tests in which the axis of the impacting submunition was rotated 90 degrees to the axis of the impacted submunition. At an impact velocity of 127 m/s, both submunitions deformed around the impact area but neither leaked, as shown in Figure 2-25. The velocity imparted to the impacted submunition was 71 m/s. An impact velocity of 153 m/s caused the diaphragms to burst in both submunitions. The imparted velocity was 85 m/s.

We conclude that Chemical Submunition 2 can have imparted velocities of about 65 m/s without leaking for a range of impact orientations.



On Axis



Cross Axis

Figure 2-24. Body-to-body impact orientations.

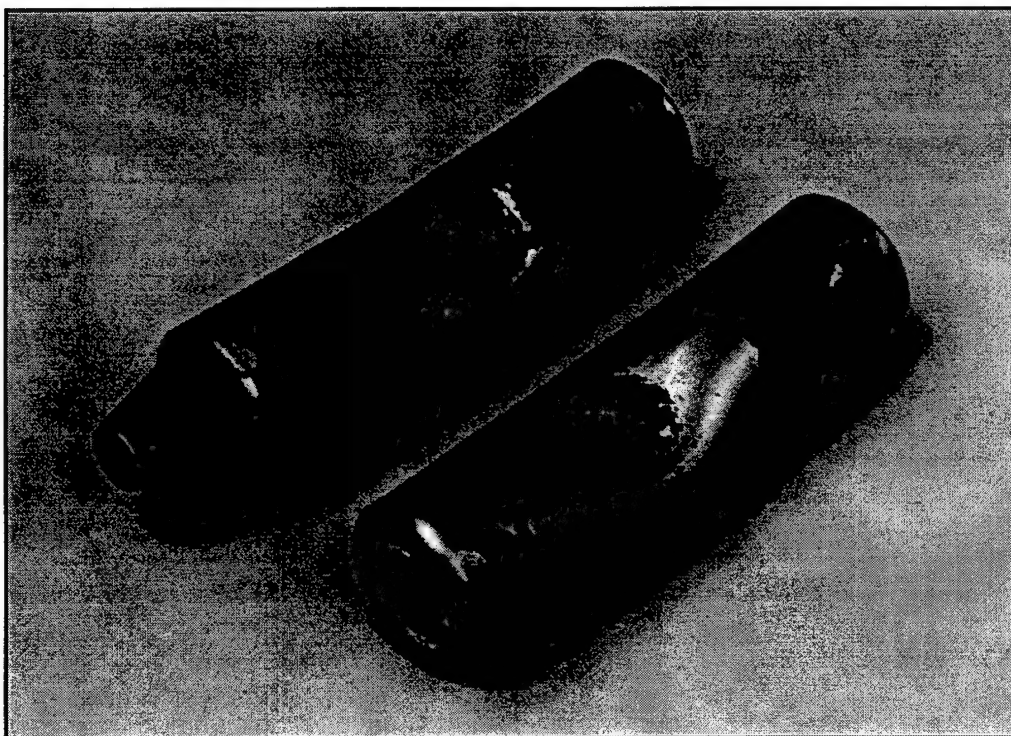
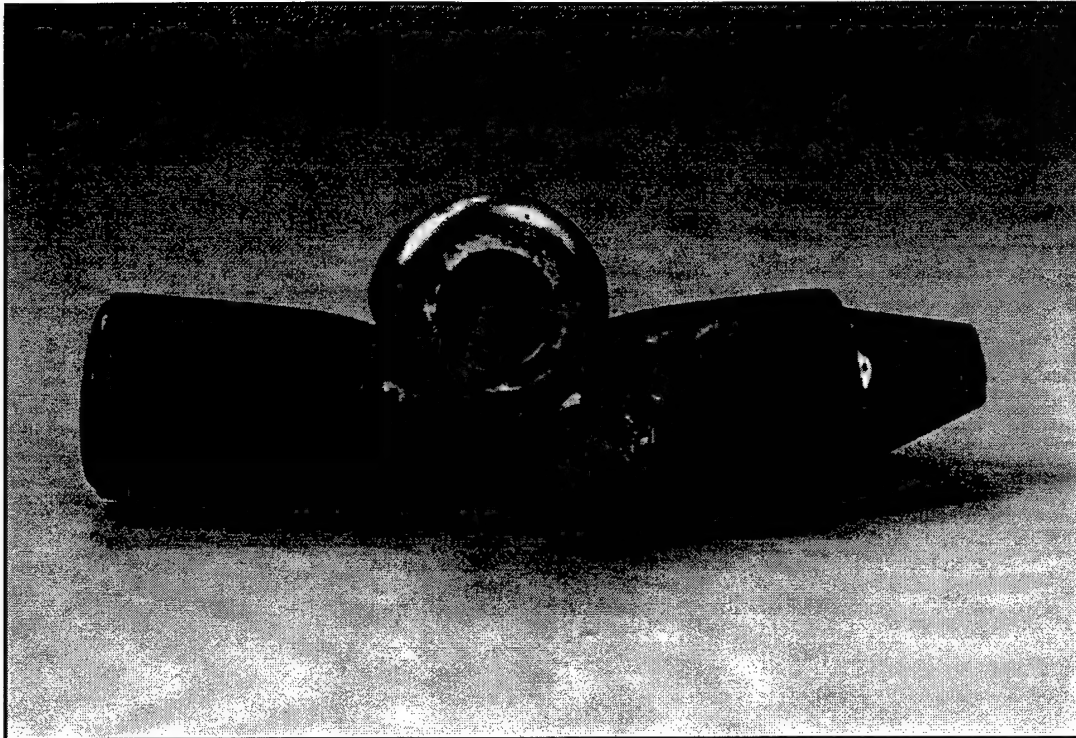


Figure 2-25. Damage to submunitions from cross-axis body-to-body impact.

SECTION 3

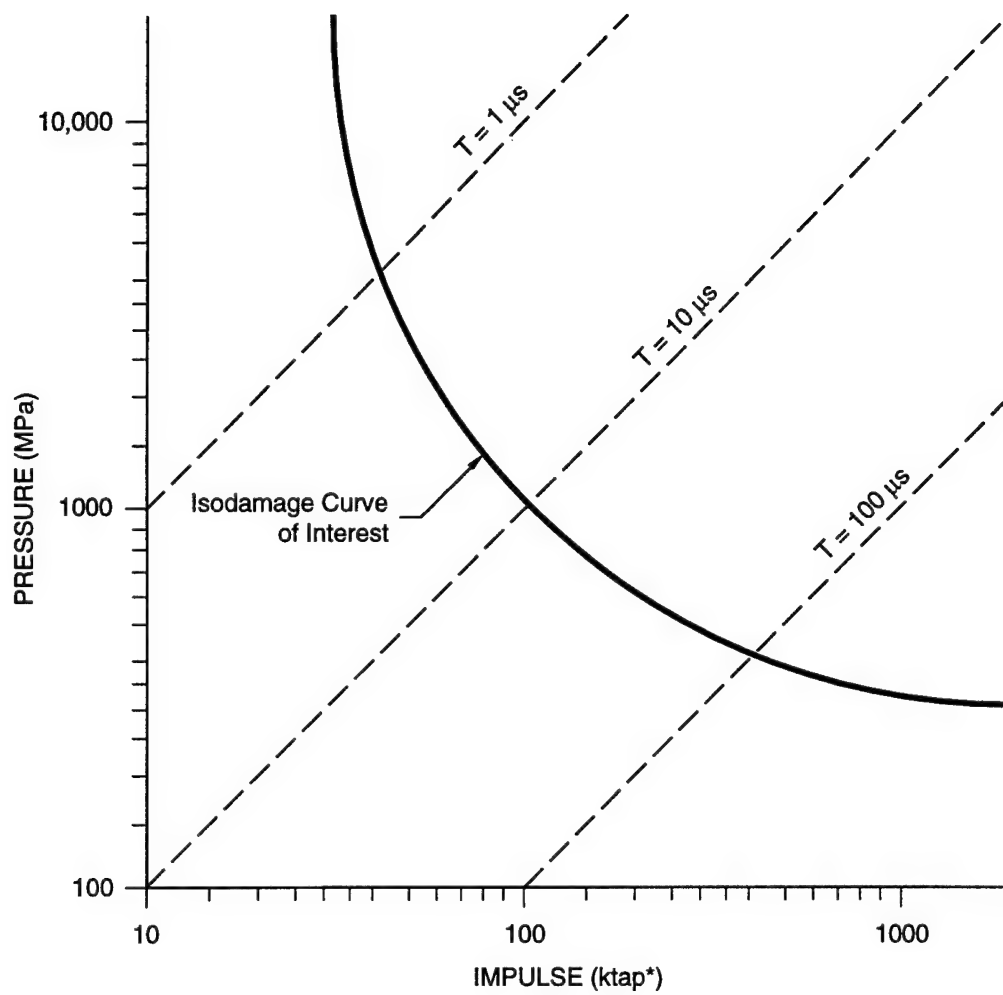
PRESSURE-IMPULSE CURVES FOR CHEMICAL SUBMUNITIONS

3.1 BACKGROUND.

A useful technique for presenting the load-damage relationship for any structure responding to a simple pulse load is to characterize the applied load by its peak pressure P and total impulse I . It has been demonstrated for a wide variety of structures that there are an infinite number of combinations of P and I that produce the same final damage (Abrahamson and Lindberg, 1971). For a particular damage level, these combinations of P and I are represented as an isodamage curve in pressure-impulse coordinates. Figure 3-1 illustrates that a typical isodamage curve would appear as a square hyperbola in PI space. For simple pulse shapes (e.g., exponential or square wave), the straight lines shown in this PI diagram have slopes equal to the characteristic load duration.

The combinations of peak pressure and impulse needed to produce a given damage level are represented by the isodamage curve. For example, for an exponential pressure load with a characteristic load duration of $10\ \mu\text{s}$, a peak pressure of $1000\ \text{MPa}$ produces the damage level specified by the isodamage curve shown in Figure 3-1. This same damage can also be produced by different combinations of peak pressures and characteristic load durations such as $1\ \mu\text{s}$ and $4200\ \text{MPa}$ or $100\ \mu\text{s}$ and $420\ \text{MPa}$. If the point representing the applied load falls above and to the right of the isodamage curve, the resulting damage would be greater than that specified by the isodamage curve. Conversely, points below and to the left of the curve indicate that the resulting damage would be less than that specified by the isodamage curve.

In what follows, we first investigate the applicability of PI curves to the complex pulse shapes typically produced in impacts. Then, we develop the PI curve for Chemical Submunition 2 under side area loading. We use this curve as a baseline to compare other PI points for a different loaded area, a different load orientation, and a different submunition. Finally, we develop a PI curve from simplified analyses based on mechanisms that produce burst diaphragm failure and fuze removal.



*1 tap = 1 dyne • s/cm²

Figure 3-1. PI diagram for a responding structure such as a submunition
(pressure = $P e^{-1/T}$, impulse = PT).

3.2 PRESSURE-IMPULSE CHARACTERIZATION FOR CHEMICAL SUBMUNITION 2.

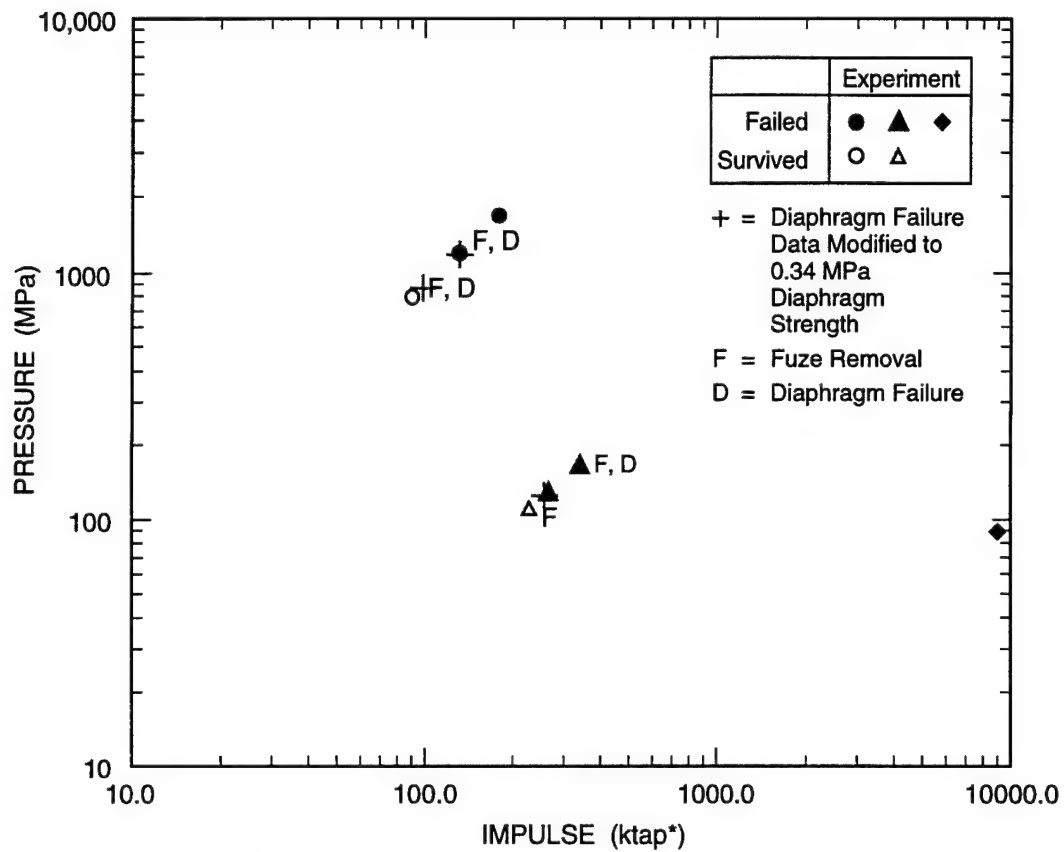
3.2.1 External Loads.

Figure 3-2 shows the data from the experiments for side loading of Chemical Submunition 2 at all three load durations. All submunitions tested did not have the same diaphragm strength. In particular, the diaphragm strength for the half-scale models was 91 MPa compared with the full-scale diaphragm strength of 34 MPa. Therefore, we first normalized those critical load data associated with diaphragm failure to a standard diaphragm strength of 34 MPa as follows.

Calculations of the side impact of Chemical Submunition 2 were performed for a range of impulses. Figure 3-3 shows the pressure histories at the diaphragm at three impulse levels for 300 μ s duration loads. Figure 3-3(d) shows the calculated peak pressure versus the loading impulse. The pressure versus impulse relationship is highly nonlinear. This curve was used to normalize the impulse to a diaphragm strength of 34 MPa. For example, the half-scale models tested had a strength of 91 MPa which, according to Figure 3-3(d), would require an external impulse of 385 ktaps to produce failure. If the same model had a diaphragm strength of 34 MPa, it would require an impulse of 295 ktaps. Thus, if the failure mechanism is diaphragm failure, the critical impulses for the 91 MPa diaphragms were reduced to $300/380 = 76\%$ of their measured value (for the same load duration) so that they could be compared with the 34-MPa strength diaphragms found in full-scale submunitions.

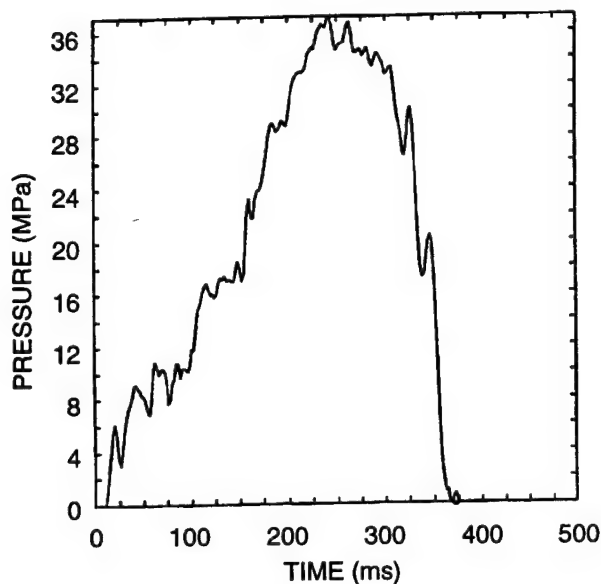
The impulse associated with the data points corresponding to diaphragm failure at a 10 μ s load duration has been reduced to 76% of the applied impulse to account for the greater diaphragm strength in the half-scale model tested and the calculated combinations of pressure and impulse that produce the damage of interest. Figure 3-4 shows the data as well as the calculations from Table 2-4. The curve shown in the figure is a hyperbola that best fits the data and the calculated points.

The damage level represented by the experiments is incipient rupture of the burst diaphragm at the short and intermediate load durations and leakage around the fuze plug at the long duration load. For all the calculations, the failure mode is burst diaphragm rupture of a 34 MPa strength diaphragm. The impulse and duration of the sheet explosive load is well known from previous similar experiments. The impulse from the impact experiment is deduced directly from measurements of imparted velocity; the load duration for the submunition-to-submunition impact is determined from DYNA3D calculations. The pressure from the static crush tests is the maximum total force divided by the maximum contact area. This example illustrates how information from various sources can be used as input to the specification of the PI curve.

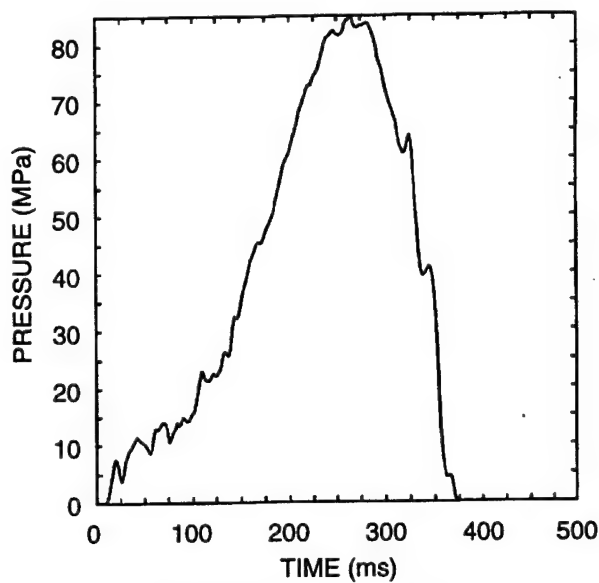


*1 tap = 1 dyne • s/cm²

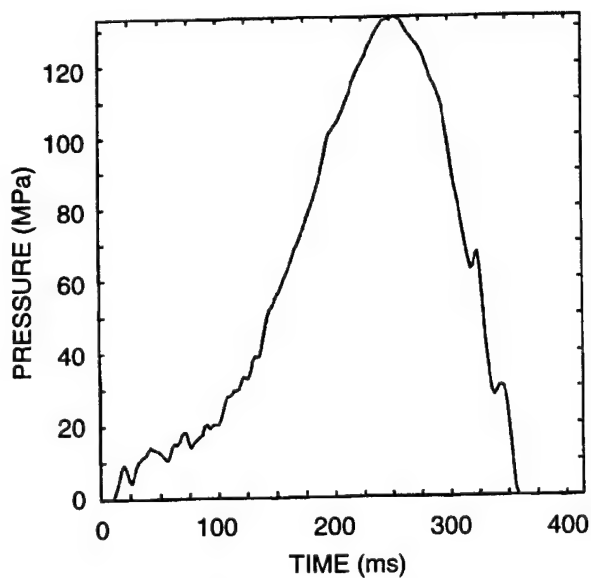
Figure 3-2. Chemical Submunition 2 PI data for various side loading experiments.



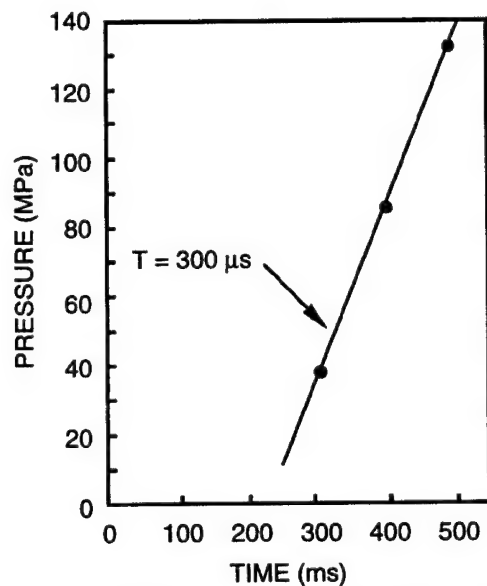
(a) Pressure history for $I = 300 \text{ ktap}^*$



(b) Pressure history for $I = 375 \text{ ktap}^*$



(c) Pressure history for $I = 450 \text{ ktap}^*$

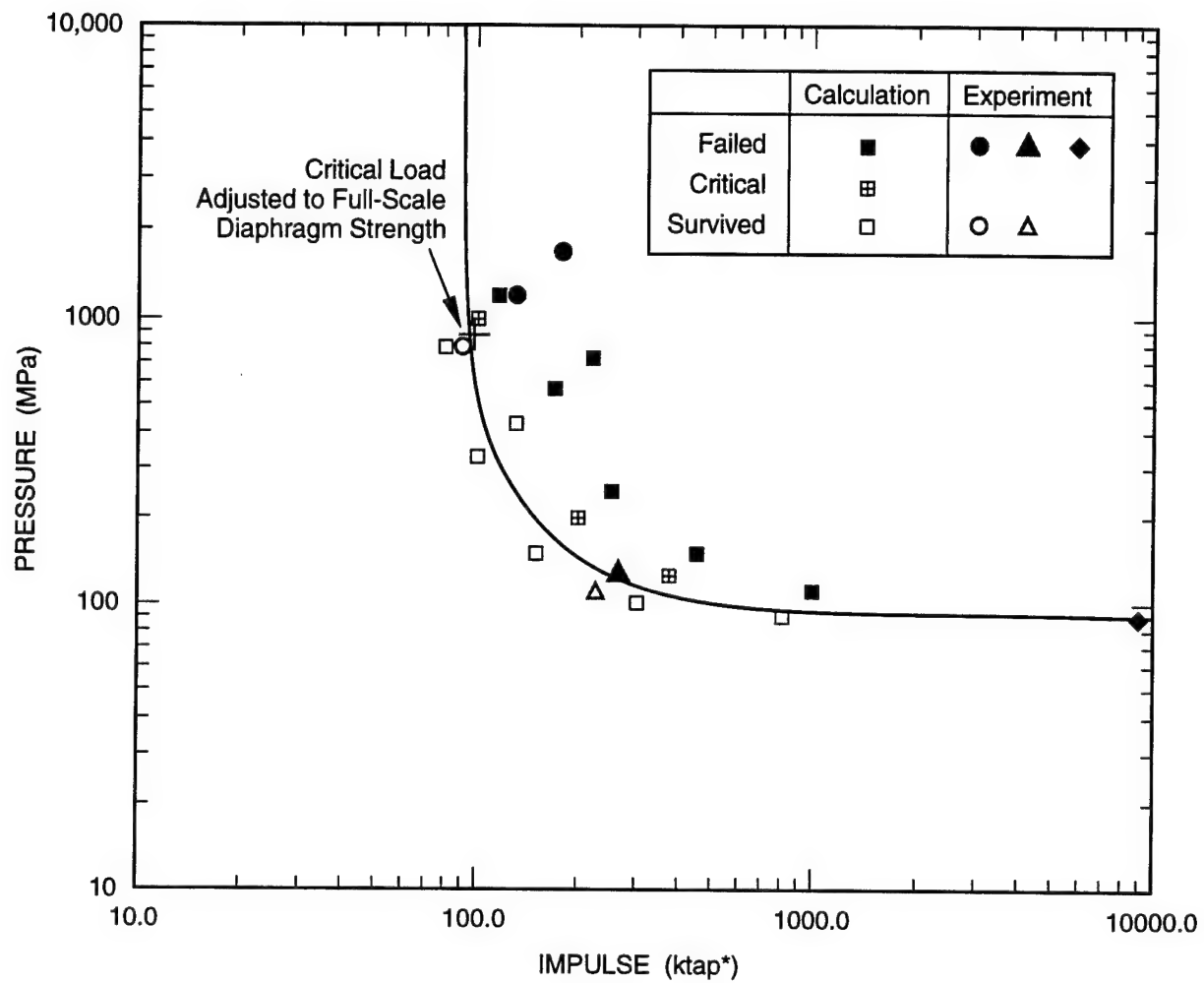


(d) Peak diaphragm pressure versus external impulse

*1 tap = $1 \text{ dyne} \cdot \text{s}/\text{cm}^2$

CAM-4727-105

Figure 3-3. Calculated effect of impulse on internal pressure for side area loading of Chemical Submunition 2 ($\tau = 300 \mu\text{s}$).



*1 tap = 1 dyne • s/cm²

Figure 3-4. PI curve for external side load of Chemical Submunition 2.

3.2.2 Internal Loads.

For each calculation of pressure loading applied to the exterior of Chemical Submunition 2, the response of the internal fluid was also calculated. Our goal was to find the combinations of internal PI pairs that correspond to the external PI pairs that produce failure. Two internal pressure pulses that correspond to external loads that produce failure are shown in Figure 3-5.

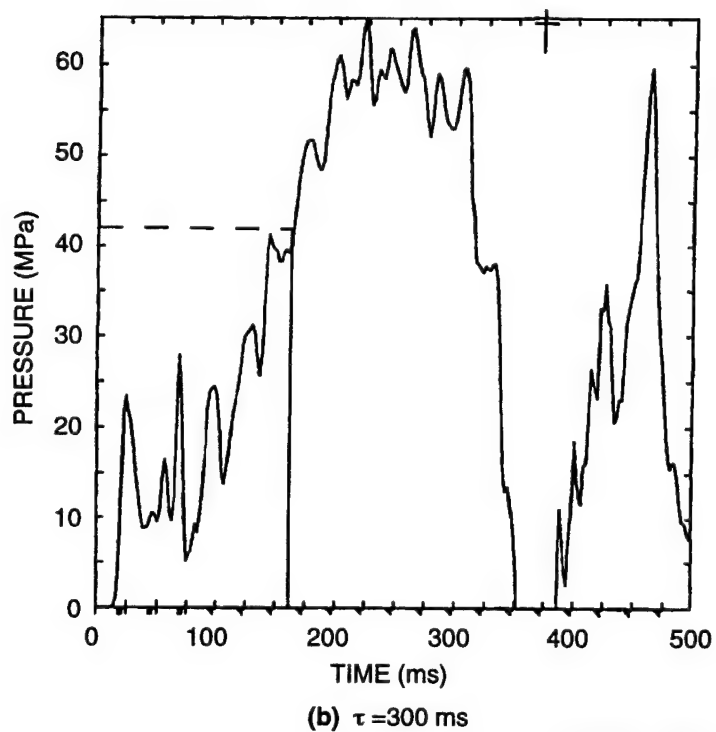
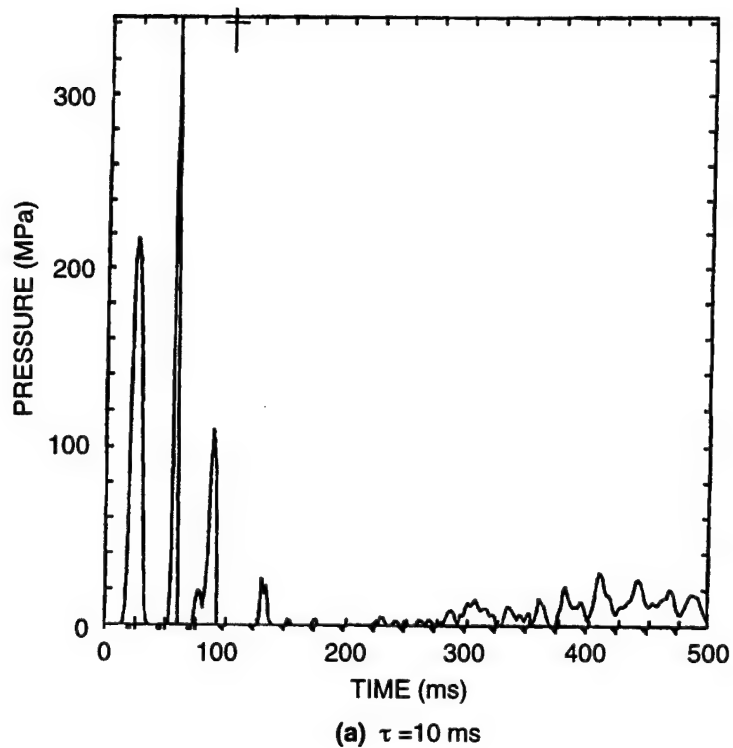
If we simply assign the peak value as the peak pressure and the integral of the pressure time history as the impulse for such pulses, there is no pattern to the internal PI pairs that produce failure. The reason is that the classical PI curves were developed for simple pulse shapes such as exponential, triangular, or square. In many practical applications, such as the impact of a submunition, the actual pulse shapes are complex due to wave reverberations in the impactor and the target, such as shown in Figure 3-6. The PI characterization could be applied to these complex pulse shapes if the complex pulse could be represented as an equivalent simple pulse with peak pressure P and total impulse I related to the complex pulse.

To this end, we analyzed the response of a diaphragm, such as the burst diaphragm in a chemical submunition, to complex pulse shapes. The details of the analysis are presented in Appendix A. The analysis shows that complex pulses can be represented by equivalent square waves if the response time of the diaphragm is taken into account. We use this result below to characterize the complex pressure pulses developed in the submunitions, particularly in the internal fluid, in terms of equivalent square pulses with specified amplitude and duration. The analysis of PI curves for complex pulse shapes (Appendix A) shows how to interpret such pulses.

For the 10 μs loading pulse, the pressure shown in Figure 3-5(a) has three distinct pulses that occur within the time from 15 to 100 μs . Because the rise on the first pulse is abrupt, the time between pulses is less than the response time of the diaphragm (about 80 μs). The total impulse associated with this pulse is found by integrating all three pulses, i.e., from 15 to 90 μs or 41 ktaps. The equivalent peak pressure is then $41 \text{ ktaps}/75 \mu\text{s} = 55 \text{ MPa}$. This load produced incipient failure of the diaphragm.

For the 300 μs duration load, the pressure shown in Figure 3-5(b) is below the yield stress of the diaphragm until 160 μs after the pressure is applied. This portion of the pulse does not contribute to the impulse. The rest of the pulse does, however. Therefore, the impulse is taken as the integral of the pressure from 160 to 350 μs or 96 ktaps. The equivalent peak pressure is $I/\tau = 96 \text{ ktaps}/190 \mu\text{s} = 51 \text{ MPa}$. This load was just short of producing diaphragm failure.

Proceeding in this manner, we found the combinations of internal pressures and impulses that produce the burst diaphragm damage of interest for each load duration and plotted them in Figure 3-7. The curve indicated is the best approximation to the internal pressures that cause the burst diaphragm to fail. This curve can be used to predict burst diaphragm failure from pressure histories measured in the fluid in



CAM-4727-116A

Figure 3-5. Pressure histories calculated inside Chemical Submunition 2 for side area loading.

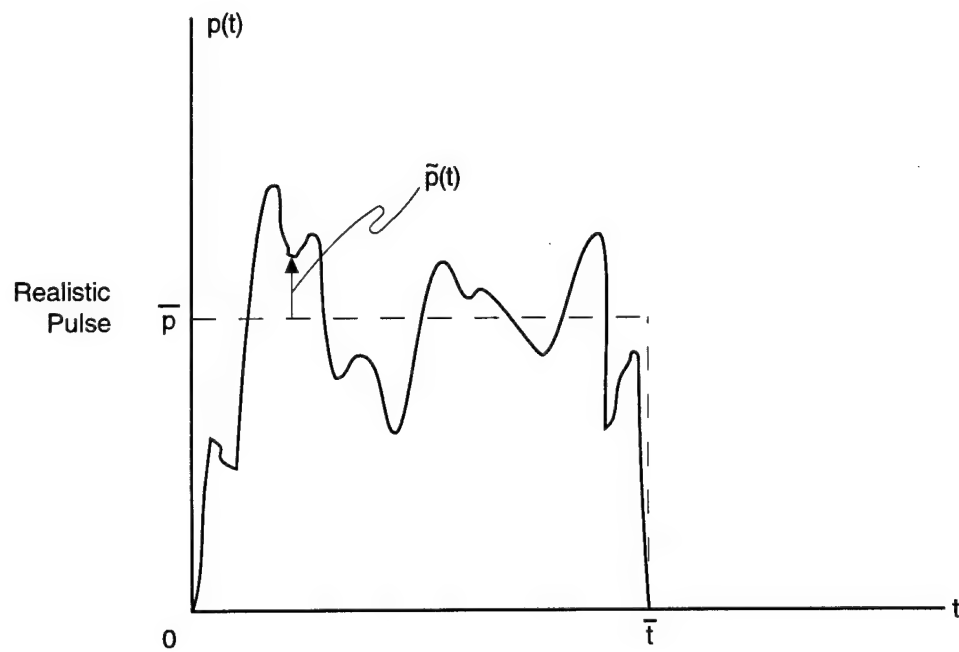
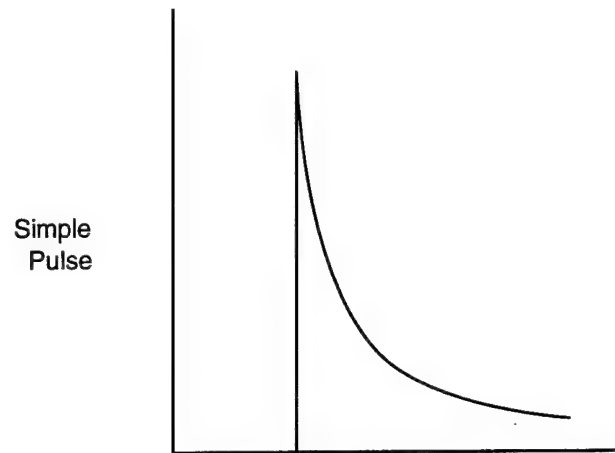
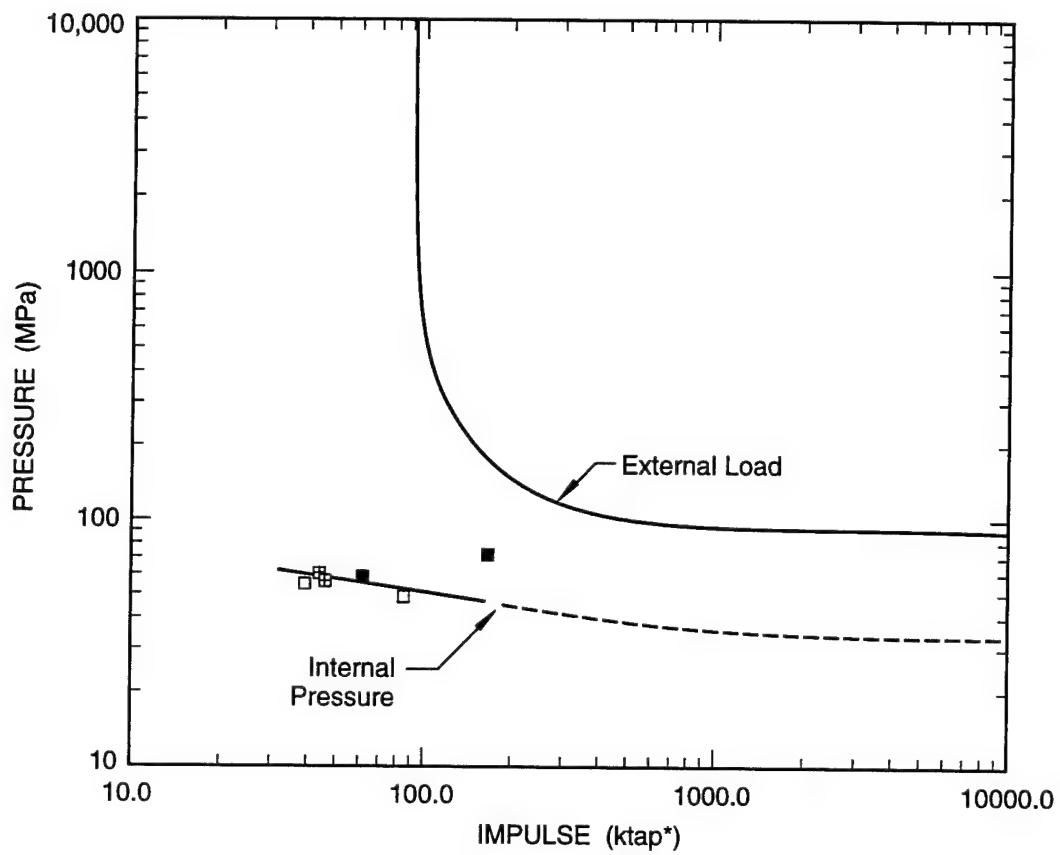


Figure 3-6. Loading pulses for PI characterization.



*1 tap = 1 dyne • s/cm²

Figure 3-7. PI curves for external side load and internal fluid load for Chemical Submunition 2.

submunitions that are subjected to side area loading, in sled tests, or from calculated pressure histories as part of the array response. Although not demonstrated here, it is likely that this curve could also be used to estimate failure for loading other than side area loading. Additional calculations and experiments would have to be performed to make this determination.

The critical load curve for side loading of Chemical Submunition 2 was used as a reference for other critical load information determined experimentally and by calculation. Although complete information is not always available to define the PI curve for other types of loads or other targets, it is useful to compare the PI points that are available to this reference curve as shown below.

Figure 3-8 shows the PI curve for localized loading for two different plate thicknesses on the side of Chemical Submunition 2. Both the impulse and pressure required to produce burst diaphragm rupture are about a factor of 2 greater than for side area loading because the loading area is reduced.

Figure 3-9 shows the PI curve for axial loading of Chemical Submunition 2. The curve shown is drawn so that it is consistent with the calculated points for axial loading over the fuze and shoulder of the submunition. The failure criterion is a critical plastic strain of 15%, which is produced below the shoulder. The single data point is for loading on the end of the fuze. The data point is above the curve because, in the experiment, only the end of the fuze was loaded. In either case, the critical loads for axial loading exceed those for side area loading because the submunition is stronger in this direction and because the loading area is reduced.

3.3 PRESSURE-IMPULSE CHARACTERIZATION FOR CHEMICAL SUBMUNITION 1.

Figure 3-10 shows data for side area loading of Chemical Submunition 1. The impulsive asymptote is about a factor of 3 greater than that for Chemical Submunition 2 because of the greater wall thickness of Chemical Submunition 1.

Figure 3-11 shows PI data for localized plate loading on the side of Chemical Submunition 1. By comparing these data with those of Figure 3-8, we see that the pressure and impulse is about a factor of 2 greater for Chemical Submunition 1 than for Chemical Submunition 2 because of the greater wall thickness of Chemical Submunition 1.

Figure 3-12 shows PI curves for axial loading on Chemical Submunition 1. Two types of calculations were performed with the L2D code. One curve shows a typical calculation for impact loading on the fuze only, such as would occur by a large single fragment. The failure criterion of 15% effective plastic strain was produced below the shoulder of the submunition. These calculations agree with the data shown. Calculations were also performed for loading over the entire end of the submunition in the absence of the fuze. This configuration more closely resembles an array of fragments impacting the end of

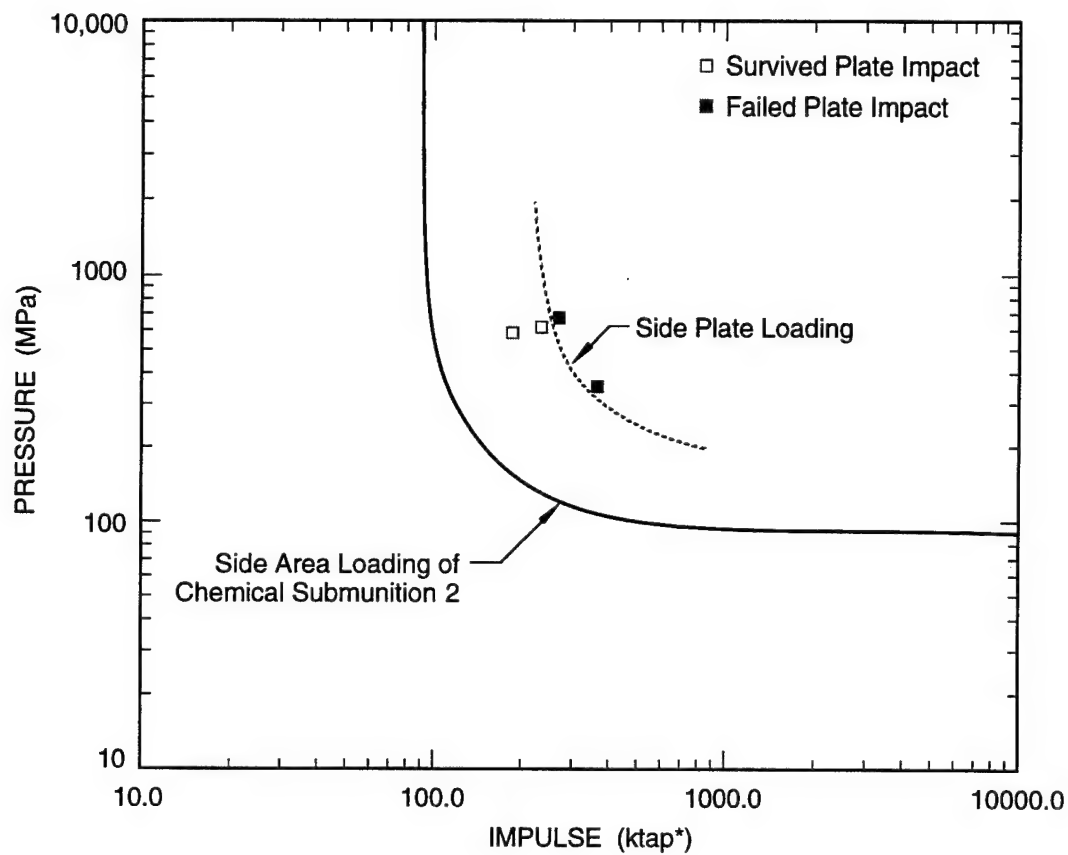
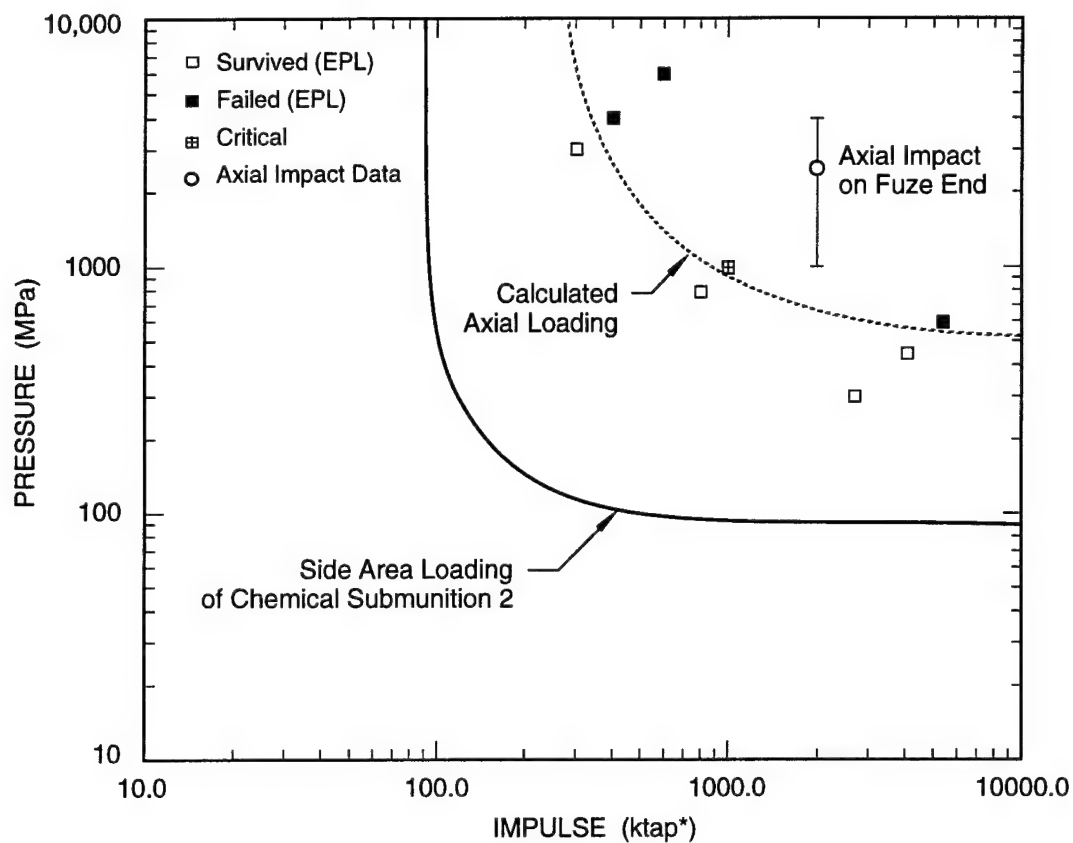
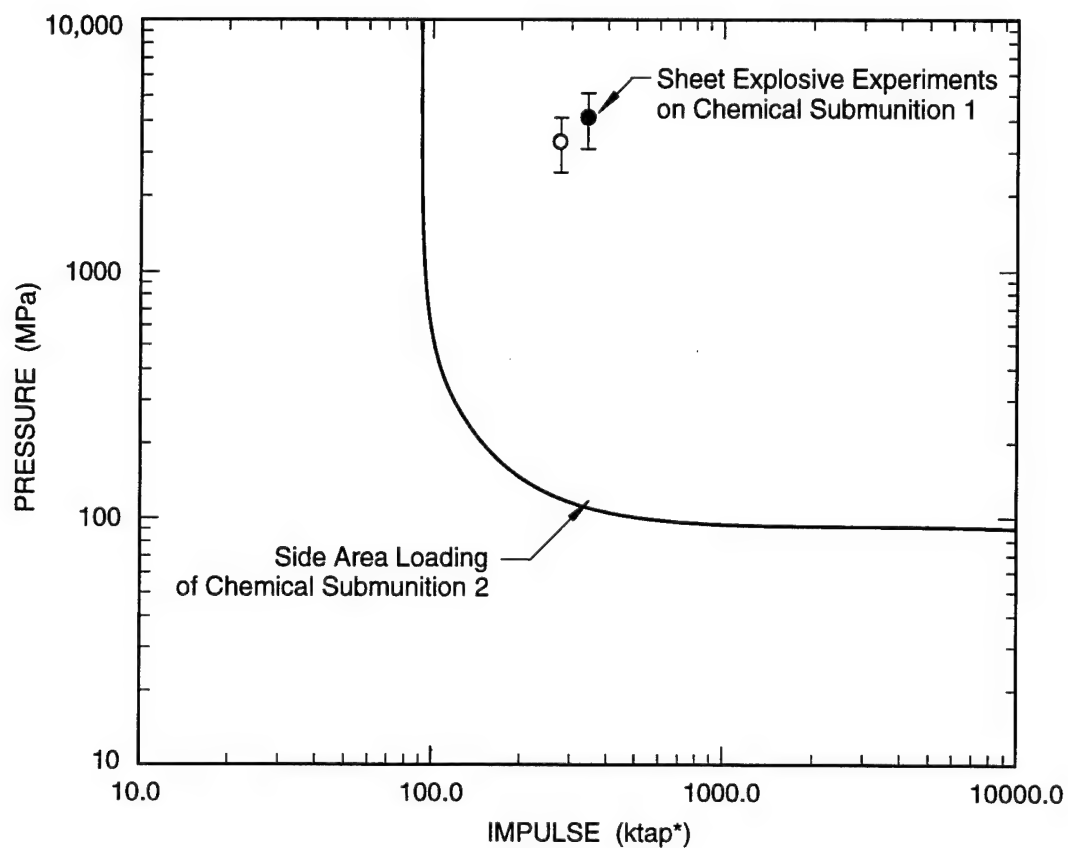


Figure 3-8. PI curve for side impact plate loading experiments on Chemical Submunition 2.



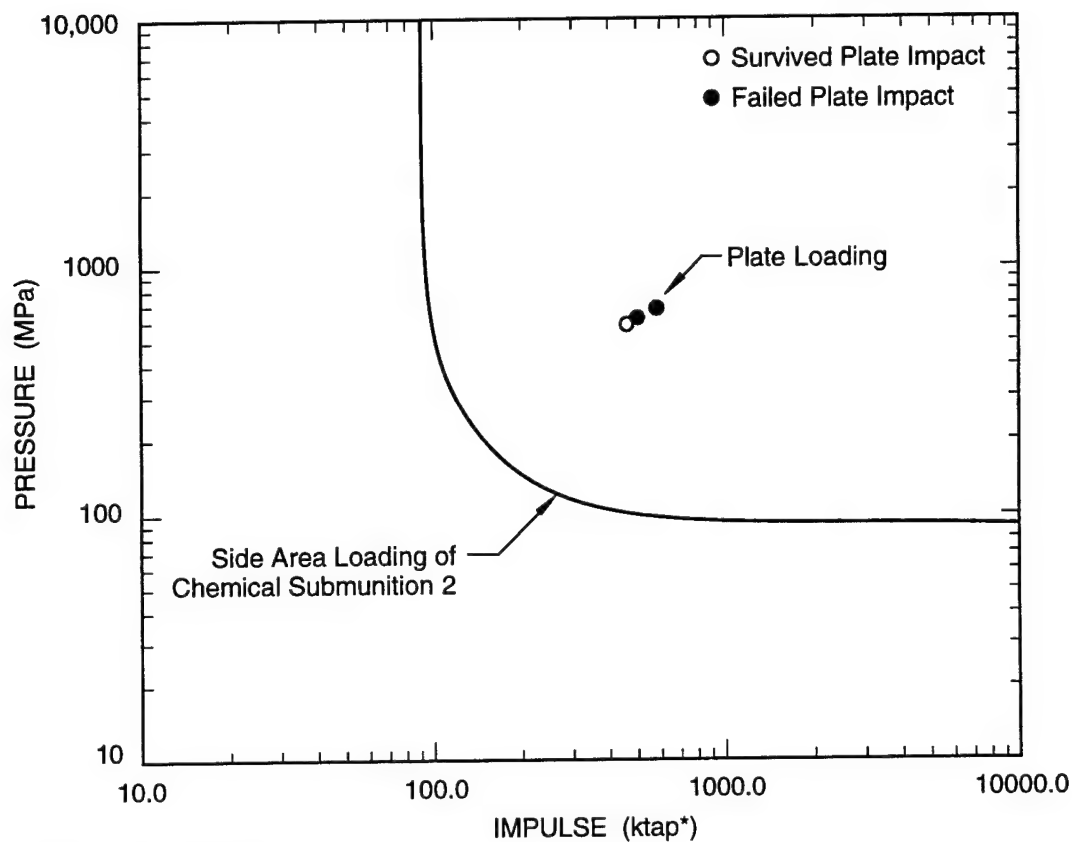
*1 tap = 1 dyne • s/cm²

Figure 3-9. PI curve for axial loading on Chemical Submunition 2.



*1 tap = 1 dyne • s/cm²

Figure 3-10. PI data for side area loading of Chemical Submunition 1.



*1 tap = 1 dyne • s/cm²

Figure 3-11. PI data for side impact plate loading experiments on Chemical Submunition 1.

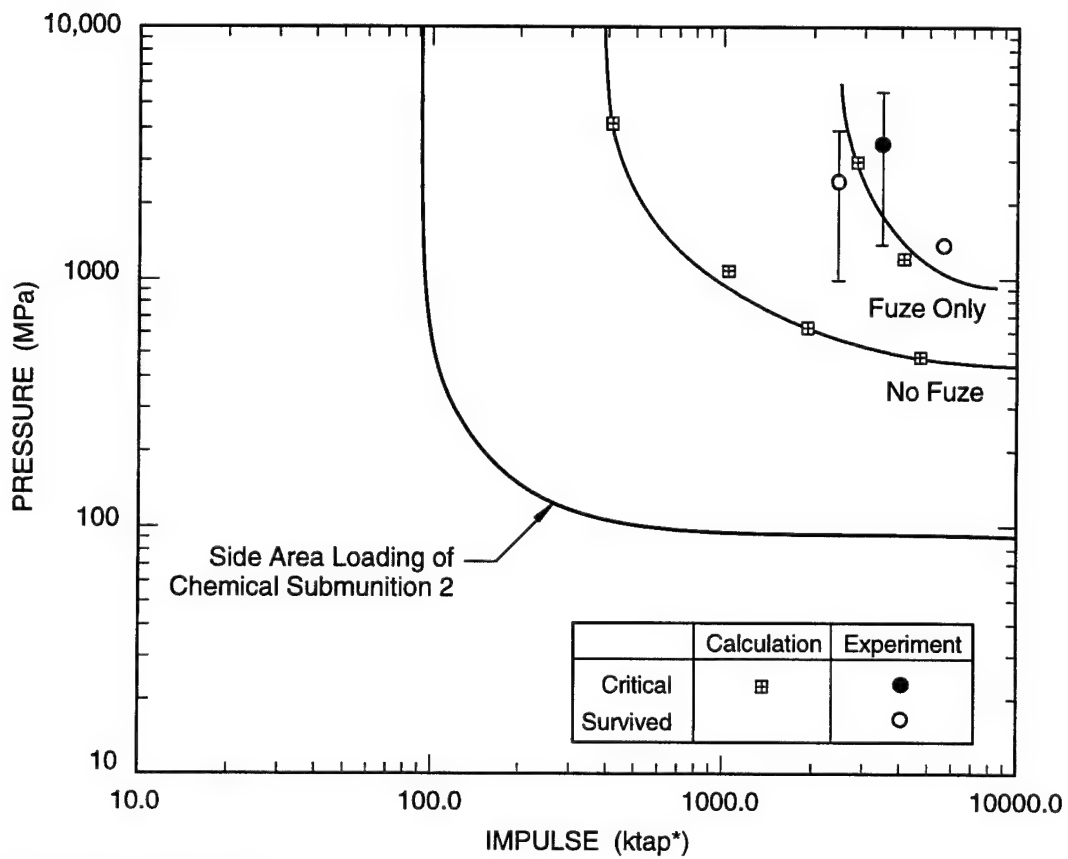


Figure 3-12. PI curves for axial loading on Chemical Submunition 1.

the submunition. The damage mode was similar to that for loading on the fuze only. The differences in area result in greater critical loads for the fuze only loading.

The critical damage information presented above is for specific targets under specific loading conditions. For lethality assessment, it is necessary to predict the response for a variety of targets under a range of loads. This requires simplified methods for determining the critical loads for a range of targets and loading conditions. In the remainder of this section, we present two simplified analyses, one for burst diaphragm failure and one for fuze plug removal.

3.4 PRESSURE-IMPULSE CHARACTERIZATION FOR A LONG FLUID-FILLED CYLINDRICAL SHELL.

We performed this analysis to determine the conditions under which an impact to the side of a fluid-filled cylindrical shell representing a submunition will raise the fluid pressure to a level sufficient to fail the burst diaphragm. The main theoretical approach to solving this problem is to analyze the impact event with a finite element code using a reasonably idealized fragment (e.g., plate- or rectangular-shaped plate) as discussed in Section 2.4. A useful supplement to the finite-element analysis is a classical analysis in which the contact pressure history is further idealized to be a rectangular pulse. The classical analysis is especially useful for lethality assessment if a formula can be derived for the pressure and impulse of the rectangular pulse required to generate the diaphragm burst pressure in the fluid. To relate the pressure and impulse to an idealized fragment, we first approximate the duration of the rectangular pulse as the time taken to flatten the side of the cylinder over a specified sector by the maximum inward deformation divided by half the impact velocity. Then, we assume plastic impact to approximate the fragment momentum change and hence the applied impulse. The average contact pressure is the impulse divided by the duration, if we assume that the contact area is constant and equal to the final value.

In Appendix B, we present the details of a classical analysis addressing a long fluid-filled cylindrical shell subjected to a rectangular pressure pulse applied over a longitudinal strip of its outer surface. The resulting state is one of plane strain. The case of a loaded length shorter than the cylinder length is incorporated by increasing the plane strain fluid pressure required to burst the diaphragm by the ratio of the total length of the cylinder to the loaded length. Applying this ratio to the plane strain pressure is equivalent to reducing the fluid bulk modulus by the inverse of this ratio.

In the analysis, the cylindrical shell material is assumed to be rigid-perfectly plastic. Deformation occurs by means of a mechanism formed by stationary plastic hinges, as shown in Figure 3-13. The locations of the stationary hinges are based on experimental observations, finite element results, and the fluid pressure being the diaphragm burst pressure when the three hinges adjacent to the loading strip become collinear. At each plastic hinge, a fully plastic moment acts; we neglect the membrane force interaction on the moment-thrust yield curve. To simplify the kinematics, we use the geometry of the

chords rather than the arcs between plastic hinges, but in the dynamics we assign the translational and rotational inertia of the arcs to the associated chords.

The kinematic relations and the equations of motion are reduced to a single differential equation governing the rotation of the chords under the loading. The coefficients in this equation are functions of the rotation, so a mathematical simplification consisting of linearization of the coefficients is introduced to allow an explicit solution to be derived. The coefficient of the fluid pressure buildup is also linearized, but the fluid pressure is held constant at a value that produces the same compressional strain energy or resistive work done.

In the analysis, formulas are derived that determine the pressure and impulse required to drive the three plastic hinges under the load into a collinear position in which rotational motion ceases. Two static collapse pressures arise in this problem. The first is the step pressure required to activate the hinge mechanism and the second is the smallest step pressure that drives the three plastic hinges under the load into a collinear position where rotational motion ceases.

Let us consider a long steel cylinder with the following specifications characteristic of Chemical Submunition 2:

Mean radius	a	2.8575 cm (1-1/8 ms)
Mean diameter	d	5.7150 cm (2-1/4 ms)
Wall thickness	h	0.6350 cm (1/4 m)
Bilinear yield stress	σ_y	680 MPa (100,000 psi)
Steel density	ρ	7.80 g/cm ³
Mass	$m = \rho h$	4.953 g/cm ²

We take the initial plastic hinge mechanism as having

Chord AB angle	θ_0	65°
Chord BC angle	$\phi_0 = \pi/2 - \theta_0$	25°
Subtended angle of AB	$\psi_0 = \pi - 2\theta_0$	50°
Chord AB length	$l_1 = d \cos\theta_0$	2.4153 cm
Chord BC length	$l_2 = d \sin\theta_0$	5.1795 cm
Chord AB height	$z_1 = l_1 \cos\theta_0$	1.0207 cm
Chord BC height	$z_2 = l_2 \cos\phi_0$	4.6942 cm
Combined heights	$D = z_1 + z_2 = d$	5.7150 cm
Breadth of chords	$B = l_1 \sin\theta_0$	2.1890 cm

For these values, we find the asymptote to be $\bar{P}_s = 94$ MPa and $I_0 = 124$ ktaps.

Figure 3-14 compares the PI curve derived from this analysis with that obtained from the experiments and finite element analysis. The classical analysis presented here predicts the critical load curve reasonably well and allows the PI curve for diaphragm failure to be determined readily for other parameters, such as a stronger diaphragm or different wall thickness. For example, Figure 3-14 also shows the critical loading curve for a wall thickness of 0.378 cm (1/8-inch), one-half the original wall thickness.

3.5 PRESSURE-IMPULSE CHARACTERIZATION FOR FUZE PLUG RESPONSE.

In the sled tests, a common damage mode was dislodging or removal of the fuze plug. In our experiments on single submunitions, we found that this damage was produced by side impact of the body of the submunition. Below, we analyze this mechanism in detail to determine the critical loads.

When a submunition body is impacted from the side, the inertia of the fuze causes the fuze to rotate about a point on the edge of the base of the fuze as indicated in Figure 3-15. This rotation is resisted by the threads. Below, we determine the critical loads for this mechanism, i.e., the combinations of pressure and impulse applied to the side of the submunition such that the fuze plug rotates a specified amount.

For small angles of rotation (small θ), the equations of motion for the fuze and the body of the submunition are

$$I_{\theta}^* \ddot{\theta} = F_x \frac{h}{2} - F_y \frac{f}{2} - T_o^* \quad (3.1)$$

$$F_x = m \ddot{x} \quad (3.2)$$

$$F_y = m \frac{f}{2} \ddot{\theta} - F_t \quad (3.3)$$

$$P(t)A = (M + m) \ddot{x} \quad (3.4)$$

where

I_{θ}^* = the moment of inertia of the fuze about its center of mass

θ = angle of rotation

F_x = horizontal reaction force on the top of the submunition casing

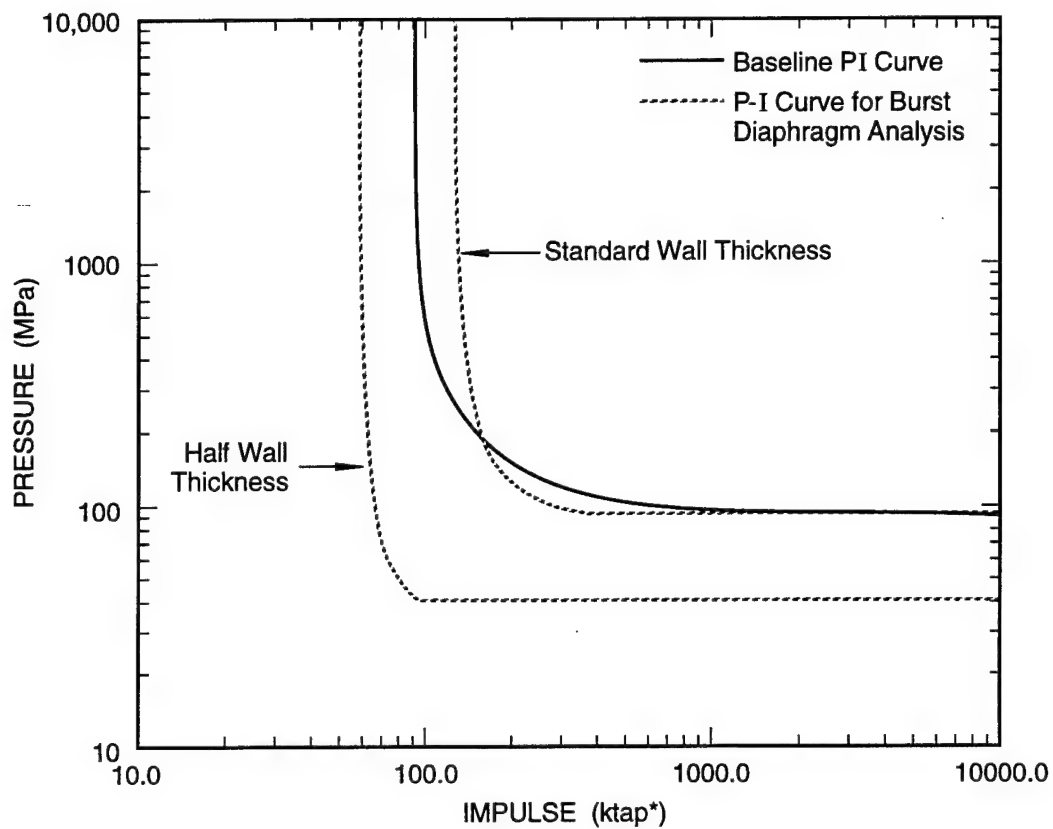
F_y = vertical reaction force on the top of the submunition casing

F_t = vertical force applied by the threads

T_o = torque applied by the threads about the point of rotation

$h/2$ = vertical distance from the center of gravity of the fuze to the top of the threads

$f/2$ = horizontal distance from the center of gravity of the fuze to the edge of the fuze



*1 tap = 1 dyne • s/cm²

Figure 3-14. Comparison of the PI curves calculated for the analytical model of burst diaphragm failure and the baseline PI curve for Chemical Submunition 2.

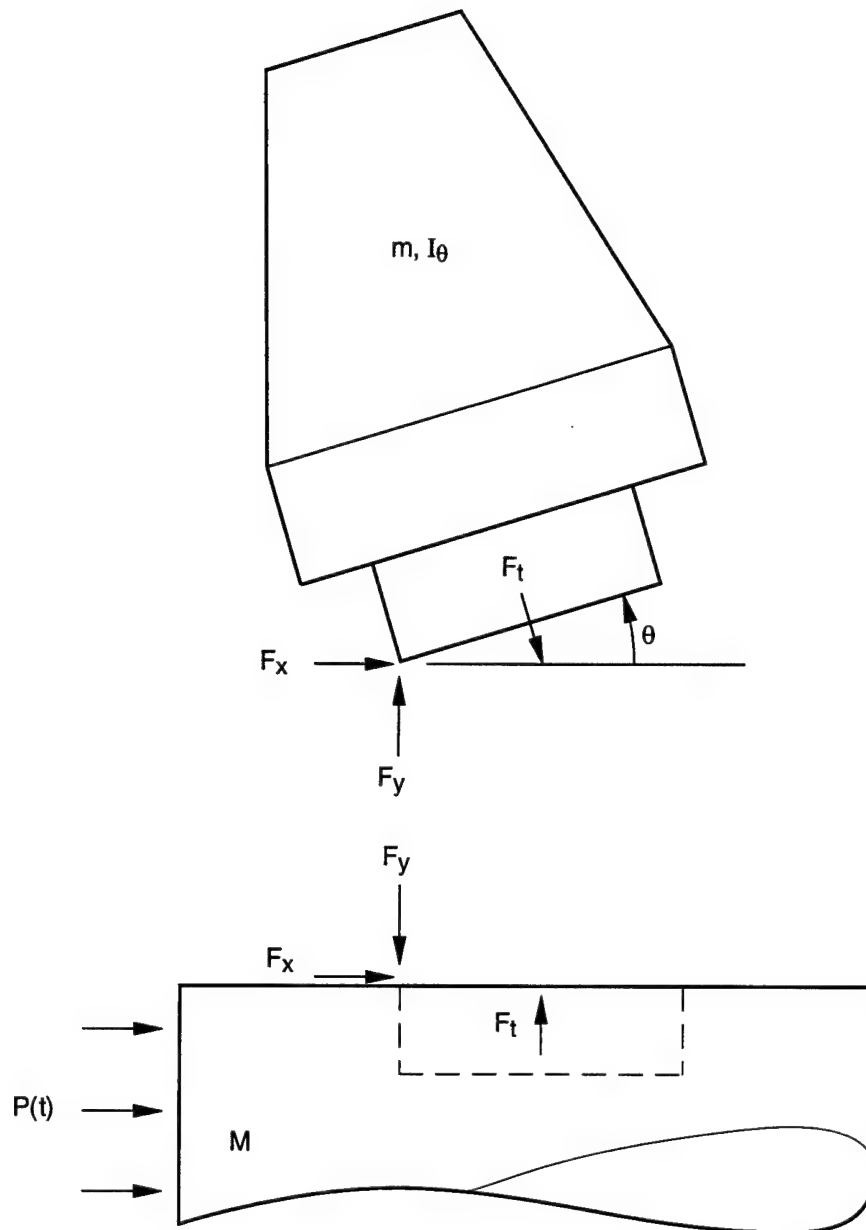


Figure 3-15. Schematic of fuze removal mechanism.

- m = mass of the fuze
 M = mass of the submunition and contents except for the fuze
 $P(t)$ = pressure history applied to the side of the submunition
 A = area of the side of the submunition

Substituting (3.2), (3.3), and (3.4) into (3.1) gives

$$I_{\theta}^* \ddot{\theta} = \frac{mhAP}{2(M+m)} - m\left(\frac{f}{2}\right)^2 \ddot{\theta} - T_0 \quad (3.5)$$

or

$$\left(I_{\theta}^* + \frac{mf^2}{4}\right) \ddot{\theta} = \frac{mhA}{2(M+m)} P - T_0 \quad (3.6)$$

where

$$T_0 = T_0^* - F_t \frac{f}{2} \quad (3.7)$$

Equation (3.6) can be written

$$\ddot{\theta} = P' - T_0' \quad (3.8)$$

where

$$P' = \frac{mhA}{2(M+m) I_{\theta}^*} P$$

$$T_0' = \frac{T_0}{I_{\theta}^*}$$

$$I_{\theta} = I_{\theta}^* + \frac{mf^2}{4}$$

A square loading pulse has two regimes, i.e.

$$P' = P_0' \quad 0 < t \leq \tau$$

$$P' = 0 \quad t > \tau$$

For initial conditions

$$\theta(0) = 0$$

$$\dot{\theta}(0) = 0$$

Equation (3.8) can be integrated the first regime to

$$\dot{\theta} = (P' - T_0')t \quad t \leq \tau$$

$$\theta = (P' - T_0') \frac{t^2}{2} \quad t \geq \tau$$

At the transition between the two regimes $t = \tau$,

$$\dot{\theta}(\tau) = (P' - T_0') \tau \quad (3.9)$$

$$\theta(\tau) = (P' - T_0') \frac{\tau^2}{2} \quad (3.10)$$

In the second regime, for $t > \tau$,

$$\ddot{\theta} = -T_0' \quad (3.11)$$

$$\dot{\theta} = -T_0' t + B \quad (3.12)$$

At $t = \tau$, (3.9) and (3.12) give $B = P'\tau$.

In the second regime,

$$\theta = \frac{-T_0' t^2}{2} + P'\tau t + C \quad (3.13)$$

and at $t = \tau$

$$(P' - T_0') \frac{\tau^2}{2} = -T_0' \frac{\tau^2}{2} + P'\tau^2 + C \quad (3.14)$$

or

$$C = \frac{-P'\tau^2}{2} \quad (3.15)$$

Therefore,

$$\theta = \frac{-T_0' t^2}{2} + P'\tau \left(t - \frac{\tau}{2} \right) \quad (3.16)$$

Fuze rotation stops when $\dot{\theta} = 0$, which, from (3.12), occurs at $t = \frac{P'}{T_0} \tau$. The maximum rotation is then

$$\theta_{\max} = \frac{P' \tau^2}{2} \left(\frac{P'}{T_0} - 1 \right) \quad (3.17)$$

For a square pulse shape, the impulse is given by $I' = P' \tau$ and (3.17) can be written

$$\theta_{\max} = \frac{I'^2}{2} \left(\frac{1}{T_0} - \frac{1}{P'} \right) \quad (3.18)$$

To write (3.18) in the form of the asymptotic values of I' and P' ,

$$\tau \rightarrow 0$$

$$P' \rightarrow \infty$$

and

$$I \rightarrow I_0'$$

so that

$$\theta_{\max} = \frac{I_0'^2}{2 T_0} \quad (3.19)$$

Combining (3.18) and (3.19) gives the nondimensional PI curve

$$\frac{I_0'^2}{I'^2} = \left(1 - \frac{T_0}{P'} \right) \quad (3.20)$$

or, noting that

$$I' = \frac{mhA}{2(M+m)} I_0 I \quad (3.21)$$

we can write (3.20), the PI curve in dimensional form as

$$\frac{I_0^2}{I^2} = \left[1 - \frac{2(M+m) T_0}{mhAP} \right] \quad (3.22)$$

where from (3.19)

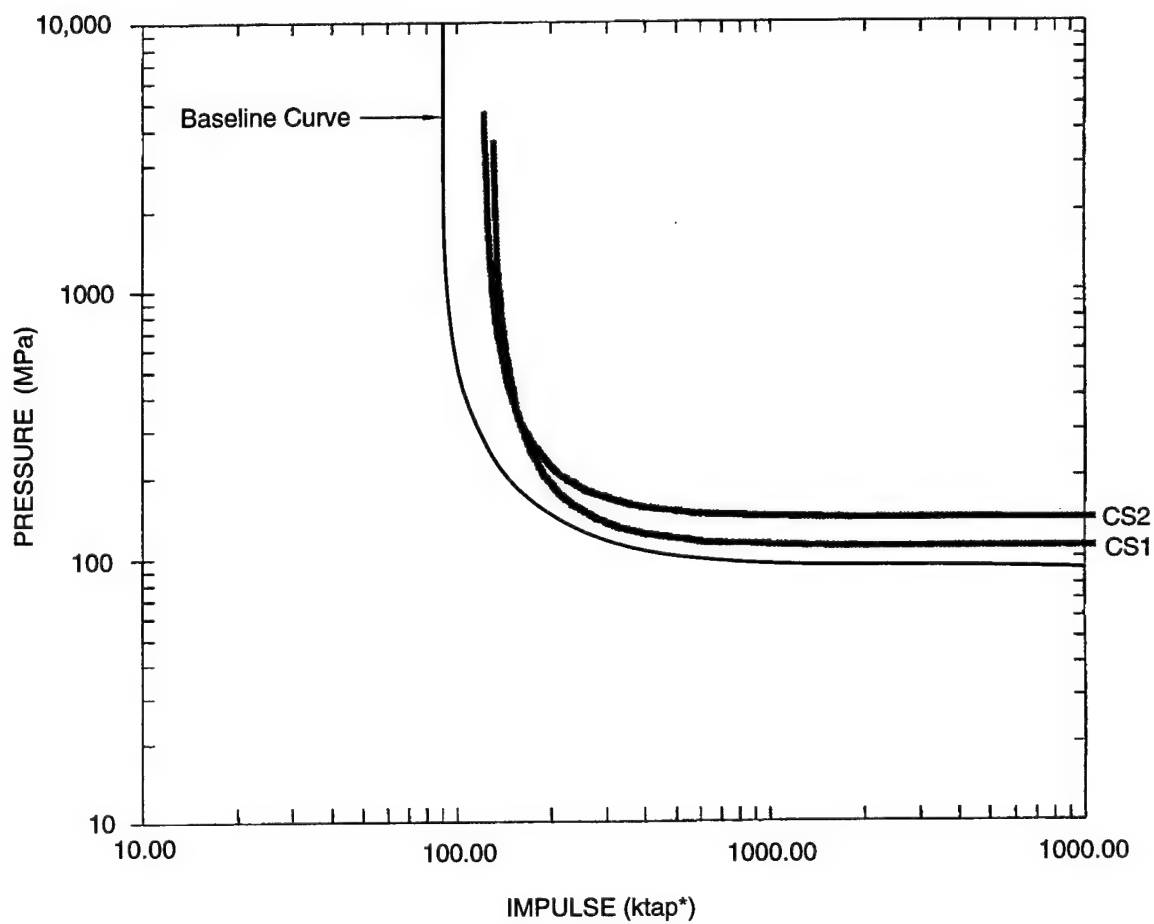
$$I_0 = \frac{2(M+m)}{mhA} \sqrt{2T_0 \theta_{\max} I_0} \quad (3.23)$$

The PI curves for Chemical Submunitions 1 and 2 were calculated using the following values:

		<u>Chemical Submunition 1</u>	<u>Chemical Submunition 2</u>
M	g	6535	3916
m	g	607	470
h	cm	2.24	1.38
A	cm ²	83.1	65.6
T ₀	dyne cm	3.47 x 10 ¹⁰	2.71 x 10 ¹⁰
θ _{max}	radians	0.03	0.03
I _θ	g cm ²	3035	1267

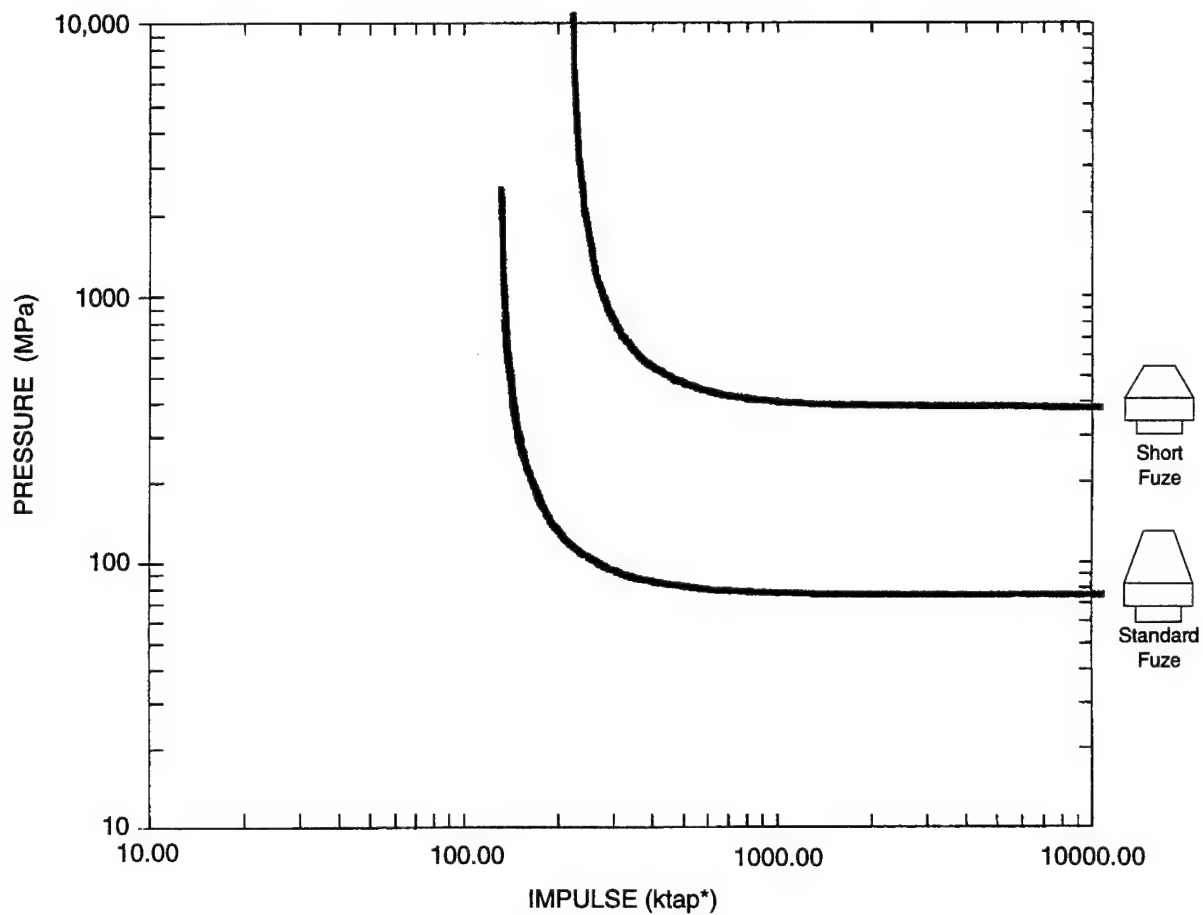
Figure 3-16 compares the PI curves for fuze removal for both submunitions with the baseline curve for Chemical Submunition 2. The value of T₀ and θ_{max} fall in a range consistent with the observed behavior of fuze removal. The particular values chosen are those that give best agreement with the data.

An example of the utility of this analysis is that it can be used to determine quickly the effect of changing the target parameters. Figure 3-17 shows the effect of reducing the length of the fuze on Chemical Submunition 2 while keeping all other parameters constant. The simplicity of the fuze analysis and the ease of investigating a number of parameters makes it a suitable tool for lethality assessments.



*1 tap = 1 dyne • s/cm²

Figure 3-16. PI curves for fuze removal compared to baseline curve for Chemical Submunition 2.



*1 tap = 1 dyne • s/cm²

Figure 3-17. PI curves for standard and short fuze in Chemical Submunition 2.

SECTION 4

SCALING EVALUATION

The objective of this investigation was to establish whether the impact response of complete targets with arrays of chemical submunitions can be reliably obtained from subscale tests (Colton et al., 1994). We first examined the results from tests of complete targets with submunition arrays conducted at the Holloman Sled Test Track (full-scale) and at the Arnold Engineering Development Center (quarter-scale). The damage modes in the full- and quarter-scale tests consisted primarily of fragmentation of the submunitions, failure of the burst diaphragm, removal of the fuze plug, failure of the weld between the case and the top and bottom of the submunition (full-scale only), and fracture of the casing. In the specimens we examined, fracture of the casing was accompanied by one of the other failure modes, usually failure of the burst diaphragm. This dual failure always occurred in the 1/4-scale experiments, and in the full-scale experiments with few exceptions.

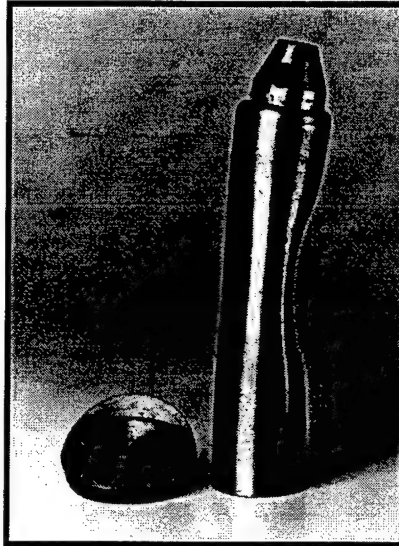
Examination of the fragments assumed to be produced in the impact area, in both the full- and quarter-scale tests, showed that the fragment size distributions essentially scale. To investigate structural damage modes, we performed tests in which plates at 200 m/s impacted full-, half-, and quarter-scale single submunitions on the side both at the midheight and near the top of the submunitions. We found that the fuze failure and diaphragm failure modes and the overall deformation of the submunitions were essentially the same at all scales. In the full-scale submunitions with welds, identical to those submunitions used in full-scale sled tests, weld failure occurred as it often did in the sled tests. We also made and tested full-scale submunitions without welds and found that the responses were nearly identical to those in the 1/4-scale (unwelded) submunition: no failures in the case, failure of the burst diaphragm, and partial removal of the fuze plug.

Figure 4-1 shows a comparison of the damage to full-, half-, and quarter-scale models impacted on the side at midlength. Radial deformation and diaphragm rupture in the three models are faithfully replicated. The fuze plug was removed in the half-scale model; in the full- and quarter-scale model, the fuze plug was dislodged to cause a large leak. Table 4-1 summarizes the deformations and volume changes for comparable full and scale models. The slightly lower deformation and volume change for the half-scale shoulder impact experiment is consistent with a slightly off-center impact on this test. However, the combination of deformation and volume change is self-consistent. Nevertheless, it is clear that, under equal impact conditions, the damage sustained by each model size is very similar.

Welded Full-Scale



Unwelded Full-Scale



Unwelded Quarter-Scale

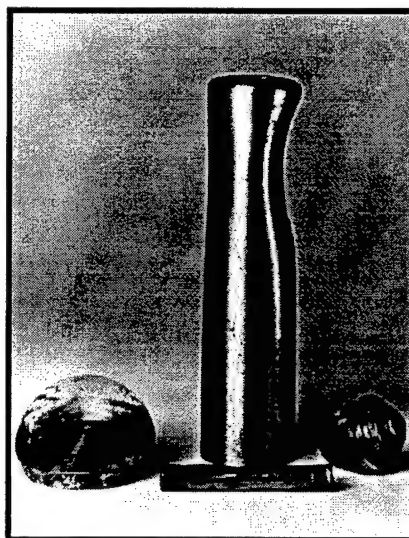


(a) At Center

Welded Full-Scale



Unwelded Full-Scale




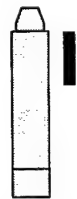
Quarter-Scale



(b) At Shoulder

Figure 4-1. Comparison of damage in different sizes of Chemical Submunitions 2 subjected to side-on impact.

Table 4-1. Deformation and volume change measurements for Chemical Submunitions 2 impact tests.

Impact Location	Full-Scale Welded		Full-Scale Unwelded		1/2-Scale Welded		1/4-Scale Unwelded	
	$\Delta R/R_o$ (%)	$\Delta V/V_o$ (%)	$\Delta R/R_o$ (%)	$\Delta V/V_o$ (%)	$\Delta R/R_o$ (%)	$\Delta V/V_o$ (%)	$\Delta R/R_o$ (%)	$\Delta V/V_o$ (%)
	62.5	7.2	56.9	6.6	53.1	6.7	57.1	6.5
	44.3	6.2	53.4	5.4	40.0	4.3	49.2	5.0

ΔR = radius change; R_o = original radius; ΔV = volume change; V_o = original volume.

Finally, we examined in detail the fractures in the submunition casings from the full-scale sled tests and the quarter-scale gun tests. We found that, in the full-scale submunitions, cleavage fractures were large and more or less straight. Such fractures are common for thicker-walled structures and can also be induced by the failure of the weld at the top of the case. In contrast, the quarter-scale submunitions always fractured by ductile void growth, which results in jagged tearing axial fractures associated with large plastic deformations, and circumferential shear fractures in the regions stiffened by the closures. In our tests, we found that, although the measured stress-strain properties for the full- and quarter-scale materials were essentially the same, the effective fracture resistance of the quarter-scale material was greater than that of the full-scale material because of the differences in fracture mode.

We conclude that the only significant difference in response between full- and quarter-scale submunitions was in fracture of the casing including weld fracture. Thus, if lethality requires the casing to be fractured, the loads required to produce this response will be greater at quarter-scale than at full-scale and lethality estimates from the scaled tests will be conservative. If lethality relies on diaphragm failure and fuze failure, the dominant failure modes observed, no significant scaling differences are expected between the full- and quarter-scale tests. In either case, the small-scale test results are useful. They can be used to investigate response modes that lead to lethality. At a minimum, small-scale tests can be used to determine lower bounds on the loads required for lethality. In many cases, they can be used to quantify the critical loads.

SECTION 5

CONCLUSIONS

Our work was performed primarily to determine the relationship between the load and response of individual submunitions, particularly those that are away from the impact area where the impact velocities are hundreds of meters per second. The load-damage relationship is a link between (1) measurements that can be made in sled tests and calculated in the most sophisticated codes available (e.g., internal submunition pressure), and (2) the final damage to individual submunitions. We conclude that

- Damage modes in the submunitions recovered from sled tests included
 - Fragmentation caused by the large stresses produced in the vicinity of the impact
 - Failure of the weld between the top and the cylindrical casing
 - Fracture of the casing
 - Rupture of the burst diaphragm by the internal pressure
 - Removal of the fuze caused by the impact of fragments and submunitions against the submunition away from the impact point
- Rupture of the burst diaphragm and removal of the fuze were the most prevalent failure modes.
- The fuzes in Chemical Submunitions 1 and 2 acted as good energy absorbers that protected the body of the submunition. The shoulder was weakest, because the weld between the top and the main body of the submunition frequently failed. For side impact, the damage mechanism was frequently rupture of the burst diaphragm or fuze removal.
- The failure of the diaphragm is largely a dynamic phenomena of the fluid. Therefore, the amount of ullage (at least up to 15%) and its location were not important in damage to the ruptured diaphragm.
- For Chemical Submunition 2 for side loading, the pressure-impulse curve for internal pressure could be related to the pressure-impulse curve for external loads.
- For a range of pulse durations on Chemical Submunition 2, the external critical loads changed by an order of magnitude while the internal loads varied by only a factor of 2 because the response of the fluid was moderated by the strength of the submunition.
- PI curves derived from simplified analyses for side impact that produces diaphragm or fuze failure can be used to predict responses for a range of parameters of interest. The critical load for side loading is greatly increased if the height of the fuze is decreased.

- Submunitions could survive impacts that imparted velocities up to about 65 m/s. This is a direct input into a post-engagement analysis to determine the footprint on the ground.
- Most of the damage mechanisms are the same in the full-, half-, and quarter-scale submunitions, notably diaphragm and fuze failure. Differences in the damage to the submunition casing resulted from differences in construction (welds versus no welds--not a true scaling difference) and because the quarter-scale material fractured at greater loads than the full-scale material. Thus if fracture of the submunition casing is a significant damage mode of interest, care must be taken in interpreting the results.

We recommend that

- Additional experiments be carried out, particularly on Submunition 1, to complete the critical load curves for external and internal loads and for multiple impacts.
- Simplified models be developed for loading over a portion of the side of the submunition, for axial impact, and for internal loads for loading other than side area loading.
- The critical load curves developed be integrated into lethality assessment codes such as KAPPII.
- Additional experiments be conducted to refine the critical survival velocity imparted to an impacted submunition by glancing blows and multiple impacts. Post-engagement analyses of the results should also be conducted.

SECTION 6

REFERENCES

- Mullins, S. E., G. B. Booth, and C. S. Fowler, "ERINT Hit-to-Kill Sled Tests Against Chemical Submunition Target (U)," Technical Report SEAS-SDC-3390, Teledyne Brown Engineering, Contract No. DASG60-92-C-0036, October 1992. (SECRET)
- Smith, V. M. and S. L. Durham, "FY92 Quarter-Scale Hit-to-Kill Chemical Submunition Test Series, Volume II: Pretest Timing Calculations for the FY92 Quarter-Scale Chemical Submunition Test Series (U)," Final Report WL-TR-93-7053, Kaman Sciences Corporation, Contract No. F08635-91-C-0008 (July 1993). (SECRET)
- Colton, J. D., J. H. Giovanola, and D. R. Curran, "Modes of Damage to Submunition Threat Simulators in Sled Tests (U)," Topical Report on Project 4727, Defense Nuclear Agency, Contract No. DNA 001-93-C-0104, November 1993. (SECRET)
- Lindberg, H. E. and J. D. Colton, "Sheet Explosive Simulation for Combined Shock and Structural Response," Technical Report AFWL-TR-69-124, SRI Project 6599, Air Force Weapons Laboratory, September 1970. (UNCLASSIFIED)
- Whirley, R. G., "DYNA3D (A Nonlinear, Explicit, Three-Dimensional Finite Element Code for Solid and Structural Mechanics) Users Manual," Lawrence Livermore National Laboratory, Report UCRL-MA-107254, November 1993. (UNCLASSIFIED)
- Cooper, T., "A Computer Code for Numerical Simulation of Shock Waves in Fluids and Solids," Report DS 1980:16, 1980. (UNCLASSIFIED)
- Abrahamson, G. R. and H. E. Lindberg, "Peak Load-Impulse Characterization of Critical Pulse Loads in Structural Dynamics," Proceedings of a Symposium held at Stanford University, California, June 28 and 29, 1971. (UNCLASSIFIED)
- Colton, J. D. et al., "Evaluation of Subscale Testing of Chemical Submunitions—Full vs. Subscale Testing," Topical Report on Project 4727, Defense Nuclear Agency, Contract No. DNA 001-93-C-0104, June 1994. (UNCLASSIFIED)

APPENDIX A

PRESSURE-IMPULSE CURVES FOR COMPLEX PULSES

INTRODUCTION

Pressure-impulse (PI) representations of isodamage curves are well established for basic structural components (such as beams, plates, and cylindrical shells) subjected to basic pulse shapes, such as idealized forms of sudden or blast loadings, which include the rectangle, triangle, and exponential. Here, we describe a method for obtaining the PI relationship for a pulse that is more general than the usual basic shape. To do this, we have chosen probably the simplest generalization, which consists of a class of pulses with general variations in pressure about a rectangular pulse. We have chosen a rigid, perfectly plastic circular membrane as our basic structural component. This choice sprang from a requirement to analyze the thin diaphragm that forms the base of a cylindrical submunition containing fluid. The loading is caused by the rise in fluid pressure when the submunition receives an impact from external objects, such as an adjacent submunition.

A rigid-plastic material behavior is reasonable because we are considering strains that are many times the yield strain, and the failure criterion is taken as the biaxial elongation. The initial bending response has been ignored in the analysis. In fact, for the practical dimensions chosen, the central deflection is less than the thickness when membrane forces dominate bending resistance. A shortcoming of the analysis is probably the failure criterion. We predict that the maximum strain occurs at the center, whereas experimental results show failure at the supports. The different behavior is attributed to a stress concentration at the support caused by localized bending combined with the membrane tension. One may possibly overcome this shortcoming by empirically reducing the central elongation strain.

We have restricted the analysis to pulses that cause the membrane to come to rest after the entire pulse has been applied. For pulses that are variations about a rectangular pulse, the restriction is not severe. For pulses that are variations about other standard shapes, such as a half sine, the analysis requires modification to account for cases in which motion can cease while the pulse is still being applied.

In the analysis, we have assumed that the motion is dominated by the first or fundamental spatial mode. The analysis can be modified to include higher modes. Probably, three modes would provide a fairly accurate description of the mechanics.

Fluid-structure interaction was examined, but is not included here because the fluid against the membrane is confined within the cylindrical walls. Spatial pressure equalization occurs because the fluid

radial wave transit time is very short relative to the pulse duration, except for pulses that approach an ideal impulse. For these extreme cases, we have chosen not to include the effect of fluid-structure interaction; the consequence is that for extremely short pulses our impulse values are low.

The main result of the analysis is that the PI relationship for the rectangular pulse is not affected strongly by the pressure variations about the mean even when the variations are large.

STATIC MEMBRANE RESPONSE

Figure A-1 shows the displacements and in-plane forces of a rigid, perfectly plastic membrane subjected to a static pressure. An element dr of radius changes its length to ds as a result of the vertical and radial deflections $w(r)$ and $v(r)$, as shown in Figure A-1(a). The corresponding radial and tangential strains are

$$\epsilon_r = \frac{ds - dr}{dr} = [(1 + v')^2 + w'^2]^{1/2} - 1 \quad (\text{A.1})$$

$$\epsilon_\theta = \frac{v}{r} \quad (\text{A.2})$$

where primes have been introduced to indicate differentiation with respect to r .

We postulate that the membrane forces are equal and have the value corresponding to the yield stress; that is,

$$N_\theta = N_r = N_0 = \sigma_0 h \quad (\text{A.3})$$

where σ_0 is the yield stress and h is the membrane thickness. This stress state lies on the von Mises yield ellipse

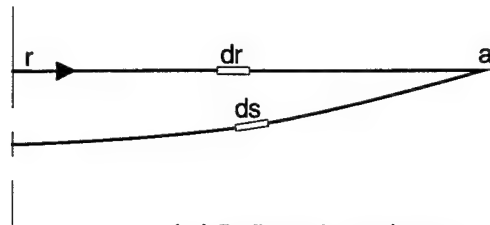
$$N_r^2 - N_r N_\theta + N_\theta^2 = N_0^2 \quad (\text{A.4})$$

The loading is proportional, so we can represent the associated flow rule in the form of the Levy-Mises equations

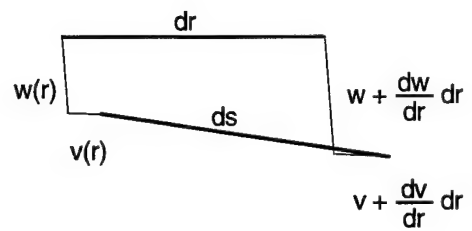
$$\frac{\epsilon_r}{N_r'} = \frac{\epsilon_\theta}{N_\theta'} = \frac{\epsilon_z}{N_z'} = \frac{3}{2} \frac{\epsilon}{N_0} \quad (\text{A.5})$$

where N_r' , N_θ' , and N_z' are the deviatoric forces defined by

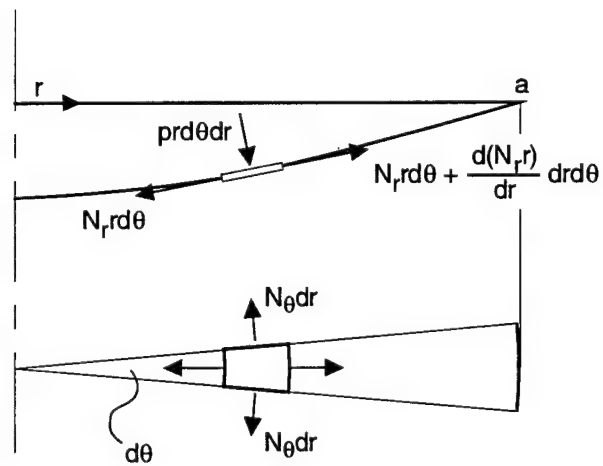
$$N_r' = N_r - N_m \quad N_\theta' = N_\theta - N_m \quad \text{and} \quad N_z' = N_z - N_m \quad (\text{A.6})$$



(a) Deflected membrane



(b) Element displacements



(c) Forces on an element

Figure A-1. Elemental displacements and forces.

with the mean force defined by

$$N_m = \frac{1}{3} (N_r + N_\theta + N_z) \quad (A.7)$$

The stress through the membrane thickness is ignored ($N_z = 0$), so

$$N_r' = \frac{2}{3} (N_r - \frac{1}{2} N_\theta) \quad N_\theta' = \frac{2}{3} (N_\theta - \frac{1}{2} N_r) \quad N_z' = -\frac{1}{3} (N_r + N_\theta) = -N_m \quad (A.8)$$

and when $N_\theta = N_r = N_0$, we obtain the deviatoric values

$$N_\theta' = N_r' = \frac{1}{3} N_0 \quad N_z' = -\frac{2}{3} N_0 = -N_m \quad (A.9)$$

In the flow rule (A.5), ϵ is the equivalent plastic strain defined by

$$\epsilon = \frac{2}{\sqrt{3}} (\epsilon_r^2 + \epsilon_r \epsilon_\theta + \epsilon_\theta^2)^{1/2} \quad (A.10)$$

for a plastically incompressible material ($\epsilon_r + \epsilon_\theta + \epsilon_z = 0$). From (A.9), the deviatoric membrane forces N_θ' and N_r' are equal, so the flow rule (A.5) gives

$$\epsilon_\theta = \epsilon_r \quad (A.11)$$

and, from (A.10), the equivalent plastic strain becomes

$$\epsilon = 2\epsilon_\theta = 2\epsilon_r \quad (A.12)$$

The result (A.11) is consistent with the plastic strain vector being normal to the yield ellipse at the stress state $N_r = N_\theta$. We need this result to determine the radial displacement, as shown below.

In our treatment of the equilibrium equations, we assume at the outset that the displacements and slopes are small enough to allow the use of the coordinate r (Lagrangian) and the approximate expressions for the two principal curvatures

$$\kappa_r = -w'' \quad \kappa_\theta = -\frac{1}{r} w'$$

By resolving forces perpendicular and tangential to the membrane element, we obtain

$$N_r w'' + N_\theta \frac{1}{r} w' = -p_0 \quad (A.13)$$

and

$$(rN_r)' = N_\theta \quad (A.14)$$

Equation (A.14) is satisfied by $N_\theta = N_r = N_0$ and this stress state simplifies (A.13) to

$$w'' + \frac{1}{r} w' = - \frac{p_0}{N_0} \quad (A.15)$$

The solution of equation (A.15) that satisfies the conditions of zero deflection at the boundary $r = a$ and zero slope at the center is

$$w = \frac{k}{a} (a^2 - r^2) \quad k = \frac{p_0 a}{4N_0} \quad (A.16)$$

The value of the constant k is generally small enough to allow the radial strain expression (A.1) to be approximated by

$$\epsilon_r = v' + \frac{1}{2} w'^2 \quad (A.17)$$

Equating the strains ϵ_r and ϵ_θ as required by (A.12) gives

$$v' - \frac{v}{r} = - \frac{1}{2} w'^2 \quad w' = - \frac{2k}{a} r \quad (A.18)$$

The solution of equation (A.18) that satisfies the conditions of zero radial displacement at the center and the support ($r = a$) is

$$v = k^2 r \left(1 - \frac{r^2}{a^2} \right) \quad (A.19)$$

The displacements (A.16) and (A.19) give the strains

$$\epsilon_\theta = \epsilon_r = k^2 \left(1 - \frac{r^2}{a^2} \right) \quad (A.20)$$

the maximum being at the center. Setting $r = 0$ in (A.20) gives

$$\max \epsilon_\theta = \max \epsilon_r = \epsilon_\theta(0) = \epsilon_r(0) = k^2 \quad (A.21)$$

If the maximum plastic strain in a failure criterion is ϵ_f , then (A.21) with k given by (A.16) shows that the failure pressure p_f is

$$p_f = 4 \frac{h}{a} \sigma_0 \sqrt{\epsilon_f} \quad (A.22)$$

The central deflection at this pressure according to (A.16) is

$$w_f = ka = a\sqrt{\epsilon_f} \quad (\text{A.23})$$

As an example, a membrane of thickness $h = 0.318$ cm (1/8 in.) and radius $a = 2.54$ cm (1 in.) made of steel with a yield stress of $\sigma_o = 612$ MPa (90,000 psi, $\epsilon_y = 0.3\%$) has a maximum strain of $\epsilon_f = 0.8\%$ when the pressure is $p_f = 27.2$ MPa (4000 psi); the central deflection is $w_f = 0.226$ cm ($w_f = 0.72 h$). As an interesting comparison, the static collapse pressure of this disk, when it is regarded as a rigid-plastic clamped circular plate, is

$$p_s = 2.82 \left(\frac{h}{a}\right)^2 \sigma_o = 27 \text{ MPa (3966 psi)}$$

If we are concerned with large failure strains, the membrane forces begin to dominate bending after small deflections; however, the support hinge circle will introduce initial strain concentrations. The plate has a collapse mechanism when p_s is reached, whereas the membrane does not have a collapse mechanism; additional pressure is needed to generate additional deflection or strain, which is a geometric effect.

DYNAMIC MEMBRANE RESPONSE

For the dynamic response, we add the inertial term $m\ddot{w}$ to the right-hand side of the static equilibrium equation (A.13); $m = \rho h$ is the membrane mass per unit surface area, and the dots denote time differentiation. Again, setting $N_\theta = N_r = N_o$ leads to

$$\ddot{w} - c^2 \left(w'' + \frac{1}{r} w' \right) = \frac{p(t)}{m} \quad c^2 = N_o/m = \sigma_o/\rho \quad (\text{A.24})$$

In this analysis, we ignore the effect of the radial inertia; a comparison of the vertical and radial displacement expressions (A.16) and (A.19) shows that $v = 0(kw)$ where the parameter k in (A-16) is small.

If we introduce the dimensionless quantities

$$x = r/a \quad y = w/a \quad \tau = ct/a \quad q(\tau) = p(t)a/N_o \quad (\text{A.25})$$

equation (A.24) can be put in the convenient dimensionless form

$$\ddot{y} - \left(y'' + \frac{1}{x} y' \right) = q(\tau) \quad (\text{A.26})$$

where

$$(\)^{\circ} = \partial/\partial\tau \quad (\)' = \partial/\partial x$$

The initial conditions are taken as zero displacement and velocity

$$y(x,0) = \dot{y}(x,0) = 0 \quad (A.27)$$

and the boundary conditions as

$$y(1,t) = 0 \quad (A.28)$$

A solution to equation (A.26) with the initial and boundary conditions (A.27) and (A.28) for a pulse loading $q(\tau)$ can be obtained readily in modal form. The appropriate modal form for a loading $q(x,\tau)$ is the Fourier-Bessel expansion

$$q(x,\tau) = \sum_{n=1}^{\infty} q_n(\tau) J_0(\alpha_n x) \quad (A.29)$$

where the sequence of numbers α_n are roots of $J_0(\alpha_n) = 0$. In (A.29), J_0 is a Bessel function of order zero. As a reminder, the properties of the orthogonal expansion are

$$\int_0^1 x J_0(x\alpha_m) J_0(x\alpha_n) dx = \begin{cases} 0 & m \neq n \\ \frac{1}{2} J_1^2(\alpha_n) & m = n \end{cases}$$

and

$$q_n(\tau) = \frac{2}{J_1^2(\alpha_n)} \int_0^1 q(x,\tau) x J_0(x\alpha_n) dx$$

For a load that is uniformly distributed over the membrane

$$q_n(\tau) = \frac{2q(\tau)}{\alpha_n J_1(\alpha_n)} \quad (A.30)$$

If we represent the deflection $y(x, \tau)$ by the expansion

$$y(x, \tau) = \sum_{n=1}^{\infty} y_n(\tau) J_0(\alpha_n x) \quad (\text{A.31})$$

along with the loading expansion (A.29) in equation (A.26) and equate the coefficients of the modes $J_0(\alpha_n x)$, we obtain the set of ordinary differential equations for the time dependent coefficients:

$$\ddot{y}_n + \alpha_n^2 y_n = q_n(\tau) \quad (\text{A.32})$$

with $q_n(\tau)$ given by (A.30).

The solutions of equations (A.32) that satisfy the initial conditions $y_n(x, 0) = \dot{y}_n(x, 0) = 0$ are

$$\alpha_n y_n(\tau) = \sin \alpha_n \tau \int_0^{\tau} q_n(s) \cos \alpha_n s ds - \cos \alpha_n \tau \int_0^{\tau} q_n(s) \sin \alpha_n s ds \quad (\text{A.33})$$

The velocities of the modal amplitudes are

$$\dot{y}_n(\tau) = \cos \alpha_n \tau \int_0^{\tau} q_n(s) \cos \alpha_n s ds + \sin \alpha_n \tau \int_0^{\tau} q_n(s) \sin \alpha_n s ds \quad (\text{A.34})$$

We now restrict our attention to the simplest class of pulses. These pulses are such that the membrane is still in motion when the pulse ends. The simplest example of this class is a rectangular pulse of sufficiently high magnitude. We assume as an approximation that the time $\bar{\tau}$ at which the membrane comes to rest is based on the first mode, that is, $\dot{y}_1(\bar{\tau}) = 0$. Let the pulse duration be $\bar{\tau}$. Then, for motion ceasing after the pulse has been applied, (A.33) and (A.34) become

$$\alpha_n y_n(\tau) = C_n \sin \alpha_n \tau - S_n \cos \alpha_n \tau \quad (\text{A.35})$$

$$\dot{y}_n(\tau) = C_n \cos \alpha_n \tau + S_n \sin \alpha_n \tau \quad (\text{A.36})$$

where

$$C_n = \int_0^{\bar{\tau}} q_n(\tau) \cos \alpha_n \tau d\tau \quad S_n = \int_0^{\bar{\tau}} q_n(\tau) \sin \alpha_n \tau d\tau \quad (\text{A.37})$$

The duration of motion, $\tilde{\tau}$, is the solution of $\dot{y}_1(\tilde{\tau}) = 0$; that is,

$$\tan \alpha_1 \tilde{\tau} = -\frac{C_1}{S_1} \quad (\text{A.38})$$

and substitution of $\tilde{\tau}$ in (A.35) provides an approximation to the displacement amplitudes $y_n(\tilde{\tau})$ when the membrane has come to rest.

The dimensionless forms of the strain equations are

$$\epsilon_r = z' + \frac{1}{2} y'^2 \quad \epsilon_\theta = \frac{z}{x} \quad z = \frac{v}{a} \quad (\text{A.39})$$

If we again postulate that $\epsilon_r = \epsilon_\theta$, ($N_r = N_\theta$), we obtain

$$\epsilon_\theta' = \left(\frac{z}{x} \right)' = -\frac{1}{2} \frac{y'^2}{x} \quad (\text{A.40})$$

Then, considering only the contribution of the first mode to the strains, the spatial integration of (A.40) gives

$$\epsilon_\theta = \frac{1}{4} \alpha_1^2 [1 - J_1^2(\alpha_1)] y_1^2 \quad (\text{A.41})$$

as the strain at the center of the membrane, where it is greatest. Let this strain be the failure strain ϵ_f . Then, to produce this strain, the amplitude of the first mode when motion ceases must be

$$y_1(\tilde{\tau}) = \frac{2\epsilon_f^{1/2}}{\alpha_1 [1 - J_1^2(\alpha_1)]^{1/2}} \quad (\text{A.42})$$

The first root of $J_0(\alpha) = 0$ is $\alpha_1 = 2.40$, which gives $J_1(\alpha_1) = 0.52$, so the value resulting from (A.42) is $y_1(\tilde{\tau}) = 1.14 \epsilon_f^{1/2}$. When $\epsilon_f = 0.1$, we have $y_1(\tilde{\tau}) = 0.36$, so $w_1(\tilde{\tau}_f)$ is about one-third of the membrane radius.

Before treating a general pulse, we apply our analysis to a rectangular pulse as an illustration of our approximate analysis and to establish results for general pulses with shapes that can be regarded as variations about a rectangular pulse.

RECTANGULAR PULSE

Our rectangular pulse is defined by

$$p(t) = \begin{cases} \bar{p} & 0 < t < \bar{t} \\ 0 & t > \bar{t} \end{cases} \quad q(\tau) = \begin{cases} \bar{q} & 0 < \tau < \bar{\tau} \\ 0 & \tau > \bar{\tau} \end{cases} \quad (\text{A.43})$$

where the dimensionless pressure $q(\tau)$ and time τ are related to $p(t)$ and t through (A.25). The integrals C_n and S_n in (A.37), according to (A.30) and (A.43), become

$$\bar{C}_n = \frac{2\bar{q}}{\alpha_n J_1(\alpha_n)} \cdot \frac{\sin \alpha_n \bar{\tau}}{\alpha_n} \quad \bar{S}_n = \frac{2\bar{q}}{\alpha_n J_1(\alpha_n)} \cdot \frac{1 - \cos \alpha_n \bar{\tau}}{\alpha_n} \quad (\text{A.44})$$

Thus, (A.35) and (A.44) give the modal displacement amplitudes $\tilde{y}_n = y_n(\bar{\tau})$ at time $\bar{\tau}$ in the form

$$\tilde{y}_n = \frac{2\bar{q}}{\alpha_n^3 J_1(\alpha_n)} [\sin \alpha_n \bar{\tau} \sin \alpha_n \bar{\tau} - \cos \alpha_n \bar{\tau} (1 - \cos \alpha_n \bar{\tau})] \quad (\text{A.45})$$

where the duration of motion is assumed to be determined by the first mode. Hence, by (A.38) and (A.44), $\bar{\tau}$ is the solution of

$$\tan \alpha_1 \bar{\tau} = -\bar{C}_1 / \bar{S}_1 = -\sin \alpha_1 \bar{\tau} / (1 - \cos \alpha_1 \bar{\tau}) \quad (\text{A.46})$$

or

$$\sin \alpha_1 \bar{\tau} = \cos(\alpha_1 \bar{\tau} / 2) \quad \cos \alpha_1 \bar{\tau} = -\sin(\alpha_1 \bar{\tau} / 2) \quad (\text{A.47})$$

Expression (A.47) allows us to simplify the formula for the first modal amplitude among the set (A.45) to

$$\tilde{y}_1 = \frac{4\bar{q}}{\alpha_1^3 J_1(\alpha_1)} \sin \frac{\alpha_1 \bar{\tau}}{2} \quad (\text{A.48})$$

By means of (A.42), we can relate the pulse amplitude and duration to the failure strain. This relationship is

$$\bar{q} \sin \frac{\alpha_1 \bar{\tau}}{2} = \frac{\alpha_1^2 J_1(\alpha_1)}{2[1 - J_1^2(\alpha_1)]^{1/2}} \epsilon_f^{1/2} \quad (\text{A.49})$$

The numerical value of the coefficient of $\epsilon_f^{1/2}$ is 1.76.

We are considering rectangular pulses of magnitudes and durations that do not allow the membrane to come to rest until after the pulse has ended ($\tilde{\tau} > \bar{\tau}$). The lowest pressure to ensure this condition occurs when the pulse duration and the motion are equal ($\tilde{\tau} = \bar{\tau}$).

When we let $\tilde{\tau} = \bar{\tau}$ in (A.46) or (A.47), we find that $\bar{\tau} = \pi/\alpha_1$. Substitution of $\alpha_1 \bar{\tau} = \pi$ in (A.49) gives the lowest \bar{q} that can be applied to the membrane to produce the failure strain ϵ_f . With this minimum \bar{q} denoted by \bar{q}_0 , (A.49) gives

$$\bar{q}_0 = \frac{\alpha_1^2 J_1(\alpha_1)}{2[1 - J_1^2(\alpha_1)]^{1/2}} \epsilon_f^{1/2} = 1.76 \epsilon_f^{1/2} \quad (\text{A.50})$$

For values of $\bar{q} < \bar{q}_0$, the membrane comes to rest while the pulse is still being applied. A modification of the analysis is required to treat cases in which the membrane comes to rest when the maximum strain is ϵ_f while the pulse is still being applied.

The other extreme of the set of rectangular pulses is the ideal impulse defined by

$$i_0 = \lim_{\bar{\tau} \rightarrow 0} \int_0^{\bar{\tau}} q(\tau) d\tau \quad (\text{A.51})$$

in terms of dimensionless pressure and time. For a rectangular pulse, the limiting process applied to \bar{C}_1 and \bar{S}_1 in (A.44) gives

$$\bar{C}_1 = \frac{2i_0}{\alpha_1 J_1(\alpha_1)} \quad \bar{S}_1 = 0 \quad (\text{A.52})$$

and when it is applied to (A.46) or (A.47), we obtain the duration of motion $\tilde{\tau} = \pi/2\alpha_1$. The amplitude of the first mode, obtained from (A.48), becomes

$$\tilde{y}_1 = \frac{2i_0}{\alpha_1^2 J_1(\alpha_1)} \quad (\text{A.53})$$

and according to (A.49), the ideal impulse required to produce the failure strain ϵ_f is

$$i_0 = \frac{\alpha_1 J_1(\alpha_1)}{[1 - J_1^2(\alpha_1)]^{1/2}} \epsilon_f^{1/2} \quad (\text{A.54})$$

A dimensionless form of the PI relationship is readily derived from the results of (A.49), (A.50), and (A.54). From (A.49) and (A.54)

$$\frac{\bar{q}}{\bar{q}_0} \sin \frac{\alpha_1 i}{2\bar{q}} = 1 \quad i = \bar{q} \bar{\tau} \quad (\text{A.55})$$

Equations (A.50) and (A.54) show that $\bar{q}_0/i_0 = \alpha_1/2$, so after λ and μ are set as follows,

$$\lambda = \bar{q}/\bar{q}_0 \quad \mu = i/i_0$$

Equation (A.55) gives the PI relationship

$$\lambda \sin(\mu/\lambda) = 1 \quad (\text{A.56})$$

In terms of physical quantities

$$\begin{aligned} \lambda &= \bar{p}/\bar{p}_0 & \mu &= I/I_0 & I &= \bar{p} \bar{\tau} \\ \bar{p}_0 &= \frac{\alpha_1^2 J_1(\alpha_1)}{2[1 - J_1^2(\alpha_1)]^{1/2}} \frac{\sigma_0 h}{a} \epsilon_f^{1/2} & I_0 &= \frac{\alpha_1 J_1(\alpha_1)}{[1 - J_1^2(\alpha_1)]^{1/2}} \frac{\sigma_0 h}{c} \epsilon_f^{1/2} \end{aligned} \quad (\text{A.57})$$

For a rectangular pulse with the lowest pressure \bar{q}_0 , the pressure ratio is $\lambda = 1$ and the corresponding impulse ratio, according to (A.56), is given by $\sin \mu = 1$, that is, $\mu = \pi/2$; the impulse for the pulse with the lowest pressure is $i = (\pi/2)i_0$.

As an example, consider a membrane of radius $a = 2.54$ cm and thickness $h = 0.318$ cm, so that $a/h = 8$, and a yield stress of $\sigma_0 = 612$ MPa (90,000 psi). The lowest pressure and the ideal impulse values are given by (A.57) as

$$\bar{p}_0 = 135 \sqrt{\epsilon_f} \quad \text{and} \quad I_0 = 0.101 \sqrt{\epsilon_f}$$

which, for a failure strain of $\epsilon_f = 0.1$, result in $\bar{p}_0 = 42.6$ MPa (6260 psi) and $I_0 = 0.032$ bar-s.

The lowest pressure pulse has a duration of $\bar{\tau} = (a/c)\bar{\tau} = (a/c)(\pi/\alpha) = 118 \mu\text{s}$ and an impulse of $I = 0.050$ bar-s.

PULSES OF A CERTAIN CLASS

With the objective of deriving a PI relationship for general pulses, we establish the methodology by confining our attention to pulses that are probably among the least complex class of pulses. This class

consists of pulses that can be represented reasonably well by variations about a rectangular pulse, as shown schematically in Figure A-2. For this case, the pressure is

$$p(t) = \bar{p} + \tilde{p}(t) \quad (\text{A.58})$$

in which \bar{p} is the average pressure

$$\bar{p} = \frac{1}{\bar{t}} \int_0^{\bar{t}} p(t) dt \quad (\text{A.59})$$

and $\tilde{p} = p - \bar{p}$ is the departure from the average pressure.

We assume once again that the pulse does not allow the membrane to come to rest until the entire pulse has been applied. We also assume that the deflection and resulting strains are adequately approximated by the fundamental mode. With these assumptions (A.35) and (A.36) give

$$\alpha_1 y_1(\tau) = C_1 \sin \alpha_1 \tau - S_1 \cos \alpha_1 \tau \quad (\text{A.60})$$

$$\dot{y}_1(\tau) = C_1 \cos \alpha_1 \tau + S_1 \sin \alpha_1 \tau \quad (\text{A.61})$$

in which

$$C_1 = \int_0^{\bar{\tau}} q_1(\tau) \cos \alpha_1 \tau d\tau \quad S_1 = \int_0^{\bar{\tau}} q_1(\tau) \sin \alpha_1 \tau d\tau \quad (\text{A.62})$$

In (A.62), $q_1(\tau)$ is the coefficient of the first mode in the expansion (A.29). We represent its general temporal form by a Fourier series. Let

$$q(\tau) = \bar{q} + \tilde{q}(\tau) \quad q_1(\tau) = \frac{2}{\alpha_1 J_1(\alpha_1)} [\bar{q} + \tilde{q}(\tau)] \quad (\text{A.63})$$

which is consistent with (A.58), and substitute in the integrals of (A.62). Then

$$C_1 = \bar{C} + \tilde{C} \quad S_1 = \bar{S} + \tilde{S} \quad (\text{A.64})$$

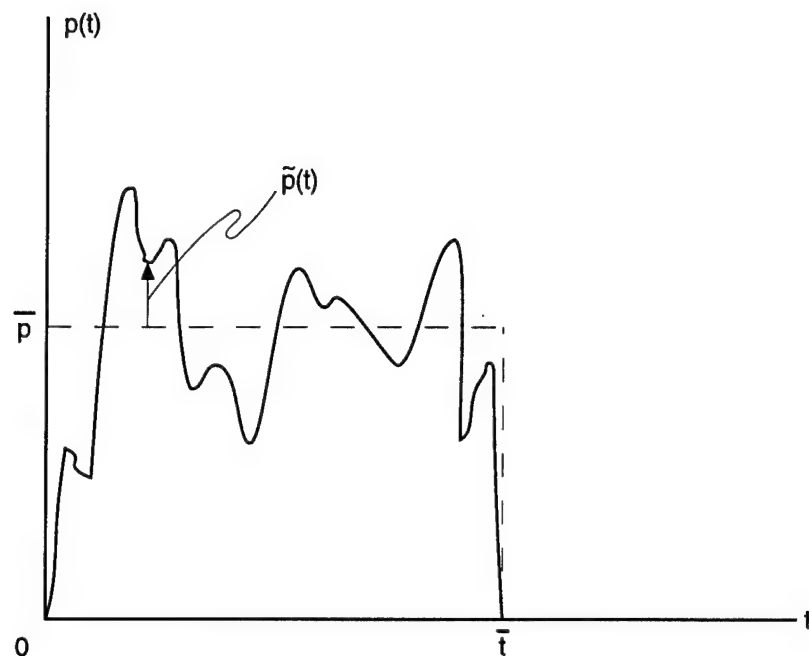


Figure A-2. Pulse example.

where

$$\bar{C} = \frac{2\bar{q}}{\alpha_1 J_1(\alpha_1)} \frac{\sin \alpha_1 \bar{\tau}}{\alpha_1} \quad \bar{S} = \frac{2\bar{q}}{\alpha_1 J_1(\alpha_1)} \frac{1 - \cos \alpha_1 \bar{\tau}}{\alpha_1} \quad (\text{A.65})$$

$$\tilde{C} = \frac{2}{\alpha_1 J_1(\alpha_1)} \int_0^{\bar{\tau}} \tilde{q}(\tau) \cos \alpha_1 \tau d\tau \quad \tilde{S} = \frac{2}{\alpha_1 J_1(\alpha_1)} \int_0^{\bar{\tau}} \tilde{q}(\tau) \sin \alpha_1 \tau d\tau \quad (\text{A.66})$$

According to (A.61), motion in the fundamental mode ceases at a time $\bar{\tau}$ given by

$$\tan \alpha_1 \bar{\tau} = -C_1/S_1 = -(\bar{C} + \tilde{C})/(\bar{S} + \tilde{S}) \quad (\text{A.67})$$

The duration of motion is approximately the same as that associated with the rectangular pulse of magnitude \bar{q} if the integrals \tilde{C} and \tilde{S} are much smaller than \bar{C} and \bar{S} .

Let us represent in (A.66) the variation of pressure about the mean by the variable

$$\tilde{r}(\tau) = \tilde{q}(\tau)/\bar{q} \quad (\text{A.68})$$

so that \tilde{C} and \tilde{S} become

$$\tilde{C} = \frac{2\bar{q}}{\alpha_1 J_1(\alpha_1)} \int_0^{\bar{\tau}} \tilde{r}(\tau) \cos \alpha_1 \tau d\tau \quad \tilde{S} = \frac{2\bar{q}}{\alpha_1 J_1(\alpha_1)} \int_0^{\bar{\tau}} \tilde{r}(\tau) \sin \alpha_1 \tau d\tau \quad (\text{A.69})$$

Then the criteria for taking the duration of motion as that associated with the average or rectangular pulse are

$$\int_0^{\bar{\tau}} \tilde{r}(\tau) \cos \alpha_1 \tau d\tau \ll \frac{\sin \alpha_1 \bar{\tau}}{\alpha_1} \quad \int_0^{\bar{\tau}} \tilde{r}(\tau) \sin \alpha_1 \tau d\tau \ll \frac{1 - \cos \alpha_1 \bar{\tau}}{\alpha_1} \quad (\text{A.70})$$

The inequalities (A.70) suggest that pulses with several oscillations about the mean value ($\tilde{r} = 0$) will fulfill these criteria. We also note that

$$\int_0^{\bar{\tau}} \tilde{r}(\tau) d\tau = 0 \quad (\text{A.71})$$

We, therefore, assume that the duration is given by

$$\tan \alpha_1 \bar{\tau} = -\bar{C}/\bar{S} \quad (\text{A.72})$$

With this simplification, the amplitude of the first mode, given by (A.60) is

$$\tilde{y}_1 = \frac{4\bar{q}}{\alpha_1^3 J_1(\alpha_1)} \sin \frac{\alpha_1 \bar{\tau}}{2} + \frac{1}{\alpha_1} \left[\bar{C} \cos \frac{\alpha_1 \bar{\tau}}{2} + \bar{S} \sin \frac{\alpha_1 \bar{\tau}}{2} \right] \quad (\text{A.73})$$

where \bar{C} and \bar{S} are defined by (A.69).

In addition to the class of pulses being described as those with pressure variations about a constant value, we need a description of the variation with time. This is done by introducing the variable

$$\eta = \tau/\bar{\tau} = t/\bar{t} \quad (\text{A.74})$$

and requiring that $\tilde{r} = \tilde{r}(\eta)$ be the same for all pulses. The integrals \bar{C} and \bar{S} of (A.69) become

$$\bar{C} = \frac{2\bar{q} \bar{\tau}}{\alpha_1 J_1(\alpha_1)} \int_0^1 \tilde{r}(\eta) \cos \alpha_1 \bar{\tau} \eta d\eta \quad \bar{S} = \frac{2\bar{q} \bar{\tau}}{\alpha_1 J_1(\alpha_1)} \int_0^1 \tilde{r}(\eta) \sin \alpha_1 \bar{\tau} \eta d\eta \quad (\text{A.75})$$

or

$$\bar{C} = \frac{2i}{\alpha_1 J_1(\alpha_1)} \tilde{R}_c \quad \bar{S} = \frac{2i}{\alpha_1 J_1(\alpha_1)} \tilde{R}_s \quad (\text{A.76})$$

where \tilde{R}_c and \tilde{R}_s represent the integrals in (A.75) and $i = \bar{q} \bar{\tau}$ is the impulse.

The ideal impulse causing the same central deflection \tilde{y}_1 is again given by (A.53). After replacing \tilde{y}_1 and substituting (A.76) in (A.73), we obtain

$$i_0 = \frac{2\bar{q}}{\alpha_1} \sin \frac{\alpha_1 \bar{\tau}}{2} + i \left(\tilde{R}_c \cos \frac{\alpha_1 \bar{\tau}}{2} + \tilde{R}_s \sin \frac{\alpha_1 \bar{\tau}}{2} \right) \quad (\text{A.77})$$

To complete the derivation of the pressure-impulse relationship, we assume that the effect of the pulse with the lowest pressure can be represented by a rectangular pulse of magnitude \bar{q}_0 . For this pulse, the duration of motion of the fundamental mode equals that of the pulse ($\bar{\tau} = \bar{t}$). We have already established that $\bar{q}_0 = (\alpha_1/2)i_0$ for producing the same strain ϵ_f , so the general pulse duration is $\bar{\tau} = i/\bar{q} =$

$(i/i_0)(\bar{q}_0/\bar{q})(i_0/\bar{q}_0) = (\mu/\lambda)(2/\alpha_1)$. Hence, in (A.77), we substitute $\alpha_1 \bar{\tau} = 2(\mu/\lambda)$ to obtain the PI relationship

$$\sin\omega + \omega(\tilde{R}_c \cos\omega + \tilde{R}_s \sin\omega) = \frac{1}{\lambda} \quad (\text{A.78})$$

where

$$\omega = \mu/\lambda \quad \mu = i/i_0 \quad \lambda = \bar{q}/\bar{q}_0 \quad 0 < \omega < \pi/2 \quad (\text{A.79})$$

and

$$\tilde{R}_c = \int_0^1 \tilde{r}(\eta) \cos 2\omega\eta d\eta \quad \tilde{R}_s = \int_0^1 \tilde{r}(\eta) \sin 2\omega\eta d\eta \quad (\text{A.80})$$

For a specified failure strain, \bar{q}_0 and i_0 are given by (A.50) and (A.54). Note that $\tilde{r}(\eta)$ is the same for all pulses in this class. A convenient form of representation for $\tilde{r}(\eta)$ is a Fourier series over the interval $0 \leq \eta \leq 1$, as follows

$$\tilde{r}(\eta) = \sum_{n=1}^{\infty} (a_n \cos 2\pi n\eta + b_n \sin 2\pi n\eta) \quad (\text{A.81})$$

$$a_n = 2 \int_0^1 \tilde{r}(\eta) \cos 2\pi n\eta d\eta \quad b_n = 2 \int_0^1 \tilde{r}(\eta) \sin 2\pi n\eta d\eta \quad (\text{A.82})$$

The coefficient a_0 is zero because of (A.71). Using the series (A.81) in the integrals (A.80) leads to the PI relationship

$$\left[1 - \omega^2 \sum_{n=1}^{\infty} \frac{a_n}{(n\pi)^2 - \omega^2} \right] \sin\omega = \frac{1}{\lambda} \quad 0 < \omega < \pi/2 \quad (\text{A.83})$$

The departure from the rectangular pulse is given by the series in (A.83) and, because of the decay of the form $(n\pi)^2$, we see that the higher the frequency of the variations the less the effect on the membrane response.

As an example, let $\tilde{r}(\eta) = a_1 \cos 2\pi\eta$ as shown in Figure A-3. Then, the PI relationship is

$$\left(1 - \frac{a_1 \omega^2}{\pi^2 - \omega^2}\right) \sin \omega = \frac{1}{\lambda} \quad 0 < \omega < \pi/2 \quad (\text{A.84})$$

A line of constant slope in the pressure-impulse (λ, μ) plane is $\omega = \mu/\lambda = \text{constant}$. If $\omega = \pi/4$, $\lambda = \sqrt{2}/(1 - a_1/15)$. If $a_1 = 1/2$, $\lambda = 1.03\sqrt{2} = 1.46$ and $\mu = 1.15$. A rectangular pulse has $a_1 = 0$, so $\lambda = \sqrt{2} = 1.41$ and $\mu = 1.11$. Although the variation varies between $1/2 \bar{q}$ and $3/2 \bar{q}$, the pressure and impulse required to produce a failure strain are only 3.4% and 3.6% higher, respectively, than a rectangular pulse of magnitude equal to the average pressure.

Figure A-4 shows the PI curves from (A.84) with amplitudes of the first temporal modes of $-a_1 = 0$, and $1/2$; $a_1 = 0$ represents the rectangular pulse and $a_1 = 1/2$ represents a pulse with a cosine variation with an amplitude equal to half the average pressure. The curves are close together, the largest difference being in the low pressure region, where $\omega = \pi/2$ and $\lambda = (1 - a_1/3)^{-1}$. The value $a_1 = 1/2$ gives $\lambda = 1$ and hence $\mu = \lambda\omega = (1.2)(\pi/2)$, which means that the mean pressure and impulse must be about 20% higher than the rectangular pulse values to achieve the same specified failure strain.

Figure A-5 shows a PI curve for the burst diaphragm in Chemical Submunition 2. The parameters used were $a_1 = 1/2$, $\epsilon_f = 0.1$, $\sigma_0 = 620.7 \text{ MPa}$, $d = 2.22 \text{ cm}$, $h = 0.120 \text{ cm}$, $\rho = 7.8 \text{ g/cm}^3$.

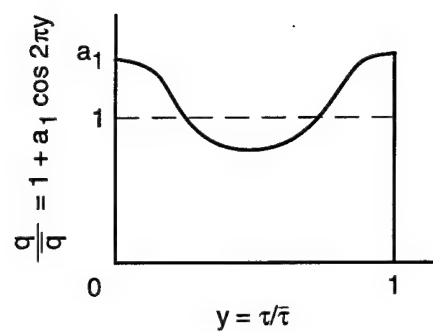


Figure A-3. Fundamental pulse variation.

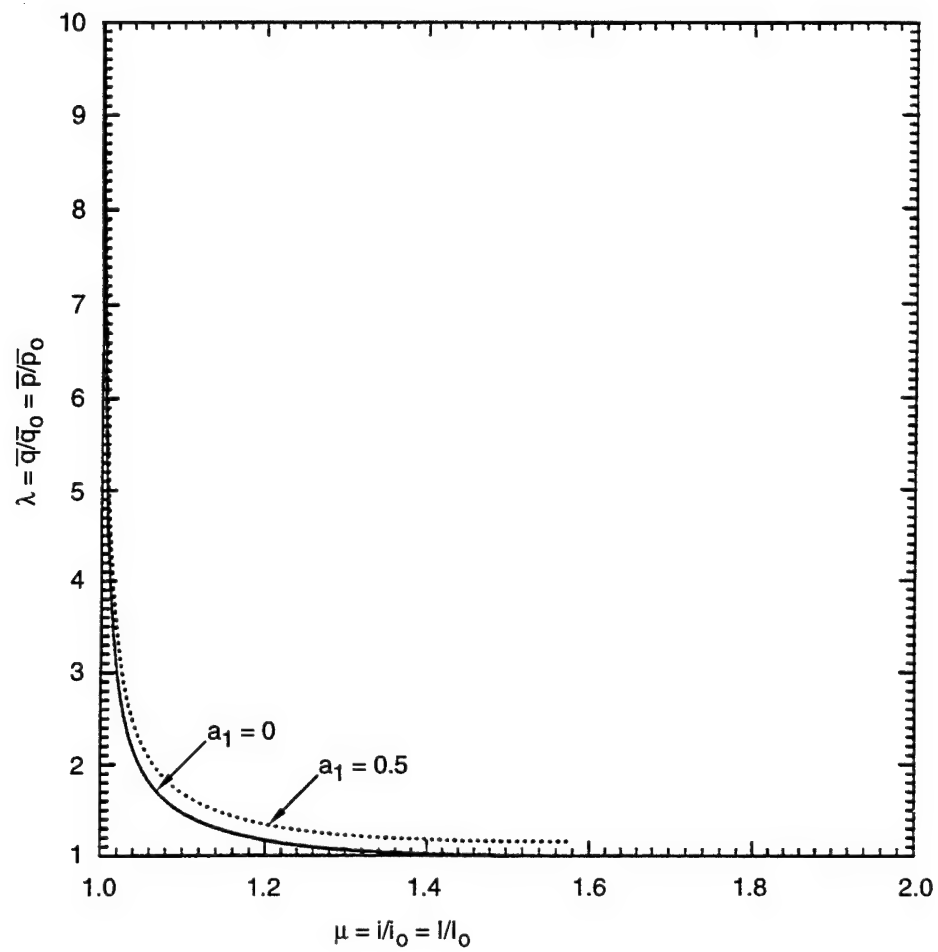
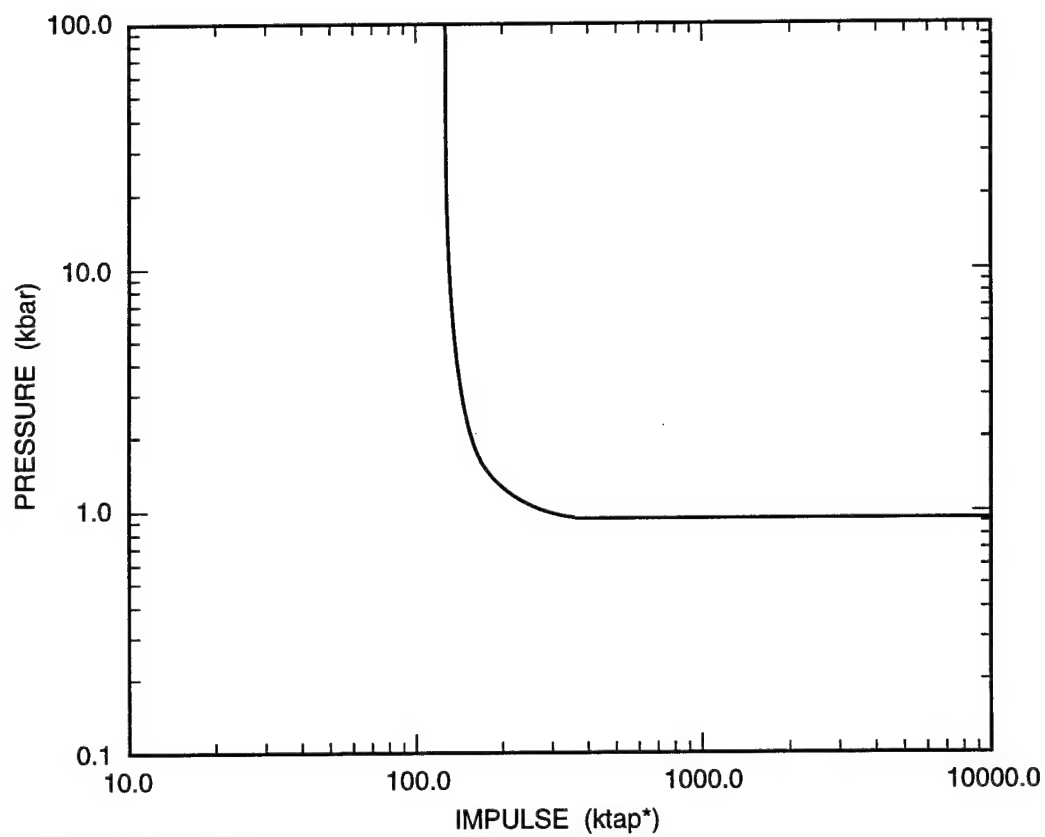


Figure A-4. Dimensionless pressure-impulse curves.



*1 tap = 1 dyne • s/cm²

Figure A-5. Pressure-impulse curve for burst diaphragm in Chemical Submunition 2.

APPENDIX B

DERIVATION OF PRESSURE-IMPULSE RELATIONSHIP FOR A LONG FLUID-FILLED CYLINDRICAL SHELL

This appendix presents details of the analysis described in Section 3.5.

DERIVATION OF GOVERNING EQUATION

Figure B-1 shows the plastic hinge mechanism with the four hinges A, B, B', and C fixed by the angle θ , initially at θ_0 . The chord lengths, ℓ_1 and ℓ_2 , are fixed in length throughout the motion. The figure also shows the forces, moments, and coordinates required to establish the kinematics and equations of motion of chords AB and BC.

The equations of translational and rotational motion of the chord AB are

$$P_b - p l_1 \sin \theta - R_y = m_1 \ddot{y}_1 \quad (B.1)$$

$$p l_1 \cos \theta + H_1 - R_x = m_1 \ddot{x} \quad (B.2)$$

$$P_b \left(x - \frac{b}{2} \right) + R_y x - (R_x + H_1) \frac{1}{2} l_1 \cos \theta - 2M = I_1 \ddot{\theta} \quad (B.3)$$

In (B.1) and (B.2), m_1 is the mass associated with chord AB. It is the mass of the arc AB. In (B.3), I_1 is the moment of inertia associated with chord AB. It is the moment of inertia of the arc AB about its center of gravity. Values of m_1 and I_1 are introduced later.

The corresponding equations of motion of chord BC are

$$p l_2 \sin \phi + R_y = m_2 \ddot{y}_2 \quad (B.4)$$

$$p l_2 \cos \phi - H_2 + R_x = m_2 \ddot{x} \quad (B.5)$$

$$R_y x + (R_x + H_2) \frac{1}{2} l_2 \cos \phi - 2M = I_2 \ddot{\phi} \quad (B.6)$$

In these equations, the mass m_2 and moment of inertia I_2 are determined from arc BC. They will be introduced later.

The kinematic relations are

$$y_1 = Y + \frac{1}{2} z_1 \quad (B.7)$$

$$y_2 = Y + z_1 + \frac{1}{2} z_2 \quad (B.8)$$

$$x = \frac{1}{2} B \quad (B.9)$$

where

$$z_1 = l_1 \cos\theta \quad z_2 = l_2 \cos\phi \quad B = l_1 \sin\theta = l_2 \sin\phi \quad (B.10)$$

In (B.7) and (B.8), Y is the displacement of the central hinge, A .

Elimination of the reactions R_x and R_y , given by (B.2) and (B.4), from (B.1) and (B.5) results in

$$m_1 \ddot{y}_1 + m_2 \ddot{y}_2 = Pb \quad (B.11)$$

$$(m_1 + m_2) \ddot{x} = H_1 - H_2 + pD \quad (B.12)$$

where

$$D = z_1 + z_2 \quad (B.13)$$

Equations (B.11) and (B.12) could have been written down immediately by considering the translational components of the whole system. Equations (B.3) and (B.6) governing rotation become

$$m_1 \ddot{x} \frac{z_1}{2} + m_2 \ddot{y}_2 x - I_1 \ddot{\theta} = -Pb \left(x - \frac{b}{2} \right) + \frac{1}{2} p l_1^2 + H_1 z_1 + 2M \quad (B.14)$$

$$m_1 \ddot{x} \frac{z_2}{2} - m_2 \ddot{y}_2 x + I_2 \ddot{\phi} = \frac{1}{2} p l_2 (z_1 z_2 - B^2) + (H_1 + H_2) \frac{z_2}{2} - 2M \quad (B.15)$$

After eliminating the horizontal reactions H_1 and H_2 among (B.12), (B.14), and (B.15), we obtain

$$\begin{aligned} (m_1 + m_2) \ddot{x} \frac{z_1 z_2}{2} - m_2 \ddot{y}_2 \frac{BD}{2} + I_1 \ddot{\theta} z_2 + I_2 \ddot{\phi} z_1 = \\ Pb \left(x - \frac{b}{2} \right) z_2 - \frac{1}{2} p_1 D (B^2 - z_1 z_2) - 2MD \end{aligned} \quad (B.16)$$

At this stage, we have (B.11) and (B.16) for θ and Y , after expressing all accelerations in terms of θ . From differentiation of (B.7), (B.8), (B.9), and (B.10), we have

$$\begin{aligned}\ddot{x} &= -\frac{B}{2} \dot{\theta}^2 + \frac{z_1}{2} \ddot{\theta} \\ \ddot{y}_1 &= \ddot{Y} - \frac{z_1}{2} \dot{\theta}^2 - \frac{B}{2} \ddot{\theta} \\ \ddot{y}_2 &= \ddot{Y} - z_1 \dot{\theta}^2 - B \ddot{\theta} - \frac{z_2}{2} \dot{\phi}^2 - \frac{B}{2} \ddot{\phi} \\ \dot{\phi} &= \frac{z_1 \dot{\theta}}{z_2} \\ \ddot{\phi} &= \frac{1}{z_2} \left[- \left(1 - \frac{z_1^2}{z_2^2} \right) B \dot{\theta}^2 + z_1 \ddot{\theta} \right]\end{aligned}\tag{B.17}$$

Substitution of (B.17) in (B.11) and (B.16) and elimination of Y yields

$$\begin{aligned}& \left[\frac{m_1 m_2}{m_1 + m_2} \left(1 + \frac{z_1}{z_2} \right) B^2 D + (m_1 + m_2) z_1^2 z_2 + 4I_1 z_2 + 4I_2 \frac{z_1^2}{z_2} \right] \frac{d\omega^2}{d\theta} \\ & - 2B \left\{ \frac{m_1 m_2}{m_1 + m_2} \left(1 + \frac{z_1}{z_2} \right) D \left[\left(1 - \frac{z_1}{z_2} \right) \frac{B^2}{z_2} - z_1 \right] + (m_1 + m_2) z_1 z_2 + 4 \left(1 - \frac{z_1^2}{z_2^2} \right) \frac{z_1}{z_2} I_2 \right\} \\ & \omega^2 \\ & = 4 \left[\frac{m_2}{m_1 + m_2} B D + (B - b) z_2 \right] P b - 4p D (B^2 - z_1 z_2) - 16MD\end{aligned}\tag{B.18}$$

where $\omega = \dot{\theta}$ is the angular velocity of AB. In (B.18), the coefficients are functions of θ . Initially, ($\theta = \theta_0$) the chords AB and BC are perpendicular, which means that initially $B^2 = z_1 z_2$, and so the coefficient of the fluid pressure is initially zero. Also, the initial value of D is the diameter of the cylinder. We require the mechanism to cease rotation when the three hinges under the load are collinear, that is, when

$\theta = \pi/2$. At this final angle, we have $z_1 = 0$, $z_2 = (l_2^2 - l_1^2)^{1/2}$, $B = l_1$, and $D = z_2$ in the coefficients.

The mass and moment of inertia expressions required in (B.18) are obtained from the arcs AB and BC in the form

$$m_1 = ma (\pi - 2\theta_0) \qquad m_2 = ma (2\theta_0) \qquad m = ph$$

$$I_1 = ma^3 2 \left[(\pi/2) - \theta_o - \frac{\cos^2 \theta_o}{(\pi/2) - \theta_o} \right] \quad I_2 = ma^3 \left[\theta_o - \frac{\sin^2 \theta_o}{\theta_o} \right] \quad (B.19)$$

where ρ is the density of the shell material, h is the wall thickness, and a is the radius of the shell.

SOLUTION OF GOVERNING EQUATION

Equation (B.18) is of the form

$$\frac{dy}{d\alpha} - A(\alpha)y = B(\alpha)P^1 - C(\alpha)p^1 - D(\alpha)M^1 \quad (B.20)$$

where

$$\begin{aligned} y &= \omega^2 & \alpha &= \theta - \theta_o & \max \alpha &= \bar{\alpha} = \frac{\pi}{2} - \theta_o & (0 < \alpha < \bar{\alpha}) \\ P^1 &= P/m & p^1 &= p/m & M^1 &= M/m \end{aligned} \quad (B.21)$$

The coefficients A , B , C , and D are all positive for α in the range $0 < \alpha < \bar{\alpha}$. To obtain a tractable solution, we approximate the coefficient by forms that are linear in the variable α , that is, we let

$$A(\alpha) = A_0 + A^1\alpha \quad B(\alpha) = B_0 + B^1\alpha \quad C(\alpha) = C^1\alpha \quad D(\alpha) = D_0 + D^1\alpha$$

where

$$A^1 = (A_1 - A_0)/\bar{\alpha} \quad B^1 = (B_1 - B_0)/\bar{\alpha} \quad C^1 = (C_1 - C_0)/\bar{\alpha} \quad D^1 = (D_1 - D_0)/\bar{\alpha} \quad (B.22)$$

In (B.22), the subscript zero indicates the initial value of the coefficient (value at $\alpha = 0$), while the subscript unity indicates the final value of the coefficient (value at $\alpha = \bar{\alpha}$). We have noted that $C_0 = 0$. To derive a solution as a convenient formula, we keep the fluid pressure at the constant value, which gives the same resistive work done on the deforming mechanism. This value is half the fluid pressure that exists at the end of the rotational motion, that is,

$$p = \frac{1}{2} \bar{p} = \frac{1}{2} K \frac{\frac{1}{2} l_1 [l_2 - (l_2^2 - l_1^2)^{1/2}]}{\pi a^2} \quad (B.23)$$

where K is the fluid bulk modulus.

An approximate solution of (B.20) satisfying the initial condition of $y(0) = 0$ (zero initial velocity) is

$$y = y_1\alpha + y_2\alpha^2 \quad (B.24)$$

where

$$y_1 = B_0 P^1 - D_0 M^1 \quad (B.25)$$

$$2y_2 = (A_0 B_0 + B^1) P^1 - (A_0 D_0 + D^1) M^1 - \frac{1}{2} C^1 \bar{p}^1 \quad (B.26)$$

The solution (B.24) applies while the external loading pressure P is acting. Let the pulse duration be T and let the rotation of the chord AB at this time be $\tilde{\alpha}$. Then, noting that

$$y^{1/2} = \omega = d\theta/dt = d\alpha/dt$$

we obtain the value of $\tilde{\alpha}$ by integrating (B.24). The integral is

$$T = \int_0^{\tilde{\alpha}} \frac{d\alpha}{\alpha^{1/2} (y_1 + y_2 \alpha)^{1/2}} \quad (B.27)$$

which provides two results depending on whether y_2 is positive or negative. Before supplying these results, let us examine ranges of the applied pressure, P .

For the plastic hinge mechanism to be activated, the right hand side of (B.20) must be positive. Initially, we have $\alpha = 0$, so activation required $B_0 P - D_0 M > 0$. This result gives the classical static collapse load

$$P_s = D_0 M / B_0 \quad (B.28)$$

However, because of the combined effect on the motion of the increasing fluid pressure (represented by the coefficient C) and the geometry changes, this collapse load will not cause rotation. Instead of (B.28), we define the static collapse pressure as the pressure required to just achieve the rotation $\bar{\alpha}$ (hinges collinear). This pressure acts throughout the motion and the rotation ceases when $\alpha = \bar{\alpha}$ ($\theta = \pi/2$). To find this pressure, set $y(\bar{\alpha}) = 0$ in the solution (B.24) to give

$$y_1 + y_2 \bar{\alpha} = 0 \quad (B.29)$$

as the equation for P_s , which we call \bar{P}_s to avoid confusion with (B.28). In view of the formulas (B.25) and (B.26), (B.29) gives

$$\left[B_0 + \frac{\bar{\alpha}}{2} (A_0 B_0 + B^1) \right] \bar{P}_s = \left[\frac{\bar{\alpha}}{2} (A_0 D_0 + D^1) + D_0 \right] \frac{B_0}{D_0} P_s + \frac{\bar{\alpha}}{4} C^1 \bar{p} \quad (B.30)$$

as an explicit formula for \bar{P}_s .

In the integral (B.27), we have $y_1 > 0$ and

$$y_2 \geq 0 \quad \text{for} \quad P \geq \bar{P}_s + \frac{2B_0(\bar{P}_s - P_s)}{\bar{\alpha}(A_0B_0 + B^1)} \quad (\text{B.31})$$

from (B.25), (B.26), and (B.29). Hence we have the two results

$$T = \frac{2}{y_1^{1/2}} \ln \left[(z\bar{\alpha})^{1/2} + (1 + z\bar{\alpha})^{1/2} \right] \quad y_2 > 0 \quad (\text{B.32})$$

$$T = \frac{2}{(-y_2)^{1/2}} \tan^{-1} \left[\frac{-z\bar{\alpha}}{1 + z\bar{\alpha}} \right]^{1/2} \quad y_2 < 0 \quad (\text{B.33})$$

In (B.32) and (B.33), $z = y_2/y_1$. The angular velocity at time T is

$$\bar{\omega}^2 = y_1\bar{\alpha} + y_2\bar{\alpha}^2 \quad (\text{B.34})$$

After the load has been applied, the governing equation is (B.20) with $P^1 = 0$. For convenience only, let $\alpha = \bar{\alpha} + \beta$. Then the governing equation becomes

$$\frac{dy}{d\beta} - [(A_0 + A^1\bar{\alpha}) + A^1\beta] y = -[(D_0 + D^1\bar{\alpha}) M^1 + \frac{1}{2} C^1\bar{p}^1\bar{\alpha}] - (D^1M^1 + \frac{1}{2} C^1\bar{p}^1)\beta \quad (\text{B.35})$$

and the initial condition is

$$y(0) = \bar{\omega}^2 \quad (\text{B.36})$$

An approximate solution is

$$y = \bar{\omega}^2 + \tilde{y}_1\beta + \tilde{y}_2\beta^2 \quad (\text{B.37})$$

where

$$\tilde{y}_1 = (A_0 + A^1\bar{\alpha}) \bar{\omega}^2 - \left[(D_0 + D^1\bar{\alpha}) M^1 + \frac{1}{2} C^1\bar{p}^1\bar{\alpha} \right] \quad (\text{B.38})$$

$$2\tilde{y}_2 = (A_0 + A^1\tilde{\alpha}) \left\{ (A_0 + A^1\tilde{\alpha}) - \left[(D_0 + D^1\tilde{\alpha}) M^1 + \frac{1}{2} C^1 \bar{p}^1 \tilde{\alpha} \right] \right\} \\ + A^1 \tilde{\omega}^2 - \left(D^1 M^1 + \frac{1}{2} C^1 \bar{p}^1 \right) \quad (B.39)$$

We want the angular velocity to be zero when $\theta = \pi/2$, $\alpha = \bar{\alpha} = (\pi/2) - \theta_0$ or $\beta = \bar{\beta} = \bar{\alpha} - \tilde{\alpha}$. This condition is obtained from the solution (B.37) in the form

$$\tilde{\omega}^2 + \tilde{y}_1 \bar{\beta} + \tilde{y}_2 \bar{\beta}^2 = 0 \quad (B.40)$$

Substitution in (B.40) of the expressions (B.38) and (B.39) leads to

$$\left\{ 1 + (A_0 + A^1\tilde{\alpha})\bar{\beta} + \frac{1}{2} [(A_0 + A^1\tilde{\alpha})^2 + A^1] \bar{\beta}^2 \right\} m\tilde{\omega}^2 \\ = \left[1 + \frac{1}{2} (A_0 + A^1\tilde{\alpha})\bar{\beta} \right] \left[(D_0 + D^1\tilde{\alpha}) \frac{B_0}{D_0} P_s + \frac{1}{2} C^1 \tilde{\alpha} \bar{p} \right] \bar{\beta} + \frac{1}{2} \left[D^1 \frac{B_0}{D_0} P_s + \frac{1}{2} C^1 \bar{p} \right] \bar{\beta}^2 \quad (B.41)$$

where $m\tilde{\omega}^2$ is given by (B.34). Equation (B.34) with y_1 and y_2 given by (B.25) and (B.26) is

$$m\tilde{\omega}^2 = \left[B_0 + \frac{1}{2} (A_0 B_0 + B^1) \tilde{\alpha} \right] \tilde{\alpha} P - \left[B_0 + \frac{1}{2} (A_0 D_0 + D^1) \frac{B_0}{D_0} \tilde{\alpha} \right] \tilde{\alpha} P_s - \frac{1}{4} C^1 \tilde{\alpha}^2 \bar{p} \quad (B.42)$$

so (B.41) and (B.42) determine P explicitly for each choice of the rotation angle $\tilde{\alpha}$ in the range $0 < \tilde{\alpha} < \bar{p}$. The resulting value of P is compared with (B.31) to see if $y_2 > 0$ or $y_2 < 0$ in order to select the appropriate pulse duration formula, (B.32) or (B.33).

PRESSURE-IMPULSE RELATIONSHIP

The impulse of a rectangular pulse is simply $I = PT$. Hence, (B.32) and (B.33) give

$$I = \frac{2m^{1/2}P}{(my_2)^{1/2}} \ln \left[(z\tilde{\alpha})^{1/2} + (1 + z\tilde{\alpha})^{1/2} \right] \quad y_2 > 0 \quad (B.43)$$

$$I = \frac{2m^{1/2}P}{(-my_2)^{1/2}} \tan^{-1} \left[\frac{-z\tilde{\alpha}}{1 + z\tilde{\alpha}} \right]^{1/2} \quad y_2 < 0 \quad (B.44)$$

The angle $\tilde{\alpha}$ can be regarded as a parameter. After eliminating $m\tilde{\omega}^2$ between (B.41) and (B.42) we obtain $P = P(\tilde{\alpha})$ and hence, according to (B.25) and (B.26), we have $y_1(\tilde{\alpha})$ and $y_2(\tilde{\alpha})$, giving $z = z(\tilde{\alpha})$. Again, the inequality (B.31) determines the choice of (B.43) or (B.44) for the impulse.

If we consider a sequence of pulses in which $P \rightarrow \infty$ and $T \rightarrow 0$ in such a way that $I = PT$ decreases but $I \rightarrow I_0$, an ideal impulse, we can determine the value of I_0 from (B.43). Because z tends to a constant and $\tilde{\alpha} \rightarrow 0$, the limiting process gives

$$I_0 \sim \frac{2P}{y_1^{1/2}} (z\tilde{\alpha})^{1/2} \sim \frac{2P\tilde{\alpha}^{1/2}}{y_1^{1/2}} \sim \frac{2P_0\tilde{\omega}}{y_1} \sim \frac{2m^{1/2}}{B_0} (m\tilde{\omega}^2)^{1/2} \quad (\text{B.45})$$

where $m\tilde{\omega}^2$ is (B.41) with $\tilde{\alpha} = 0$ ($\bar{\beta} = \bar{\alpha}$), that is,

$$\left[1 + A_0\bar{\alpha} + \frac{1}{2} (A_0^2 + A^1) \bar{\alpha}^2 \right] m\tilde{\omega}^2 \sim \left[\left(1 + \frac{1}{2} A_0\bar{\alpha} \right) D_0 + \frac{1}{2} D^1\bar{\alpha} \right] \bar{\alpha} \frac{B_0}{D_0} P_s + \frac{1}{4} C^1 \bar{\alpha}^2 \quad (\text{B.46})$$

SUBMUNITION RESPONSE

The mass and moments of inertia representing the arcs are

Chord AB masubmunition	$m_1 = a (\pi - 2\theta_0)m$	2.4936 m (cm)
Chord BC masubmunition	$m_2 = a (2\theta_0)m$	6.4835 m (cm)
Chord AB inertia	$I_1 = 2a^3 \left(\varphi_0 - \frac{\sin^2 \varphi_0}{\varphi_0} \right)$	1.2585 m (cm ³)
Chord BC inertia	$I_2 = 2a^3 \left(\theta_0 - \frac{\sin^2 \theta_0}{\theta_0} \right)$	19.1565 m (cm ³)

The final values of the geometrical quantities are

$$\begin{aligned} \bar{\theta} &= \pi/2 & \bar{\varphi} &= \sin^{-1} (l_1/l_2) = 27.8^\circ & \bar{\psi} &= \sin^{-1} (l_1/a) = 57.7^\circ \\ \bar{z}_1 &= 0 & \bar{z}_2 &= l_2 \cos \bar{\varphi} = 4.5817 \text{ cm} & \bar{D} &= \bar{z}_2 = 4.5817 \text{ cm} \\ \bar{B} &= l_1 = l_2 \sin \bar{\varphi} = 2.4156 \text{ cm} \end{aligned}$$

The initial values of the coefficients in (B.18) are

Coefficient of $\frac{d\omega^2}{d\theta}$	144.58 m	(cm ⁴)
Coefficient of ω^2	-245.58 m	(cm ⁴)
Coefficient of P	79.38	cm ³
Coefficient of p	0	
Coefficient of M	- 91.44	cm

where m is expressed in grams per square centimeter. (P and p in dynes/cm², M in dyne-cm per centimeter, ω in radians per second).

The final values of the coefficients in (B.18) are

Coefficient of $\frac{d\omega^2}{d\theta}$	71.34 m	(cm ⁴)
Coefficient of ω^2	- 50.77 m	(cm ⁴)
Coefficient of P	79.18	cm ³
Coefficient of p	- 106.90	cm ³
Coefficient of M	- 73.31	cm

The initial and final values of the coefficients in (B.18) give the following values for the coefficients in (B.20):

$$\begin{array}{llll} A_0 = 1.70 & A^1 = - 2.25 & B_0 = 0.55 \text{ cm}^{-1} & B^1 = 1.28 \text{ cm}^{-1} \\ C_0 = 0 & C^1 = 3.44 \text{ cm}^{-1} & D_0 = 0.63 \text{ cm}^{-3} & D^1 = 0.92 \text{ cm}^{-3} \end{array}$$

and the final value of α is $\bar{\alpha} = (\pi/2) - \theta_0 = 0.4363$.

The plastic hinge moment is

$$M = \sigma_y h^2 / 4 = 0.69 \times 10^9 \text{ dyne-cm/cm} \quad (69 \text{ MPa-cm}^2)$$

so the static collapse pressure that triggers the mechanism is

$$P_s = (D_0/B_0)M = 79 \text{ MPa}$$

The values of y_1 and y_2 given by (B.25) and (B.26) are

$$my_1 = 0.55 (P - P_s)$$

$$my_2 = 1.11 P - 1.15 P_s - 0.86 \bar{p}$$

in which the maximum fluid pressure, according to (B.23), is

$$\bar{p} = 63 \text{ MPa}$$

For the choice of integral, (B.32) or (B.33), we have

$$y_2 < 0 \quad 79 \text{ MPa} < P < 111 \text{ MPa}$$

$$y_2 > 0 \quad P > 111 \text{ MPa}$$

The lowest pressure that achieves the rotation $\theta = \pi/2$ ($\alpha = \bar{\alpha}$) given by $y_1 + \bar{\alpha}y_2 = 0$, (or $z = y_2/y_1 = -1/\bar{\alpha} = -2.29$), is

$$\bar{P}_s = 94 \text{ MPa}$$

This value is one of the asymptotes in the PI diagram. The other asymptote given by (B.45) and (B.46) is

$$I_0 = 124 \text{ ktaps (0.124 bar}\cdot\text{s) (1.24 MPa}\cdot\text{s)}$$

Figure B-2 shows the PI diagram for this example. It is the relationship between the pressure and impulse for all rectangular pulses applied to a strip of a specific cylindrical submunition, when the pulses cause the same maximum pressure in the contained fluid.

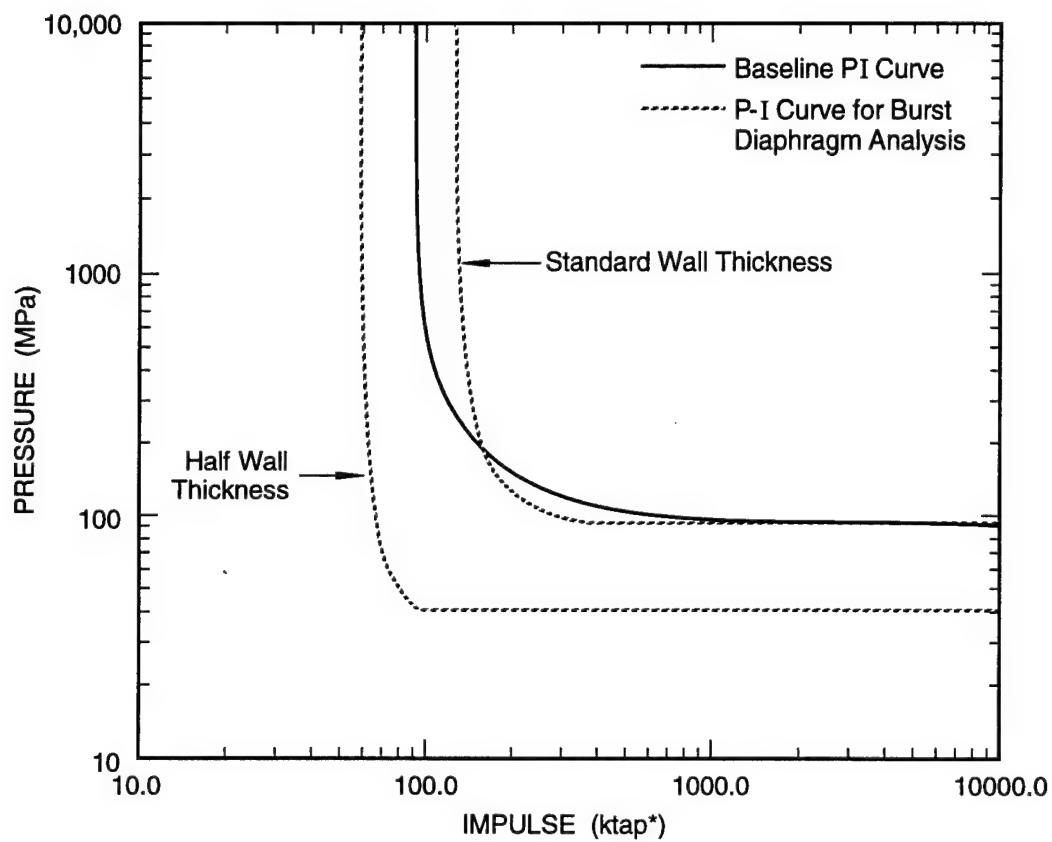
LOAD LENGTH EFFECT

When the cylinder is loaded on a part of its length, the fluid pressure that has to be generated in the foregoing analysis for a plane strain state must be increased to achieve the diaphragm burst pressure. To approximate the larger pressure required, we have adopted a quasi-static approach. We multiply the burst pressure \bar{p}_d by the ratio of two lengths, consisting of the loaded length plus the length between the loading and the diaphragm divided by the loaded length. If the loaded length is H and the unloaded length above the diaphragm is H_d , the new plane strain pressure required is

$$\bar{p} = \frac{H + H_d}{H} \bar{p}_d \quad (\text{B.47})$$

Essentially, we have a plane strain fluid with a lower bulk modulus equal to

$$K_d = \frac{H}{H + H_d} K \quad (\text{B.48})$$



*1 tap = 1 dyne • s/cm²

Figure B-2. Comparison of the PI curves calculated for the analytical model of burst diaphragm failure and the baseline PI curve for Chemical Submunition 2.

To obtain the higher pressure \bar{p} of (B.47), we need a larger fluid volumetric strain, ϵ_d , given by

$$\epsilon_d = \frac{H + H_d}{H} \epsilon \quad (\text{B.49})$$

If we keep the condition that the three plastic hinges are collinear when the maximum fluid pressure is reached, the requirement of an increased volumetric strain introduces a small change in the stationary hinge locations. These new locations are determined by

$$\epsilon_d = L_1 [L_2 - (L_2^2 - L_1^2)^{1/2}] / 2\pi a^2 = [(H + H_d)/H] \epsilon \quad d^2 = L_1^2 + L_2^2 = l_1^2 + l_2^2 \quad (\text{B.50})$$

where L_1 and L_2 are the new lengths of the chords AB and B, as shown in Figure B-1.

MODIFIED SUBMUNITION RESPONSE

Let us consider the previous example of a submunition loaded over its entire length when the loaded length is reduced according to

$$\frac{H}{H + H_d} = \frac{1}{2}$$

Equation (B.50) and geometrical relationships lead to

Chord AB angle	θ_0	59°	
Chord BC angle	ϕ_0	31°	
Subtended angle	ψ_0	62°	
Chord AB length	L_1	2.94 cm	
Chord BC length	L_2	4.90 cm	
Chord AB height	z_1	1.51 cm	
Chord BC height	z_2	4.20 cm	
Combined heights	$D = d$	5.71 cm	
Breadth of chords	B	2.52 cm	
Chord AB mass	m_1	3.09 m	(cm)
Chord BC mass	m_2	5.89 m	(cm)
Chord AB inertia	I_1	2.37 m	(cm ³)
Chord BC inertia	I_2	14.78 m	(cm ³)
Final AB angle	$\bar{\theta}$	$\pi/2$	
Final BC angle	$\bar{\phi}$	36.9°	
Final AB height	\bar{z}_1	0	
Final BC height	\bar{z}_2	3.92 m	

Final combined height	$D = \bar{z}_2$	3.92 m
Final breadth	$\bar{B} = L_1$	2.94 m

The initial values of the coefficients in (B.18) are

$d\omega^2/d\theta$	257.7 m	(cm ⁴)
ω^2	- 337.2 m	(cm ⁴)
P	93.0	cm ³
p	0	
M	- 91.4	cm

and the final values are

$d\omega^2/d\theta$	300.2 m	(cm ⁴)
ω^2	- 103.0 m	(cm ⁴)
P	89.9	cm ³
p	- 135.5	cm ³
M	- 62.7	cm

The coefficients in (B.20) are

$A_0 = 1.13$	$A^1 = - 1.79$	$B_0 = 0.36 \text{ cm}^{-1}$	$B^1 = - 0.11 \text{ cm}^{-1}$
$C_0 = 0$	$C^1 = 0.83 \text{ cm}^{-1}$	$D_0 = 0.35 \text{ cm}^{-3}$	$D^1 = - 0.26 \text{ cm}^{-3}$

and the final value of α is $\bar{\alpha} = 0.541$ radius.

The pressure that triggers the mechanism is

$$P_s = \left(\frac{D_0}{B_0} \right) M_0 = 67 \text{ MPa}$$

The maximum fluid pressure is $\bar{p} = 126 \text{ MPa}$, and the pressure applied throughout the motion required to generate the fluid pressure is

$$\bar{P}_s = 93 \text{ MPa}$$

For the choice of integral, (B.32) or (B.33), we obtain

$y_2 < 0$	$93 \text{ MPa} < P < 210 \text{ MPa}$
$y_2 > 0$	$P > 210 \text{ MPa}$

and the ideal impulse required to produce a fluid pressure of $\bar{p} = 126 \text{ MPa}$ when motion ceases is

$$I_0 = 149 \text{ ktaps (1.49 MPa}\cdot\text{s)}$$

Figure B-3 shows the PI relationship for this example as a dashed curve; the full line curve is the relationship when the submunition is loaded over its entire length (same curve as that in Figure B-2). At high pressure, the impulse has to be increased by about 20% due to the reduced loaded length. The pressure asymptotes for both loading cases are comparable ($\bar{P}_s = 94 \text{ MPa}$).

PRESSURE-IMPULSE LOADING RELATED TO FRAGMENT IMPACT

Consider an idealized fragment consisting of a steel rectangular plate traveling at a velocity V_f along the normal to the plate surface, the normal being perpendicular to the axis of the cylindrical submunition. We treat the case in which the length of the plate equals the height of the cylinder so that impact occurs over the entire height. Let the mass per unit height of the cylinder and plate be M_c and M_f respectively. By assuming that the impact is plastic, we have the velocity of the cylinder and mass as

$$V = \frac{M_f}{M_f + M_c} V_f \quad (\text{B.51})$$

The impulse \tilde{I} per unit height is

$$\tilde{I} = M_c V = M_f (V_f - V) \quad (\text{B.52})$$

The impulse I of our PI relationship is given by

$$\tilde{I} = 2b I \quad (\text{B.53})$$

where $2b$ is the width over which impact occurs (Figure B-1). Similarly, if the contact force per unit height is \tilde{P} , we have

$$\tilde{P} = 2b P \quad (\text{B.54})$$

Let the impact time be T and the ring deflection of the plastic hinge mechanism be z_1 ; at this deflection the hinges are collinear.

We assume that the deceleration of the fragment from velocity V_f to velocity V is constant. This assumption is consistent with the concept of an average contact pressure used in the equation of motion. We now have

$$z_1 = \frac{1}{2} (V + V_f) T \quad (\text{B.55})$$

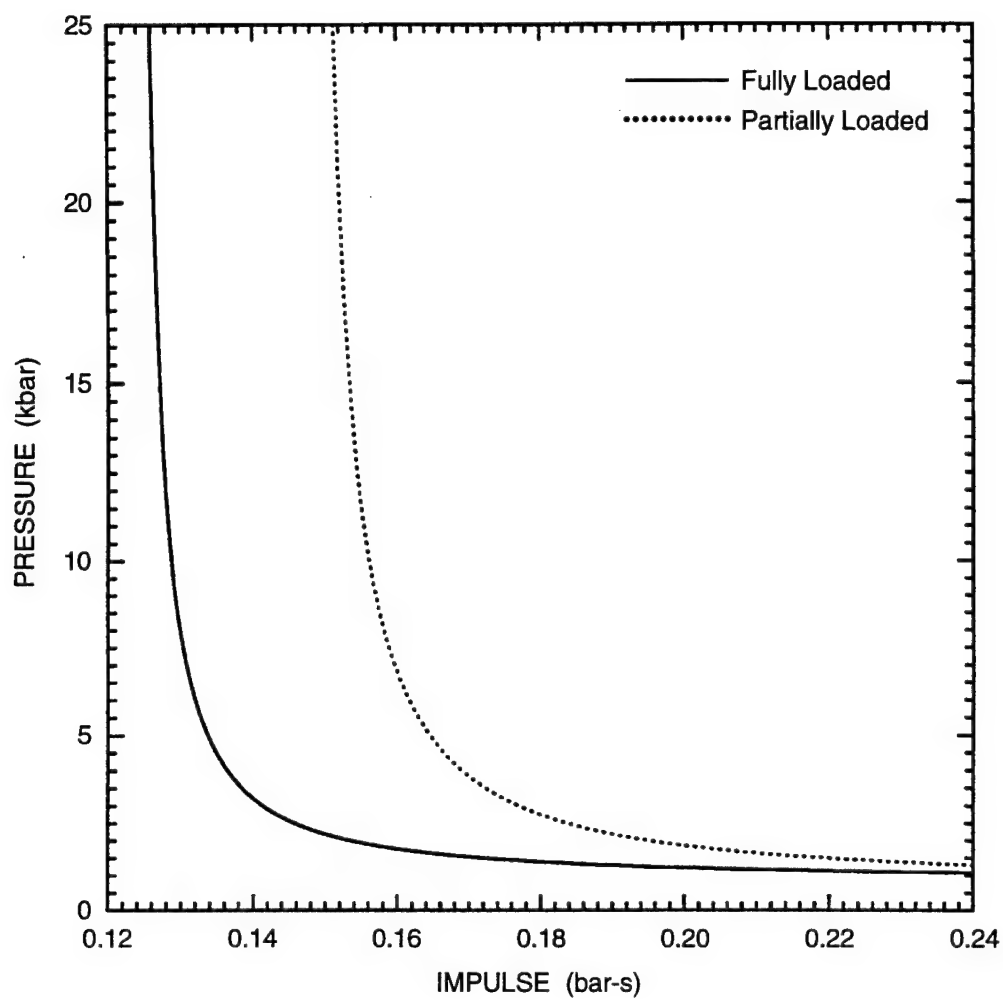


Figure B-3. Pressure-impulse relationships for a fully and partially loaded canister.

where the contact duration may be expressed as $T = \tilde{I}/\tilde{P} = I/P$.

Equations (B.51) through (B.55) can be solved for the fragment mass and velocity in the forms

$$M_f = \frac{2bI}{2 [(Pz_1/I) - (2bI/M_c)]} \quad (B.56)$$

and

$$V_f = (2Pz_1/I) - (2bI/M_c) \quad (B.57)$$

In (B.56) and (B.57),

$$M_c = \rho \, 2\pi a h + \rho_f \pi a^2$$

where ρ_f is the fluid density.

As an example, consider the submunition example presented in the "Submunition Response" section and let the fluid be water. Then

$$M_c = 114.5 \text{ g}$$

$$z_1 = 1.02 \text{ cm}$$

$$2b = 4.00 \text{ cm}$$

From Figure B-2, a PI pair is

$$P = 300 \text{ MPa}$$

$$I = 142 \text{ ktaps (1.42 MPa}\cdot\text{s)}$$

and the load duration is $T = 49 \mu\text{s}$. Equations (B.56) and (B.57) give $M_f = 18.4 \text{ g/cm}$ and $V_f = 368 \text{ m/s}$. If the height of the submunition is 15 cm, the fragment mass is 276 g.

An improvement is effected by using the value of the angle $\tilde{\alpha}$ associated with the values of P and I . The submunition deflection during the pulse time T is then $z_1 - \tilde{z}_1$, where $\tilde{z}_1 = l_1 \cos \tilde{\theta}$ with $\tilde{\theta} = (\pi/2) - \tilde{\alpha}$. In our example, we have $\tilde{z}_1 = 0.354 \text{ cm}$ to give the deflection during contact of $z_1 - \tilde{z}_1 = 0.667 \text{ cm}$. Substituting $z_1 - \tilde{z}_1$ for z_1 in (B.56) and (B.57) results in $M_f = 31.1 \text{ g/cm}$ and $V_f = 232 \text{ m/s}$. Again, for a submunition of 15 cm height, the fragment mass is 467 g. The common velocity after impact is $V = 50 \text{ m/s}$.

APPENDIX C
TABLES OF TEST RESULTS

Table C-1. Impact tests on Chemical Submunition 1.


Impact Orientation	Impactor		
	38 mm (1.5 in.) 89 mm (3.5 in.) ~1880 g	19 mm (0.75 in.) 89 mm (3.5 in.) ~940 g	9 mm (0.375 in.) 89 mm (3.5 in.) ~470 g
			
	<u>Gun 7</u> A, C, F $V = 326 \text{ m/s}$ $MV = 605 \text{ kg}\cdot\text{m/s}$ $1/2 MV^2 = 0.986 \times 10^5 \text{ kg m}^2/\text{s}^2$ Severe fracture of upper casing, fuze flattened, multiple fragments		
	<u>Gun 8</u> A, C $V = 234 \text{ m/s}$ $MV = 435 \text{ kg}\cdot\text{m/s}$ $1/2 MV^2 = 0.508 \times 10^5 \text{ kg m}^2/\text{s}^2$ Cracking of upper casing, some fragments, fuze crushed, circumferential cracking of upper weld		
	<u>Gun 9</u> A, C $V = 198 \text{ m/s}$ $MV = 366 \text{ kg}\cdot\text{m/s}$ $1/2 MV^2 = 0.363 \times 10^5 \text{ kg m}^2/\text{s}^2$ Cracking of upper case, no fragments, fuze crushed, circumferential cracking of upper weld	<u>Gun 11</u> A, C $V = 366 \text{ m/s}$ $MV = 345 \text{ kg}\cdot\text{m/s}$ $1/2 MV^2 = 0.632 \times 10^5 \text{ kg m}^2/\text{s}^2$ Severe axial fracture, large fragment removed from side	
	<u>Gun 10</u> $V = 175 \text{ m/s}$ $MV = 324 \text{ kg}\cdot\text{m/s}$ $1/2 MV^2 = 0.284 \times 10^5 \text{ kg m}^2/\text{s}^2$ Fuze crushed, very slight cracking of upper weld.		
			<u>Gun 12</u> $V = 358 \text{ m/s}$ $MV = 170 \text{ kg}\cdot\text{m/s}$ $1/2 MV^2 = 0.305 \times 10^5 \text{ kg m}^2/\text{s}^2$ Slight erosion of fuze, no cracking, impactor fragmented

Table C-1. Impact tests on Chemical Submunition 1 (Continued).

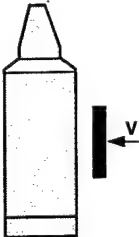
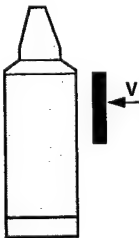
Impact Orientation	Impactor		
	38 mm (1.5 in.) 89 mm (3.5 in.) ~1880 g	19 mm (0.75 in.) 89 mm (3.5 in.) ~940 g	9 mm (0.375 in.) 89 mm (3.5 in.) ~470 g
		<p><u>Gun 14</u> F, D</p> <p>V = 336 m/s MV = 318 kg·m/s 1/2 MV² = 0.535 x 10⁵ kg m²/s²</p> <p>Severe dent under impactor, fuze separated from canister, diaphragm blown out, slight cracking of upper weld, impactor fractured</p>	
		<p><u>Gun 15</u> D</p> <p>V = 273 m/s MV = 257 kg·m/s 1/2 MV² = 0.351 x 10⁵ kg m²/s²</p> <p>Severe dent under impactor, fuze bent toward impact side, diaphragm ruptured, no fractures in canister</p>	
		<p><u>Gun 13</u></p> <p>V = 204 m/s MV = 191 kg·m/s 1/2 MV² = 0.195 x 10⁵ kg m²/s²</p> <p>Large dent in the side under impactor, fuze bent toward impact side, no fractures in canister</p>	
		<p><u>Gun 16</u> A, C, F</p> <p>V = 273 m/s MV = 257 kg·m/s 1/2 MV² = 0.351 x 10⁵ kg m²/s²</p> <p>Canister fractured into many pieces, fuze removed</p>	
		<p><u>Gun 17</u> A, C</p> <p>V = 197 m/s MV = 257 kg·m/s 1/2 MV² = 0.183 x 10⁵ kg m²/s²</p> <p>Upper body fractured, large fragment removed, axial cracking</p>	<p><u>Gun 18</u></p> <p>V = 197 m/s MV = 94 kg·m/s 1/2 MV² = 0.093 x 10⁵ kg m²/s²</p> <p>Slight deformation at impact point, fuze slightly bent towards impact direction, slight cracking of top weld</p>
			<p><u>Gun 37</u></p> <p>V = 202 m/s MV = 96 kg·m/s 1/2 MV² = 0.097 x 10⁵ kg m²/s²</p> <p>Slight deformation at impact point, no cracking</p>

Table C-1. Impact tests on Chemical Submunition 1 (Continued).

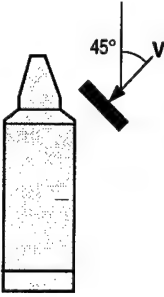
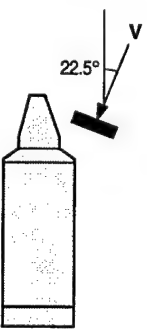
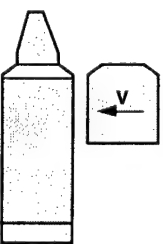
Impact Orientation	Impactor		
	38 mm (1.5 in.) 89 mm (3.5 in.) ~1880 g	19 mm (0.75 in.) 89 mm (3.5 in.) ~940 g	9 mm (0.375 in.) 89 mm (3.5 in.) ~470 g
			<p><u>Gun 19</u> C</p> <p>V = 296 m/s MV = 103 kg•m/s 1/2 MV² = 0.128 x 10⁵ kg m²/s²</p> <p>Crushing of shoulder at impact point, slight cracking of top weld</p>
			<p><u>Gun 21</u> C</p> <p>V = 343 m/s MV = 142 kg•m/s 1/2 MV² = 0.244 x 10⁵ kg m²/s²</p> <p>Crushing of shoulder at impact point, cracking of weld at impact point, some leakage through crack</p>
			<p><u>Gun 20</u> C</p> <p>V = 204 m/s MV = 102 kg•m/s 1/2 MV² = 0.126 x 10⁵ kg m²/s²</p> <p>Crushing of shoulder, cracking of weld at impact point, slight leaking at crack</p>
	<p><u>Gun 24</u></p> <p>V = 112 m/s No water</p> <p>Little damage to target, impactor fractured at top weld</p>		
	<p><u>Gun 32</u> F</p> <p>V = 113 m/s Water</p> <p>Little damage to target, fuze broken off, impactor ruptured</p>		

Table C-2. Impact tests on Chemical Submunition 2.

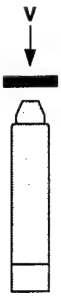
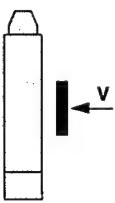
Impact Orientation	Impactor		
	24 mm (0.94 in.) 89 mm (3.5 in.) -1190 g	12 mm (0.47 in.) 89 mm (3.5 in.) -595 g	6 mm (0.24 in.) 89 mm (3.5 in.) -301 g
	<p><u>Gun 22</u></p> <p>V = 207 m/s MV = 247 kg·m/s 1/2 MV² = 0.255 x 10⁵ kg m²/s²</p> <p>Nose severely crushed, some bulging of upper body</p>		
		<p><u>Gun 28</u></p> <p>V = 334 m/s MV = 200 kg·m/s 1/2 MV² = 0.334 x 10⁵ kg m²/s²</p> <p>Nose slightly crushed, impactor fragmented</p>	
	<p><u>Gun 23</u> C, D</p> <p>V = 204 m/s MV = 243 kg·m/s 1/2 MV² = 0.248 x 10⁵ kg m²/s²</p> <p>Side severely crushed and sheared, top fractured at weld, inner tube severely bent, diaphragm ruptured</p>		
		<p><u>Gun 27</u> C, D</p> <p>V = 200 m/s MV = 119 kg·m/s 1/2 MV² = 0.119 x 10⁵ kg m²/s²</p> <p>Upper canister fractured but top not removed, diaphragm ruptured</p>	
		<p><u>Gun 40</u> D</p> <p>V = 200 m/s MV = 120 kg·m/s 1/2 MV² = 0.120 x 10⁵ kg m²/s²</p> <p>Diaphragm ruptured, upper canister intact. Welded construction</p>	<p><u>Gun 31</u> C</p> <p>V = 299 m/s MV = 92 kg·m/s 1/2 MV² = 0.138 x 10⁵ kg m²/s²</p> <p>Top broken off at weld, shock tube broken off</p>
		<p><u>Gun 45</u> D</p> <p>V = 197 m/s MV = 118 kg·m/s 1/2 MV² = 0.116 x 10⁵ kg m²/s²</p> <p>Diaphragm ruptured, 15% ullage</p>	<p><u>Gun 30</u></p> <p>V = 259 m/s MV = 78 kg·m/s 1/2 MV² = 0.101 x 10⁵ kg m²/s²</p> <p>Side dented, no fractures</p>
			<p><u>Gun 29</u></p> <p>V = 201 m/s MV = 61 kg·m/s 1/2 MV² = 0.061 x 10⁵ kg m²/s²</p> <p>Side lightly dented, no fractures</p>

Table C-2. Impact tests on Chemical Submunition 2 (Continued).

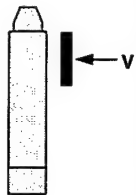
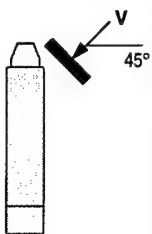
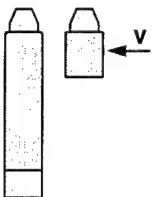
Impact Orientation	Impactor		
	89 mm (3.5 in.) 24 mm (0.94 in.) ~1190 g	89 mm (3.5 in.) 12 mm (0.47 in.) ~595 g	89 mm (3.5 in.) 6 mm (0.24 in.) ~301 g
		<p><u>Gun 25</u> C, D</p> <p>V = 200 m/s MV = 120 kg·m/s $1/2 MV^2 = 0.120 \times 10^5 \text{ kg m}^2/\text{s}^2$</p> <p>Top broken off at weld, inner tube broken off, diaphragm ruptured</p>	
		<p><u>Gun 41</u> F, D</p> <p>V = 200 m/s MV = 120 kg·m/s $1/2 MV^2 = 0.120 \times 10^5 \text{ kg m}^2/\text{s}^2$</p> <p>Fuze removed, diaphragm ruptured, welded construction</p>	
		<p><u>Gun 26</u> C</p> <p>V = 205 m/s MV = 123 kg·m/s $1/2 MV^2 = 0.126 \times 10^5 \text{ kg m}^2/\text{s}^2$</p> <p>Top broken off at weld</p>	
	<p><u>Gun 35</u> F</p> <p>V = 115 m/s MV = 185 kg·m/s $1/2 MV^2 = 0.107 \times 10^5 \text{ kg m}^2/\text{s}^2$</p> <p>Fuze removed from target, inner tube broken off</p>		

Table C-3. Impact tests on scaled Chemical Submunition 2.







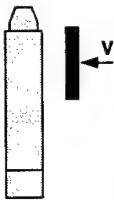
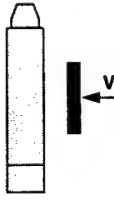
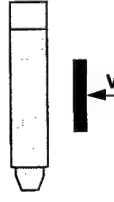

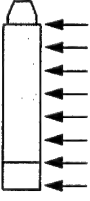
Impact Orientation	Half-scale	Quarter-scale	Quarter-scale
	6 mm  44.5 mm  73 g	3 mm  22.3 mm  9.0 g	Small Impactor 3 mm  16.3 mm  4.9 g
	Gun 53 F V = 200 m/s MV = 14.6 kg·m/s 1/2 MV ² = 0.0146 x 10 ⁵ kg m ² /s ² Fuze removed	Gun 39 D V = 198 m/s MV = 1.8 kg·m/s 1/2 MV ² = 0.0018 x 10 ⁵ kg m ² /s ² Diaphragm ruptured, fuze bent forward	Gun 34 V = 197 m/s MV = 1.0 kg·m/s 1/2 MV ² = 0.0010 x 10 ⁵ kg m ² /s ² Fuze bent forward
	Gun 46 V = 200 m/s MV = ? 1/2 MV ² = ? Glancing blow		Gun 36 D V = 260 m/s MV = 1.3 kg·m/s 1/2 MV ² = 0.0010 x 10 ⁵ kg m ² /s ² Diaphragm ruptured, fuze bent forward
	Gun 48 F, D V = 200 m/s MV = 14.5 kg·m/s 1/2 MV ² = 0.0145 x 10 ⁵ kg m ² /s ² Fuze removed, diaphragm ruptured	Gun 38 D V = 198 m/s MV = 1.8 kg·m/s 1/2 MV ² = 0.0018 x 10 ⁵ kg m ² /s ² Diaphragm ruptured, fuze bent forward	Gun 34 V = 197 m/s MV = 1.0 kg·m/s 1/2 MV ² = 0.0010 x 10 ⁵ kg m ² /s ² Fuze bent forward slightly
	Gun 61 D V = 217 m/s MV = 15.8 kg·m/s 1/2 MV ² = 0.0172 x 10 ⁵ kg m ² /s ² Diaphragm ruptured		
	Gun 62 D V = 205 m/s MV = 15.0 kg·m/s 1/2 MV ² = 0.0153 x 10 ⁵ kg m ² /s ² Diaphragm ruptured		
	Gun 59 V = 168 m/s MV = 12.3 kg·m/s 1/2 MV ² = 0.0103 x 10 ⁵ kg m ² /s ²		
	Gun 60 V = 166 m/s MV = 12.1 kg·m/s 1/2 MV ² = 0.0101 x 10 ⁵ kg m ² /s ²		

Table C-4. Tests to define P/I curve for Chemical Submunition 2.

Load Orientation	Impulsive Loading Sheet Explosive	Quasi - Impulsive Loading Body-to-Body Impact	Quasi - Static Loading MTS Machine
			<p><u>Static Test 3</u> - Fuze end load Peak load = 35,000 lb Peak pressure over cannister = 28,520 psi = 197 MPa</p> <p>Cannister bulges but never ruptures</p>
	<p><u>Test 43</u> C, D I = 91 ktaps</p> <p>Upper weld fractured, diaphragm ruptured</p>	<p><u>Gun 52</u> D, F V = 230 m/s MV = 90.9 kg•m/s 1/2 MV² = 0.104 x 10⁵ kg m²/s²</p> <p>Fuze removed, diaphragm ruptured</p>	<p><u>Static Test 1</u> - Full length Peak load = 45,000 lb Peak pressure over loaded area = 19,000 psi = 131 MPa</p> <p>Diaphragm ruptured</p>
	<p><u>Test 44</u> F, D I = 63.7 ktaps</p> <p>Fuze removed, diaphragm ruptured</p>	<p><u>Gun 51</u> F V = 158 m/s MV = 62.4 kg•m/s 1/2 MV² = 0.049 x 10⁵ kg m²/s²</p> <p>Fuze removed, diaphragm intact</p>	<p><u>Static Test 2</u> - Unsupported length Peak load = 19,000 lb Peak pressure over loaded area = 13,500 psi = 93.3 MPa</p>
	<p><u>Test 42</u> I = 46.8 ktaps</p> <p>Cannister slightly damaged, diaphragm and fuze intact</p>	<p><u>Gun 55</u> F V = 155 m/s MV = 47.1 kg•m/s 1/2 MV² = 0.037 x 10⁵ kg m²/s²</p> <p>Fuze removed V_f = 76.6 m/s</p>	
		<p><u>Gun 58</u> F V = 133 m/s MV = 53.3 kg•m/s 1/2 MV² = 0.035 x 10⁵ kg m²/s²</p> <p>Fuze removed</p>	
		<p><u>Gun 50</u> V = 119 m/s MV = 47.1 kg•m/s 1/2 MV² = 0.028 x 10⁵ kg m²/s²</p>	
		<p><u>Gun 54</u> V = 111 m/s MV = 32.9 kg•m/s 1/2 MV² = 0.018 x 10⁵ kg m²/s²</p> <p>Slightly dented canisters V_f = 49.1 m/s</p>	

Note: All tests performed at half-scale.

*1 tap = 1 dyne • s/cm²

APPENDIX D

EXPLOSIVELY ACCELERATED PLATE TESTS

A technique was devised using an explosive driver to accelerate a plate to impact target submunitions. Figure D-1 shows the experimental setup. A large, dead, soft, aluminum plate (6061-T0) is supported on top of a steel table by means of rigid foam collar. The steel plate is lightly attached to the bottom of the aluminum plate and lined up with a circular hole on the table top that is large enough to pass the steel plate through, but small enough to stop the aluminum plate. Detonation of the explosive charge on top of the aluminum plate projects the steel plate at the submunition located under the table, while the dead soft aluminum plate forms a stretchable diaphragm that covers the hole, preventing the detonation products from trailing the steel plate and obscuring high-speed photographs. In some tests, a patented dilute explosive (developed at SRI) that has an adjustable detonation pressure was used. The use of the dilute explosive ensured that the high pressures produced by conventional explosives would not break up the steel plate. Table D-1 gives the tests parameters for this technique.

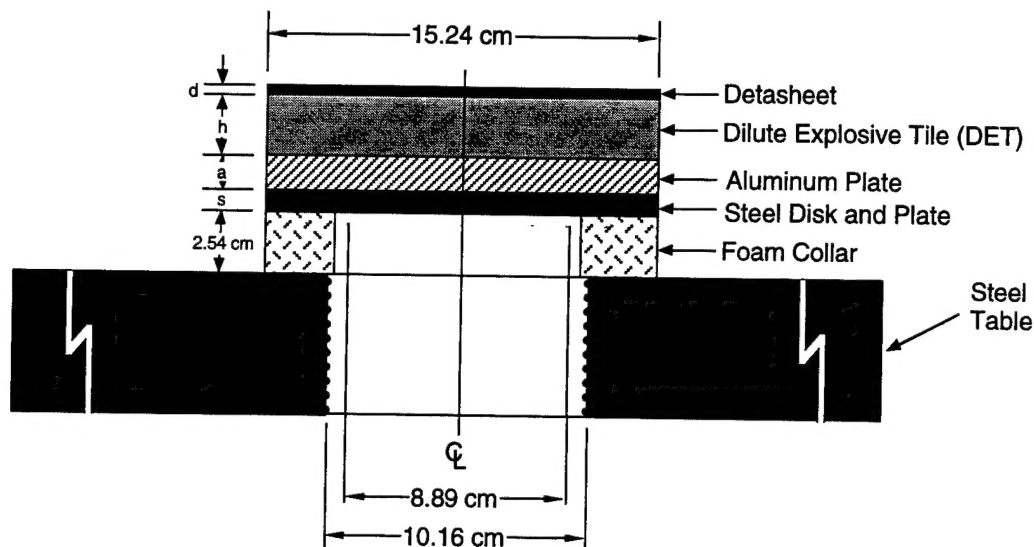


Figure D-1. Experimental setup for explosively accelerating steel plates.

Table D-1. Test parameters for explosively accelerated steel plates.

Test Number	Thickness (a) of Aluminum (cm)	Thickness (d) of Detasheet (cm)	Thickness (h) of DET (cm)	Thickness (s) of Steel Disk (cm)	Mass of Steel Disk (kg)	Velocity of Steel Disk (m/s)
TMD Cal-1	NONE	0.11	2.54	0.98	0.48'	N/A
TMD Cal-2	NONE	0.11	2.54	0.98	0.47	N/A
TMD Cal-3	0.64	0.11	2.54	0.98	0.48	N/A
TMD Cal-4	0.64	0.11	2.54	0.98	0.48	N/A
TMD Cal-5	1.27	0.11	2.54	0.98	0.48	N/A
TMD Cal-6	0.64	0.11	2.54	0.98	0.47	N/A
TMD Cal-7	0.64	0.11	2.54	0.98	0.48	185.6
TMD Cal-8	0.64	0.11	2.54	0.98	0.48	180.4
TMD Cal-9	0.64	0.11	2.54	0.98	0.48	179.2
TMD Cal-10	0.64	0.11	2.54	0.98	0.48	196.4
TMD Cal-11	1.31	0.11	5.08	0.98	0.48	244.7
TMD Cal-12	1.31	1.28	NONE	0.98	0.48	318.2

APPENDIX E

AIR GUN PERFORMANCE DATA

The relationship between gun pressure, sabot and impactor mass, and impactor velocity is depicted in Figure E-1, where sabot velocity is plotted versus the ratio of gun pressure to sabot mass for two different types of sabots. A mathematical fit to these data can be expressed by the relationship

$$V = C (P/M)^{1/2} \quad (E.1)$$

where V is sabot velocity in meters per second, M is sabot mass in kilograms, and P is the gun pressure in Pascals. Values of C that are used to fit the data vary between 0.28 and 0.34. For the combinations of mass and velocity on this program, the value of C was found to be about 0.30. Using this value for C, it was possible to predict impact velocity to within 3%.

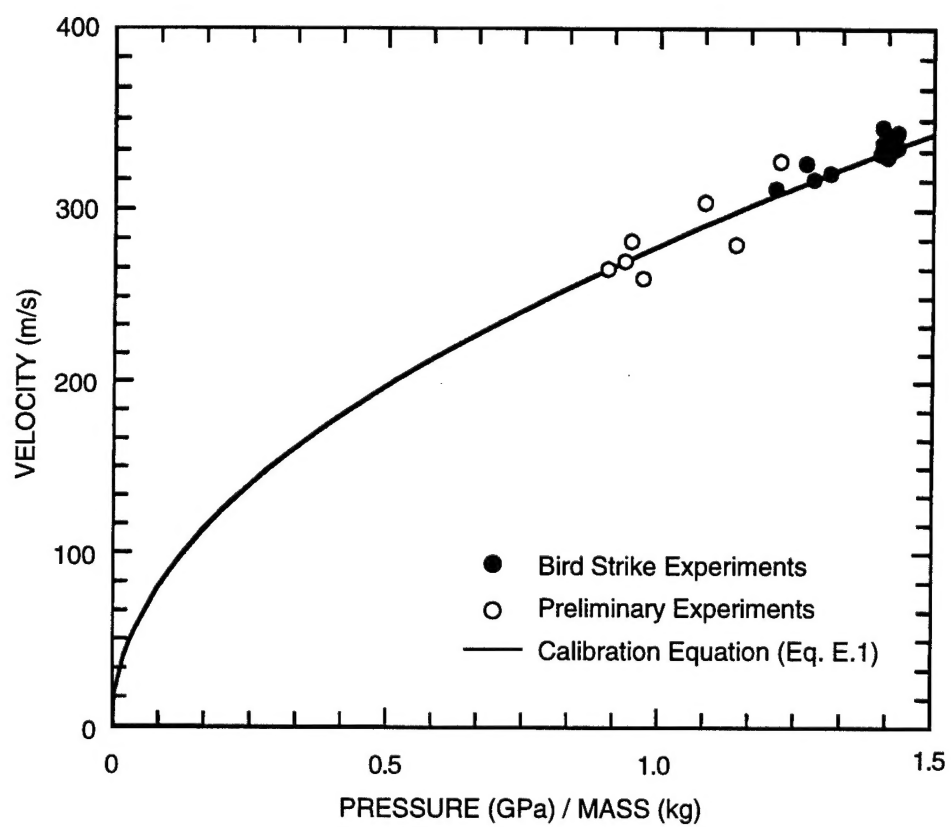


Figure E-1. Gas gun velocity calibration curve.

DISTRIBUTION LIST

DSWA-TR-96-19

DEPARTMENT OF DEFENSE

BALLISTIC MISSILE DEFENSE ORGANIZATION

ATTN: CDR HAGGERTY
ATTN: DAN WHITENER
ATTN: DOUG SCHAEFER

DEFENSE INTELLIGENCE AGENCY

ATTN: G WEBER

DEFENSE SPECIAL WEAPONS AGENCY

2 CY ATTN: ISST
3 CY ATTN: CDR KENNETH HUNTER

DEFENSE TECHNICAL INFORMATION CENTER

ATTN: DTIC/OCF

FIELD COMMAND DEFENSE SPECIAL WEAPONS AGENCY

ATTN: DR BALADI

DEPARTMENT OF THE ARMY

U S ARMY SPACE STRATEGIC DEFENSE CMD

ATTN: LIBRARY

USASSDC

3 CY ATTN: R BECKER

DEPARTMENT OF THE NAVY

NAVAL SURFACE WARFARE CENTER

ATTN: CHARLES R ELLINGTON

DEPARTMENT OF THE AIR FORCE

USAF

ATTN: RON HUNT

DEPARTMENT OF ENERGY

LAWRENCE LIVERMORE NATIONAL LAB

ATTN: G POMYKAL

LOS ALAMOS NATIONAL LABORATORY

ATTN: J V REPPA

SANDIA NATIONAL LABORATORIES

ATTN: ERIC REECE

DEPARTMENT OF DEFENSE CONTRACTORS

ARES CORP

ATTN: CHUCK MARTIN

BATTELLE MEMORIAL INSTITUTE

ATTN: C ALEXANDER

JAYCOR

ATTN: CYRUS P KNOWLES

KAMAN SCIENCES CORP

ATTN: VERN SMITH

KAMAN SCIENCES CORP

ATTN: DENNIS JONES

KAMAN SCIENCES CORPORATION

ATTN: DASIAC

LOGICON R AND D ASSOCIATES

ATTN: D GAKENHEIMER

LOGICON R AND D ASSOCIATES

ATTN: E TOTON

MAXWELL LABORATORIES INC

ATTN: DR G GURTMAN

SRI INTERNATIONAL

2 CY ATTN: A L FLORENCE

2 CY ATTN: C M ROMANDER

2 CY ATTN: J COLTON

2 CY ATTN: J H GIOVANOLA

2 CY ATTN: S W KIRKPATRICK

W J SCHAFER ASSOCIATES INC

ATTN: J CHERNAULT